Title

Turbulent mixing of settling dust in the Saharan Air Layer

Author

Branco Rodakoviski, Rodrigo

Publication Date

2024

Peer reviewed|Thesis/dissertation

UNIVERSITY OF CALIFORNIA

Los Angeles

Turbulent mixing of settling dust in the Saharan Air Layer

A dissertation submitted in partial satisfaction

of the requirements for the degree

Doctor of Philosophy in Atmospheric and Oceanic Sciences

by

Rodrigo Branco Rodakoviski

2024

ABSTRACT OF THE DISSERTATION

Turbulent mixing of settling dust in the Saharan Air Layer

by

Rodrigo Branco Rodakoviski
Doctor of Philosophy in Atmospheric and Oceanic Sciences
University of California, Los Angeles, 2024
Professor Marcelo Chamecki, Chair

Desert dust plays an important role in several components of the Earth system, mainly due to its nutrient content and interactions with radiation and clouds. Nevertheless, the airborne lifetime of coarse dust particles and their atmospheric transport from source regions are severely underestimated by current climate models. For instance, Saharan dust particles with diameters as large as 30 μm have repeatedly been detected in the Americas, while models are unable to reproduce this phenomenon. In this dissertation, we investigated the effects of vertical turbulent mixing in elevated shear layers on particle deposition rates. We focused on the Saharan Air Layer (SAL), a dust-laden air mass situated above the Marine Boundary Layer (MBL) that periodically moves from the African continent towards the Caribbean region over the tropical North Atlantic. Using an analytical approach combined with large-eddy simulations (LES), we first present a theory for dust concentration profiles evolving under the effects of gravitational settling and turbulent mixing. We found that the increase in dust airborne lifetime due to turbulence is determined uniquely by the Peclet number Pe (the ratio of the mixing timescale to the settling timescale), and it is limited to a factor of 2 when compared with laminar flows. Afterwards, we quantify the decrease in shear-induced eddy mixing rates caused by stable buoyancy stratification (which is typically present in the SAL). We found that, under weak stratification, SAL eddy diffusivities can be calculated as a function of layer depth, shear magnitude, and gradient Richardson number Ri_g. Our estimates indicate that

even small diffusivity values can significantly delay the deposition of particles as large as super coarse dust (with a diameter greater than $10\,\mu$m). In fact, we show that, together with particle asphericity, turbulent mixing can explain to a great extent the presence of super coarse Saharan dust in the Caribbean observed during the SALTRACE field campaign. Finally, we also note that the diffusivities calculated for our elevated SAL set-up decay faster with Ri_g than typical ABL models, highlighting the importance of employing appropriate parameterization schemes in climate models to represent slow processes (particularly affected by small diffusivities values) accurately.

The dissertation of Rodrigo Branco Rodakoviski is approved.

Jonathan M. Aurnou

Jasper F. Kok

James C. McWilliams

Marcelo Chamecki, Committee Chair

University of California, Los Angeles

2024

To my friends.

TABLE OF CONTENTS

LIST OF FIGURES

LIST OF TABLES

ACKNOWLEDGMENTS

Chapter 2 is reproduced from Rodakoviski et al. (2023) and Chapter 3 is reproduced from Rodakoviski et al. (In prep, preliminary version not yet submitted). Both publications are supported by the National Science Foundation under Grant 1856389, and the one that is already published is reproduced with permission from the publisher.

VITA

2024 Richard P. and Linda S. Turco exceptional research award, UCLA: for exceptional research publication.

2021 M.S. (Atmospheric and Oceanic Sciences), UCLA.

2019 M.S. (Environmental Engineering), Federal University of Paraná.

2017 B.S. (Environmental Engineering), Federal University of Paraná.

2014 Science Without Borders scholarship awarded by Brazilian Coordination for the Improvement of Higher Education Personnel (CAPES) to study abroad at the Department of Environmental Sciences and Engineering at the University Partis-Est Créteil, France.

PUBLICATIONS

Rodrigo Rodakoviski and Marcelo Chamecki. "Shear-induced vertical mixing in a stratified Saharan Air Layer". In prep.

Rodrigo Rodakoviski, Jasper Kok and Marcelo Chamecki. "Dust settling from turbulent layers in the free troposphere: Implications for the Saharan Air Layer.". In: Journal of Geophysical Research: Atmosphere 128.6 (2023), p. e2022JD037724. DOI: 10.1029/2022JD037724.

Rodrigo Rodakoviski and Nelson L. Dias. "Direct simulation of two-dimensional Bénard flow with free-slip boundary conditions.". In: Computers & Fluids 228 (2021), p. 105040. DOI: 10.1016/j.compfluid.2021.105040.

Alice M. Grimm et al. “Interdecadal variability and extreme precipitation events in South America during the monsoon season.” In: Climate Research 68.2–3 (2016), pp. 277–294. DOI: 10.3354/cr01375.

CHAPTER 1

Introduction

1.1 Introduction of the problem

1.1.1 Desert dust and the Saharan Air Layer

Dust is a key component of the Earth system. Mineral dust emitted from desert surfaces makes up about 70% of the total atmospheric aerosol loading (Tsigaridis et al., 2006). When suspended in the atmosphere, it can potentially affect human activity by causing visibility issues for aviation, as well as public health issues (Middleton, 2017). As it deposits back to Earth's surface, its nutrient content (e.g., iron) feeds ocean ecosystems, potentially promoting the development of algae blooms (Chien et al., 2016), as well as land ecosystems, such as the Amazon rainforest (Yu et al., 2015).

The effects of airborne mineral dust on atmospheric processes are numerous. Saharan dust events have been associated to a reduction of hurricane activity in the tropical North Atlantic (Dunion et al., 2004; Evan et al., 2011). Dust particles directly interact with radiation, mainly via short-wave (SW) scattering by fine dust (which acts to cool the climate) and absorption of both SW and long-wave (LW) radiation by coarse dust (which tends to warm the climate) (Otto et al., 2007; Adebiyi et al., 2020). Because dust particles can also serve as effective cloud and ice condensation nuclei (DeMott et al., 2003; Twohy et al., 2009), they also interact with radiation indirectly. As a result, their airborne lifetime importantly affects climate, weather, and atmospheric stability. Some of the greatest uncertainty in Earth's energy budget estimates comes from the contribution of dust (IPCC, 2021).

The greatest source of dust on Earth is the Sahara desert. It is estimated to emit about 1000 million tons of dust every year, contributing to about 50% of the global dust loading (Kok et al.,

2021). Turbulence in the Saharan Boundary Layer (SBL) promotes the emission of dust and its vertical distribution in the atmosphere, reaching heights up to about 6 km above the ground (Garcia-Carreras et al., 2015). Once dust is suspended and mixed in this deep boundary layer, prevailing wind patterns associated with the African Easterly Jet (AEJ) transport this warm, dust-laden Saharan air over the cooler, moister Marine Boundary Layer (MBL) in the tropical North Atlantic Ocean. This gives birth to the elevated Saharan Air Layer (SAL), an air mass extending from about 1 to 6 km above mean sea level (Carlson et al., 1972). Stable temperature inversions cap the SAL from above and below it.

SAL plumes move westward as they depart from the African continent, reaching the Caribbean region in the Americas about 5 days later. However, this process is not continuous in time. For one thing, SAL events follow a seasonal cycle, with peaks in frequency and intensity occuring in the summertime (Weinzierl et al., 2017). Furthermore, the AEJ dynamics causes the dust transport to be intermittent in shorter timescales. The zonal wind speed peaks over West Africa at a latitude of about $\varphi = 15^\circ$ N in response to strong meridional soil moisture gradients between the Sahara desert and tropical Africa, leading to the formation of the AEJ at about 600 hPa (Cook, 1999a). Barotropic and baroclinic instabilities of the jet produce African Easterly Waves (AEWs), which not only seed most tropical cyclones over the eastern Atlantic Ocean, but also contribute to the emission and transport of Saharan dust (Bercos-Hickey et al., 2017).

1.1.2 The coarse-dust long-range transport conundrum

Many processes impact the dust size distribution in the SAL during its 5-day transatlantic trip. The main process affecting coarse particles is gravitational settling and, despite its importance, it is currently overpredicted by climate models. This is because these models commonly assume that the free troposphere (away from Earth's surface) is not turbulent. As a result, they calculate settling speeds using Stokes' settling rates for a particle falling through a quiescent fluid medium. Many studies have shown that dust in the atmosphere deposits slower than these calculations (or large-scale models) predict. For instance, Kim et al. (2014) have shown that models predict a much faster decay in dust optical depth as SAL dust moves westward across the Atlantic than satellite

observations reveal. Adebiyi et al. (2020) demonstrated that dust in the coarse mode (with diameter $D_p \geq 5\,\mu$m) is being deposited too fast in global models, even though it represents more than 40% of the global dust loading. Field measurements have detected Saharan dust particles larger than $30\,\mu$m in the Caribbean, whereas calculations predict that no particle larger than $7\,\mu$m should be able to remain airborne for long enough so as to reach such a large distance from its source (Weinzierl et al., 2017).

Nevertheless, the processes responsible for keeping coarse dust suspended in the atmosphere for so long are still not fully understood. Amongst other hypotheses (discussed in chapter 2), small-scale turbulent mixing in the SAL interior is likely one of the mechanisms contributing (at least to some extent) to this phenomenon (Gasteiger et al., 2017; Van Der Does et al., 2018). In the atmosphere, turbulence is generally produced by mechanical shear (typically a change in horizontal wind speed with height) and buoyancy effects (e.g., in cloud-topped boundary layers being cooled from above). Both mechanisms are possible in the SAL. Moreover, the SAL is commonly described in the literature as a well-mixed layer (e.g., Ryder, 2021), which is supported by a number of observations (e.g., Rittmeister et al., 2017; Carlson, 2016; Jung et al., 2013). However, as discussed in chapter 3, we do note that observed potential temperature profiles reveal that most of the SAL is actually weakly stable most of the time. Thus, the idea of the SAL as a neutral, well-mixed layer is better regarded as an approximation.

1.2 Physical background

1.2.1 Elevated versus boundary layers in the atmosphere

The Atmospheric Boundary Layer (ABL) can be defined as the bottom layer of the troposphere, which is directly influenced by surface fluxes in the timescale of about an hour (Stull, 1988). Surface fluxes affecting the ABL flow dynamics are mainly the wall stress τ_w, typically represented in terms of a friction velocity $u_* \equiv \sqrt{\tau_w/\rho}$ (where ρ is the density of air), and a heat flux $\dot{Q}_{sfc}$.

Whereas the sign of the surface heat flux changes (e.g., following the diurnal solar cycle), τ_w always acts to enforce the no-slip boundary condition, i.e., the horizontal velocity $\mathbf{u}_h = 0$ at the

surface. Because ABLs are usually forced by a horizontal pressure gradient force (PGF) set by the synoptic scales, a mean flow develops away from the ground. As a result, there is typically strong wind shear in the lower levels of the ABL, and shear production of turbulence tends to dominate there. Above a certain height (roughly defined as the Obukhov length), however, buoyancy effects dominate. In a stable ABL, they act to suppress turbulence, whereas in a convective ABL, such as the daytime Saharan boundary layer, surface heating will enhance turbulence production. Strong updrafts develop, reaching levels up to the temperature inversion that caps the ABL, causing it to deepen by entrainment of free tropospheric air (Sullivan et al., 1998).

The SAL is similar to the ABL in several ways. It is possibly forced by both shear (associated with a large-scale PGF) and buoyancy effects, and it is also contained by temperature inversions. Generally speaking, both the ABL and an elevated layer like the SAL follow approximately an Ekman layer force balance, i.e., a balance between the Coriolis force, PGF, and Reynolds stresses (Kundu et al., 2015). However, the SAL is different in that internal heating resulting from radiative interactions involving dust and water vapor, as well as lateral entrainment of non-SAL air, are relevant. This is in contrast with the ABL, in which boundary fluxes usually dominate. Perhaps more importantly, however, is the fact that there is no solid wall in the SAL. Therefore, the flow does not have to transition from $\mathbf{u}_h = 0$ at the boundaries to its bulk velocity in the interior, so a surface shear layer with intense shear production is absent. This free-slip (or stress-free, $\tau_w = 0$) boundary condition has been shown to modify eddy fluxes and diffusivities from their no-slip counterparts. Rodakoviski et al. (2021) demonstrated this for Rayleigh-Benard convection, and the implications of this modified boundary condition for SAL flow are discussed in chapter 3.

1.2.2 Stratified turbulence

In high Reynolds number flows, a broad range of scales exists (Davidson, 2015). This is because large-scale structures become unstable and produce smaller-scale motions, which subsequently become unstable as well and generate even smaller flow structures, until small enough scales are reached such that viscosity can damp any perturbations. This is the idea of the energy cascade in turbulence, introduced by Lewis Richardson in the 1920s. As a result of this process, large-

scale directionality and inhomogeneities (e.g., set by the particular forcing mechanism and the domain geometry) are progressively lost as smaller eddies become more and more isotropic and homogeneous (in a statistical sense). In this so-called inertial subrange, turbulent eddies are self-similar, and the flow behavior is rather universal (i.e., independent from large-scale features). This is sometimes termed "Kolmogorov turbulence", referring to Andrey Kolmogorov's 1941 theory.

In the presence of buoyancy stratification, whether or not a Kolmogorov cascade exists for small enough scales was a puzzling question for quite some time. Many early experiments (e.g., Lin et al., 1979; Herring et al., 1989) reported the emergence of large-scale, rather flat structures denoted "pancake vortices", which evolved rather independently at different levels except for the viscous coupling arising in the presence of strong vertical gradients. This viscous coupling can dissipate enough kinetic energy to sustain a stationary state in the presence of constant forcing.

Nevertheless, time revealed that such early studies were conducted at Reynolds numbers that were too small. It is now known that, regardless of stratification, a Kolmogorov cascade will develop provided that the Reynolds number is large enough, with isotropic small scales being unaffected by buoyancy (Brethouwer et al., 2007; Bartello et al., 2013). In fact, buoyancy stratification affects primarily the large-scales of the flow, but it is no longer significantly felt at scales smaller than the so-called Ozmidov scale. This is a regime of strongly stratified turbulence, further discussed in chapter 3. In that chapter, we also present scale analyses to determine the nature of stratified turbulence in the SAL, which, from a fluid dynamics perspective, can be defined as a stratified free-shear layer constrained by thermal inversions.

1.2.3 Large-eddy simulations

Because high Reynolds number flows have such a broad range of scales, direct numerical simulations (DNS) of turbulence are extremelly computationally demanding. This is because they aim to resolve all scales of motion, from the domain scales down to the so-called Kolmogorov microscales. In fact, most of the computational effort in DNS is devoted to resolving high wavenumbers (Pope, 2000). Nevertheless, it is known from Kolmogorov's theory that the inertial subrange is a rather universal feature in many turbulent flows. Therefore, the effect of eddies in this range is mainly to cascade

flow properties down to the microscales, where energy is dissipated and local mixing takes place.

Consequently, it is possible to simulate turbulence numerically by explicitly resolving only the large eddies, as long as a subgrid-scale (SGS) model dissipates energy at the same rate ε as it cascade down to the numerical resolution scale (which must be placed in the inertial subrange). This technique is known as large-eddy simulation (LES). Large eddies depend on the flow geometry and forcing mechanism, and they contain most of the flow kinetic energy and contribute the most to momentum, heat, and dust fluxes. Because the microscales are not resolved in LES, the same amount of grid points $N_x N_y N_z$ can be used to simulate a larger domain than in a DNS of a flow with the same Reynolds number. As a result, LES can be an ideal tool to study relatively small-scale (e.g., $O(10)$ km) geophysical problems, such as ABL flows.

Because the SAL extends from Africa to the Americas, it is not possible (or appropriate) to perform an LES of this air mass as a whole. As described in chapter 2, we chose instead to simulate the flow within a small box in the SAL interior. This is a multiphase flow (containing air and dust), and various techniques to simulate flows of this kind exist. These include fully resolving the flow around individual particles, simulating Lagrangian point particles a posteriori (given a velocity field from a previous simulation), or representing dust concentrations as an Eulerian field. The choice of the appropriate method depends on both particle and carrier phase properties, as described in Balachandar et al. (2010). In the context of a SAL flow LES, this choice is discussed in chapter 2 and Appendix B.

1.3 Objectives

The overall hypothesis behind this dissertation is that, under some conditions and some periods of time, the SAL has strong enough forcing to produce and sustain at least some amount of turbulence. This impacts the transport of Saharan dust in that layer, and therefore may help explain observations of long-range transport of coarse particles.

In order to verify this hypothesis, we list the main objectives and research questions of this dissertation below:

Objective 1 Determine to what extent turbulent mixing can contribute to the long-range transport of coarse dust in the SAL.

(a) What is the relative increase in dust airborne lifetime caused by turbulence?

(b) Do models approach field observations when turbulent mixing is taken into account?

Objective 2 Develop a theoretical framework to quantify the effects of stable stratification on eddy mixing rates in the SAL.

(a) Can we develop an algebraic expression for the eddy diffusivity in the SAL as a function of some stability measure?

(b) When is stable stratification strong enough to suppress the effects of turbulence on dust deposition rates?

1.4 Outline

The remainder of this dissertation is organized as follows. Objective 1 is addressed in chapter 2, whereas objective 2 is addressed in chapter 3. Both of these chapters are exact reproductions of papers that have been published or submitted for publication (with permission from the publishers). As a result, each chapter contains its own introduction and conclusion, and utilizes its own nomenclature (which is consistent within a chapter, but not necessarily with other parts of this dissertation).

In chapter 2, we reproduce Rodakoviski et al. (2023), in which we assume the existence of turbulence in a neutral SAL. We use both an analytical approach (developed based on an idealized SAL model) and LES in order to assess the impact of turbulent mixing in settling rates of dust particles. Chapter 3 is a reproduction of Rodakoviski et al. (In prep), where we use a modified SAL model, in which a weak stratification is present. Again, we use a theoretical approach together with LES results in order to understand how to calculate eddy diffusivities based on quantities that are typically measured in the SAL. These results are then combined with results from chapter 2 to determine whether or not we expect SAL turbulence (under realistic forcing conditions) to be

vigorous enough to significantly delay dust deposition rates.

Finally, our conclusions are summarized in chapter 4, which also discusses future work to be developed. Appendices A through C correspond to the appendices published with Rodakoviski et al. (2023). Appendices D through H develop some ideas mentioned in chapter 3, and were published as supplemental information for Rodakoviski et al. (In prep).

CHAPTER 2

Dust settling from turbulent layers in the free troposphere: implications for the Saharan Air Layer

Authors: Rodrigo Rodakoviski, Jasper Kok and Marcelo Chamecki.

Abstract:

Desert dust accounts for a substantial fraction of the total atmospheric aerosol loading. It produces important impacts on the Earth system due to its nutrient content and interactions with radiation and clouds. However, current climate models greatly underestimate its airborne lifetime and transport. For instance, super coarse Saharan dust particles (with diameters greater than $10\,\mu$m) have repeatedly been detected in the Americas, but models fail to reproduce their transatlantic transport. In this study, we investigated the extent to which vertical turbulent mixing in the Saharan Air Layer (SAL) is capable of delaying particle deposition. We developed a theory based on the solution to a one-dimensional dust mass balance and validated our results using large-eddy simulation (LES) of a turbulent shear layer. We found that eddy motion can increase the lifetime of suspended particles by up to a factor of 2 when compared with laminar flows. Moreover, we found that the increase in lifetime can be reliably estimated solely as a function of the particle Peclet number (the ratio of the mixing timescale to the settling timescale). By considering both the effects of turbulent mixing and dust asphericity, we explained to a large extent the presence of super coarse Saharan dust in the Caribbean observed during the SALTRACE field campaign. The theory for the lifetime of coarse particles in turbulent flows developed in this study is also expected to be applicable in other similar geophysical problems, such as phytoplankton sinking in the ocean mixed layer.

2.1 Introduction

Desert dust accounts for about 70% of the global atmospheric aerosol mass (Tsigaridis et al., 2006). It carries key micronutrients to terrestrial and oceanic ecosystems (e.g., Yu et al., 2015; Chien et al., 2016) and potentially affects human activity by degrading visibility and human health (Middleton, 2017). Moreover, its interactions with radiation (Otto et al., 2007; Kok et al., 2017) and clouds (DeMott et al., 2003; Twohy et al., 2009) causes airborne dust to influence weather and climate significantly. In fact, the greatest uncertainty in Earth's energy budget estimates is still due to the contribution of aerosols and clouds (IPCC, 2021).

Despite its importance, and while it has been known that dust in the atmosphere deposits slower than predicted by Stokes' settling speed or simulated in large-scale models (e.g., Maring et al., 2003; Kim et al., 2014; Adebiyi et al., 2020), the processes responsible for keeping such particles suspended in the atmosphere for so long, especially those in the coarse and super coarse modes (i.e., those with volume-equivalent diameters greater than 5 and 10 μm, respectively), are still not fully understood. In fact, Adebiyi et al. (2020) estimated that the global load of coarse dust is actually four times greater than climate models currently simulate. This missing dust causes a net warming of the climate system due to absorption of solar and terrestrial radiation.

Perhaps the most well-known dust transport pathway in the atmosphere is the so-called Saharan Air Layer (SAL), a hot, dry, dust-laden air layer originating from North Africa and traveling across the tropical North Atlantic toward the Americas over the course of about 5 days (Carlson et al., 1972). The SAL is not directly in contact with Earth's surface; it rather is situated above the cooler, moister trade-wind layer, separated from it by a temperature inversion which is typically located at about 1.5-km altitude off the west coast of Africa, where the SAL extends to altitudes of 6 km or higher from the surface.

Amongst the various field experiments conducted in the past couple of decades aiming to study the behavior and properties of desert dust in the SAL (e.g., Reid et al., 2003; Tanré et al., 2003; McConnell et al., 2008; Heintzenberg, 2009; Siebert et al., 2013), the Saharan Aerosol Long-Range Transport and Aerosol-Cloud-Interaction Experiment (SALTRACE) was a particularly recent and comprehensive one (Weinzierl et al., 2017). One remarkable result from SALTRACE was obtained

when the same air mass in the SAL was sampled before and after transatlantic transport. This Lagrangian experiment revealed the presence of dust particles as large as $\sim 30\,\mu$m in the Caribbean, whereas the Stokes' settling rate for a laminar environment predicted that no particles larger than $\sim 7\,\mu$m should be able to make it there, even after a correction for particle asphericity (which reduces the deposition rate) was taken into account (Weinzierl et al., 2017).

A few reasons could explain the observed discrepancies and failure of Stokes' law. For one thing, dust particles have very irregular shapes (e.g., Muñoz et al., 2007), which reduces their settling speed due to the increased drag force experimented by dust when compared to a sphere of same volume (Mallios et al., 2020; Huang et al., 2020). Second, dust becomes electrically charged during its emission and possibly transport, and it has been hypothesized that the resulting electric forces could partly counteract gravitational settling (e.g., Nicoll et al., 2010; Van Der Does et al., 2018; Toth III et al., 2020), although results from a model simulating dust charging mechanisms by Mallios et al. (2022) indicated that the acceleration due to those forces is much smaller than gravity (and hence they should not affect settling speeds). Another reason, which is the focus of this paper, is the possibility of vertical turbulent mixing in the SAL, with the associated upward eddy flux increasing the airborne lifetime of dust particles (Gasteiger et al., 2017; Van Der Does et al., 2018). The innacurate or absent representation of at least some of these processes might explain why large-scale models consistently tend to underestimate the atmospheric coarse dust loading.

In the SAL, it is possible that turbulent motion is forced by both shear and buoyancy mechanisms. Substantial wind shear takes place over West Africa, especially due to the presence of the African Easterly Jet (AEJ) (e.g., Bercos-Hickey et al., 2017). Furthermore, differential absorption and scattering of both short- and long-wave radiation by different size particles could trigger convective motion (Otto et al., 2007; Gasteiger et al., 2017). In fact, recent analyses of lidar and dropsonde data by Gutleben et al. (2021) revealed small Richardson numbers within the SAL, as well as lidar power spectra following the predicted turbulence slope of $-5/3$, both of which are indicative of well established turbulence in that layer.

Furthermore, there exists substantial observational evidence that the SAL is a relatively well-mixed layer, which suggests the presence of turbulence. This includes, for example, lidar profiles of particle linear depolarization ratio (Rittmeister et al., 2017), potential temperature measurements

from soundings (Carlson, 2016), as well as aerosol concentration and water vapor mixing ratio profiles from in situ aircraft data (Jung et al., 2013; Ryder, 2021), all of which are rather uniform with height. The effect of daytime convective motion in the SAL was illustrated by Gasteiger et al. (2017) by means of a simple mathematical representation of turbulent mixing. Even though their results suggest that in situ SALTRACE data and satellite-borne lidar measurements are inconsistent with the absence of mixing in the SAL (even when particle asphericity is taken into account), measurement uncertainties were comparable to the differences between calculations that included or neglected mixing. Hence, further research is necessary. Note, however, that it is well-established that turbulence in the Saharan boundary layer (over land) is crucial for the emission and vertical distribution of dust before the elevated SAL is formed (Garcia-Carreras et al., 2015).

More generally, the problem of particles settling in a turbulent environment can be extended to other geophysical situations, with minor modifications necessary in some cases. An instance of an analogous problem to dust in the SAL is that of particles in the ocean mixed layer (OML), such as phytoplankton, sinking into the pycnocline (Ruiz, 1996; Deleersnijder et al., 2006). The long-lasting, global dust storms in Mars are another example of a similar problem which is particularly relevant at present due to the challenges that it poses to the robotic exploration of that planet. In this case, though, the bottom of the flow is a solid boundary, and physical parameters (such as gravity and density) can have very different values as compared to terrestrial flows (Rana et al., 2021). Hence, in this text, phrases like "dust in the SAL" will often be used in situations where ideas also apply more generally to particles settling in turbulent flows, and can potentially be extended to other geophysical problems.

In the present study, we employed a one-dimensional mass balance of dust in the SAL using uniform eddy diffusivity and idealized boundary conditions in order to develop a theory quantifying the effect of turbulent vertical mixing on the settling rate of particles. Because large-eddy simulation (LES) allows for a more realistic representation of the turbulent dynamics by employing fairly universal subgrid-scale models, we verify our theory using LES of a turbulent shear layer which is intended to be a proxy for the flow within the SAL.

This paper is organized as follows. Section 3.3 presents the idealized mass balance that leads to analytical expressions for airborne aerosol concentration, total mass and residence time as a function

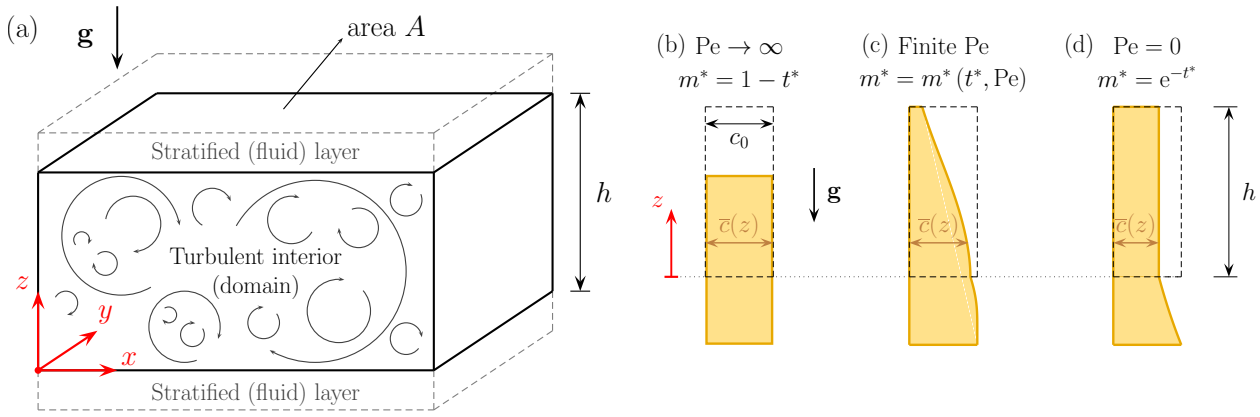

Figure 2.1: (a) Schematic representation of domain geometry. A turbulent, dust-laden fluid layer (region enclosed by black, solid lines, with its base at $z = 0$) of height h is contained in between two stably stratified, laminar fluid layers. (b–d) Illustration of theoretical dust profiles at $t^* = 0.4$ for different Peclet numbers (defined in equation (2.10)). The dashed lines delimit the turbulent layer and indicate the initial dust distribution (uniform from $z = 0$ to h), whereas the width of the yellow regions is proportional to the concentration at any level. The dotted line indicates the lower boundary of the SAL, and the flux of dust crossing it is proportional to the concentration at that level (see equation (2.5)), which in turn depends on the degree of turbulent mixing and the particle size via Pe.

of particle size and turbulent mixing efficiency. The numerical simulations performed are described in section 3.4, which also includes information about the simulated particle size bins. LES results are then analyzed and used to validate the theory in section 2.4, where we also demonstrate how our model helps explain the long-range transport of super coarse dust observed during SALTRACE. Finally, concluding remarks are made in section 3.6.

2.2 Theory

In this section, we develop an exact expression for the total particle mass m (in kg of dust) over time t within a turbulent layer of thickness h, given an initially vertically homogeneous concentration field. Two competing effects determine the mass decay rate: gravitational settling and vertical turbulent mixing.

2.2.1 Problem setup

The idealized flow setup depicted in figure 2.1a is intended to be a prototype for the SAL. It is assumed that turbulence is restricted to the inner layer, vanishing at $z \leq 0$ and $z \geq h$ due to stable thermal stratification. Note that, in this coordinate system, $z = 0$ is located above the ground (i.e., there is no solid boundary in this flow).

We assume that the flow is a dilute dispersion, so that interactions between particles and the back influence of dust on the flow dynamics are negligible. Denoting the particle velocity vector as $\mathbf{u}_p = (u_p, v_p, w_p)$ in Cartesian coordinates, in which the position vector is $\mathbf{x} = (x, y, z)$, with z being the vertical direction (i.e., that aligned with the acceleration due to gravity $\mathbf{g} = (0, 0, -g)$), conservation of mass for monodispersed particles requires that

$$\partial_t c + \mathbf{u}_p \cdot \nabla c = \kappa \nabla^2 c. \tag{2.1}$$

In (2.1), c is the Eulerian particle concentration field (expressed as mass per unit volume), and κ is the particle mass diffusivity resulting from Brownian motion.

We further assume that particle inertia effects can be neglected (which is verified a posteriori, as described in section 2.3.4 and Appendix B). Then, according to the dusty gas approach (Balachandar et al., 2010), the particle velocity vector can be written as

$$\mathbf{u}_p = \mathbf{u} - w_s \widehat{\mathbf{k}}, \tag{2.2}$$

where $\mathbf{u} = (u, v, w)$ is the instantaneous wind velocity vector, $w_s > 0$ is the constant particle settling velocity (relative to the air), and $\widehat{\mathbf{k}} = (0, 0, 1)$.

Rewriting (2.1) in terms of $\mathbf{u}$ using (2.2), and applying Reynolds averaging (Pope, 2000, eq. (4.41)), we can write the evolution equation for the mean particle concentration as (Shao, 2008, eq. (8.9))

$$\partial_t \overline{c} + \overline{\mathbf{u}} \cdot \nabla \overline{c} - w_s \partial_z \overline{c} = \kappa \nabla^2 \overline{c} - \nabla \cdot \overline{\mathbf{u}' c'}, \tag{2.3}$$

where the overbar denotes Reynolds averages and the prime indicates fluctuating quantities. The terms on the left-hand side of (2.3) refer respectively to the mean concentration time trend, advection by the mean flow and gravitational settling, whereas those on the right-hand side correspond

respectively to Brownian diffusion and eddy fluxes (i.e., advection by turbulence).

Brownian diffusion is expected to be negligible compared to gravitational settling for particles larger than $\sim 0.001\,\mu$m in the SAL (see calculations in the Supporting Information). Therefore, the corresponding term in (2.3) can be safely neglected. For the sake of simplicity, we also disregard subsidence effects by assuming $\overline{w} = 0$. Furthermore, by assuming statistical homogeneity in the horizontal directions (meaning that horizontal gradients of mean concentrations and turbulent fluxes vanish, i.e., $\partial_x \overline{c} = \partial_y \overline{c} = \partial_x \overline{u'c'} = \partial_y \overline{v'c'} = 0$), we obtain the following evolution equation for $\overline{c}$:

$$\partial_t \overline{c} - w_s \partial_z \overline{c} = -\partial_z \overline{w'c'}. \tag{2.4}$$

Equation (2.4) is frequently used (with the assumption of stationarity) to model the vertical profile of mean dust concentration in the atmospheric boundary layer (Prandtl, 1952; Kind, 1992; Freire et al., 2016).

We initialize the concentration field with a uniform profile $\overline{c}\,(z, t = 0) = c_0$ within the turbulent layer $0 < z < h$ and zero elsewhere. This is consistent with the observed well-mixed SAL over the eastern Atlantic (Carlson, 2016). Integrating (2.4) in the vertical direction from $z = 0$ to h, neglecting eddy fluxes across the top and bottom boundaries (such as entrainment/detrainment processes, an assumption expected to hold for larger particles and to be tested with the numerical simulations described in section 3.4), and considering that there is no dust above the turbulent layer entering the domain through its top, we find that the particle mass removal rate is given by

$$\frac{1}{A}\frac{\mathrm{d}m}{\mathrm{d}t} = -w_s \overline{c}\,(z = 0, t)\,, \tag{2.5}$$

where A is the horizontal area of the domain.

Physically, (2.5) means that the only particle removal mechanism is gravitational settling through the bottom of the turbulent layer. The removal rate depends on the mean concentration at $z = 0$, which is generally not known a priori, since it comes from the solution to (2.4). However, there are two limiting cases where $\overline{c}\,(z = 0, t)$ is known; these are presented in section 2.2.2. A closure model for the eddy fluxes in (2.4), which are responsible for vertical turbulent mixing thereby delaying particle removal, is necessary to generalize the asymptotic results to an arbitrary turbulence intensity.

This is discussed in section 2.2.3.

2.2.2 Asymptotic limits: laminar flow and instant mixing

In the first limiting case, we consider a laminar environment, where turbulent motion is absent. In this scenario, the whole particle field falls as if it were a single solid block, given that no process acts to erode the sharp gradient that develops at the top of the dust layer (figure 2.1b). In this case, the concentration at the bottom remains unchanged and equal to the initial condition at all times, i.e., $\overline{c}\,(z=0,t)=c_0$, and (2.5) can be integrated to give the linear decay

$$m^* = \begin{cases} 1-t^*, & t^* \leq 1, \\ 0, & t^* > 1 \end{cases} \qquad \text{(laminar flow)}. \tag{2.6}$$

In (2.6), the dimensionless variables are $m^* = m/m_0$ (with $m_0 = c_0 Ah$, i.e., the initial dust mass) and $t^* = t/\tau_g$ (with $\tau_g = h/w_s$, i.e., the time that it takes for a particle to travel a distance h at speed w_s). Note that τ_g is also the time necessary for all the dust mass to be removed in the absence of turbulence, so that $m^* = 0$ for $t^* > 1$.

On the other hand, if turbulent mixing is instantaneous, the concentration profile at any instant t is completely well-mixed (figure 2.1d). Hence, the concentration at any height (including at $z=0$) equals $m\,(t)\,/Ah$, in which case (2.5) produces the exponential decay

$$m^* = \mathrm{e}^{-t^*} \quad \text{(instant mixing)}. \tag{2.7}$$

In this case, τ_g is the e-folding time for mass decay. As expected, this means that m^* decays slower than in the laminar case since turbulent mixing is continuously diluting the dust mass throughout the entire layer, thereby reducing the concentration at the bottom and hence the mass loss rate as well.

2.2.3 Exact solution for arbitrary Peclet number

For intermediate mixing rates (i.e., not instantaneous), it is necessary to incorporate a measure of turbulence intensity into (2.4). Parametrizing the vertical eddy flux in terms of a constant eddy

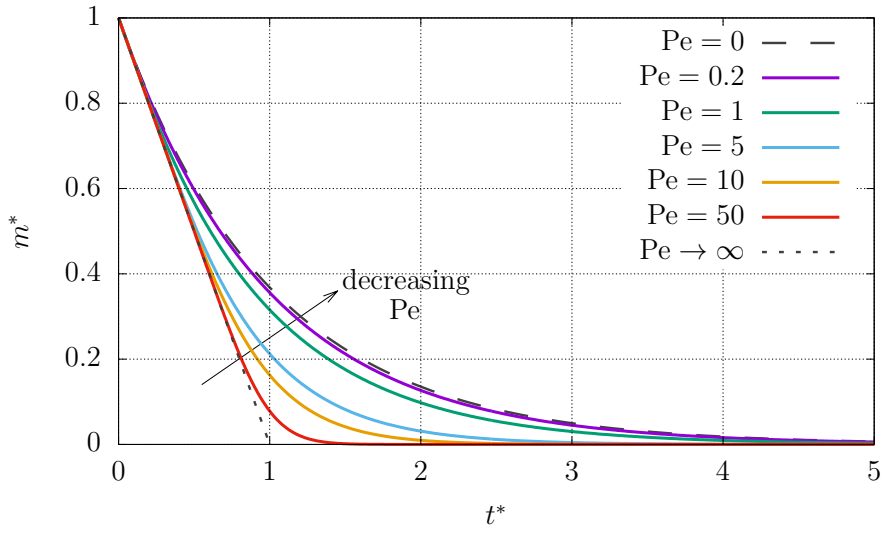

Figure 2.2: Theoretical solutions given by equation (2.12) for the remaining particle mass within the turbulent layer over time for different Peclet numbers (colors). The dotted and dashed lines show the asymptotic limits $m^* = 1 - t^*$ and $m^* = \exp(-t^*)$ for $\mathrm{Pe} \to \infty$ and $\mathrm{Pe} = 0$, respectively, as given by equations (2.6) and (2.7).

diffusivity K (such that $\overline{w'c'} = -K\partial_z\overline{c}$), (2.4) becomes

$$\partial_t\overline{c} - w_s\partial_z\overline{c} = K\partial_z^2\overline{c}. \tag{2.8}$$

Although this is often an unrealistically simple parametrization, a constant K allows for the development of an analytical solution to the problem (to be verified with the simulations described in section 3.4). In this model, the requirement that the entrainment fluxes vanish at the boundaries, along with a finite K-value, translates into homogeneous Neumann boundary conditions:

$$\partial_z\overline{c} = 0 \text{ at } z = 0 \text{ and } h. \tag{2.9}$$

This also prevents the solution to develop a maximum in the interior of the domain.

Brenner (1962) obtained a series solution for a problem equivalent to (2.8)–(3.7) with uniform initial condition, which can be used in the problem at hand. Defining the Peclet number as the ratio of a diffusive timescale τ_t (related to turbulent mixing) to a gravitational settling timescale τ_g, i.e.,

$$\mathrm{Pe} = \frac{w_s h}{K} = \frac{\tau_t}{\tau_g}, \quad \tau_g = \frac{h}{w_s}, \quad \tau_t = \frac{h^2}{K}, \tag{2.10}$$

we can write the solution $\overline{c}(z,t)$ as

$$\begin{aligned}\frac{\overline{c}(z^*,t^*,\mathrm{Pe})}{c_0} =& \frac{\mathrm{Pe}}{2}\exp\left\{\frac{\mathrm{Pe}}{4}\left[2\left(1-z^*\right)-t^*\right]\right\}\times \\ &\times\sum_{k=1}^{\infty}\frac{\lambda_k\left\{\lambda_k\cos\left[2\lambda_k\left(1-z^*\right)\right]+(\mathrm{Pe}/4)\sin\left[2\lambda_k\left(1-z^*\right)\right]\right\}}{\left(\lambda_k^2+\mathrm{Pe}^2/16+\mathrm{Pe}/4\right)\left(\lambda_k^2+\mathrm{Pe}^2/16\right)}\exp\left(-\frac{4\lambda_k^2 t^*}{\mathrm{Pe}}\right).\end{aligned} \tag{2.11}$$

Equation (2.11) can be integrated within the turbulent layer, i.e., from $z^* = z/h = 0$ to 1, to find the mass decay over time given by

$$m^*\left(t^*,\mathrm{Pe}\right) = \frac{\mathrm{Pe}}{4}\exp\left[\frac{\mathrm{Pe}}{4}\left(2-t^*\right)\right]\sum_{k=1}^{\infty}\frac{\lambda_k\sin\left(2\lambda_k\right)\exp\left(-4\lambda_k^2 t^*/\mathrm{Pe}\right)}{\left(\lambda_k^2+\mathrm{Pe}^2/16+\mathrm{Pe}/4\right)\left(\lambda_k^2+\mathrm{Pe}^2/16\right)}, \tag{2.12}$$

where the values of $\lambda_k > 0$ ($k = 1,2,\ldots$) are implicitly given by

$$\lambda_{2n-1}\tan\left(\lambda_{2n-1}\right) = \frac{\mathrm{Pe}}{4}, \quad \lambda_{2n}\cot\left(\lambda_{2n}\right) = -\frac{\mathrm{Pe}}{4} \tag{2.13}$$

for $n = 1,2,\ldots$. These values are ordered so that $\lambda_m > \lambda_n$ for $m > n$.

The Peclet number, defined in equation (2.10), measures the relative strength of particle gravitational settling with respect to vertical turbulent mixing which, in this model, are the two competing processes determining the airborne lifetime of dust. Hence, the larger (smaller) Pe is, the more (less) gravitational settling dominates over mixing. Note that, when time is normalized by τ_g, the mass decay curve (2.12), plotted in figure 2.2, depends solely on the Peclet number (which accounts for any particular combination of particle size and turbulence intensity). Figure 2.1c shows an example of an instantaneous concentration profile given by the solution (2.11) for a finite value of Pe.

As expected, the general solution (2.12) tends to the linear limit (2.6) as $\mathrm{Pe} \to \infty$, and it tends to the exponential limit (2.7) as $\mathrm{Pe} \to 0$. This fact is also illustrated in the plot of figure 2.2, and it can be nicely explained by interpreting Pe as a ratio of timescales. When $\tau_g \ll \tau_t$ ($\mathrm{Pe} \gg 1$), the entire particle field falls as a solid block because individual particles fall much faster than the mixing timescale, so that the concentration profile is simply advected without changing shape. When $\tau_t \ll \tau_g$ ($\mathrm{Pe} \ll 1$), on the other hand, turbulent mixing is so fast that it is capable to completly mix the particles within the domain before the particles fall a considerable distance.

As a final remark, it is noteworthy that the series (2.12) converges slowly at large Peclet number values. In that case, the alternative, approximate expression for m^* obtained by Brenner (1962) and

presented in Appendix A may become useful. Moreover, note that, since particles of different sizes are independent from each other in this model, an initial size distribution $m_0(D_p)$, where D_p is the volume-equivalent particle diameter, can easily be evolved in time as $m(t, D_p) = m_0(D_p)\, m^*(t^*, \mathrm{Pe})$. We highlight that both t^* and Pe depend upon D_p via their dependence on the settling velocity w_s (see equation (2.10)).

2.2.4 Residence time

The mean residence time of particles in the turbulent layer can be expressed as (Deleersnijder et al., 2006)

$$\tau_R = \frac{1}{m_0}\int_0^\infty m(t)\,\mathrm{d}t = \tau_g \int_0^\infty m^*(t^*, \mathrm{Pe})\,\mathrm{d}t^*, \tag{2.14}$$

from where it can be seen that the dimensionless residence time $\tau_R^* = \tau_R/\tau_g$ is a function of the Peclet number only. Integrating the asymptotic solutions (2.6) and (2.7), one finds that $\tau_R = \tau_g/2$ in the absence of turbulence ($\mathrm{Pe} \to \infty$), whereas $\tau_R = \tau_g$ when mixing is instantaneous ($\mathrm{Pe} = 0$), which means that turbulent mixing can increase the residence time of particles against gravitational settling by a factor of as much as 2 when compared to laminar flow (Deleersnijder et al., 2006).

In order to obtain $\tau_R(\mathrm{Pe})$ for intermediate Pe values, one can integrate (2.12), which results in

$$\tau_R^*(\mathrm{Pe}) = \frac{1}{16}\mathrm{Pe}^2 \exp\left(\frac{\mathrm{Pe}}{2}\right) \sum_{k=1}^{\infty} \frac{\lambda_k \sin(2\lambda_k)}{\left(\lambda_k^2 + \mathrm{Pe}^2/16 + \mathrm{Pe}/4\right)\left(\lambda_k^2 + \mathrm{Pe}^2/16\right)^2}. \tag{2.15}$$

However, similarly to (2.12), the series (2.15) converges slowly at large Pe values. Alternatively, a much simpler expression which, unlike the solution above, does not have convergence issues, has been given by Deleersnijder et al. (2006). Namely, they found

$$\tau_R^*(\mathrm{Pe}) = \frac{1}{2} + \frac{1}{\mathrm{Pe}} - \frac{1 - \mathrm{e}^{-\mathrm{Pe}}}{\mathrm{Pe}^2}. \tag{2.16}$$

As it should, equation (2.16) returns the same values as those given by the series (2.15). Deleersnijder et al. (2006) obtained that expression by means of an adjoint model approach which does not solve the complete problem (2.8)–(3.7) for $\overline{c}(z,t)$ or $m^*(t)$, but only for τ_R. In other words, their solution does not provide any information on the height dependence or the time evolution of the dust field, which are given in the present study by the series (2.11) and (2.12). Such knowledge is

necessary, for instance, in unsteady flows where the eddy diffusivity varies in time, which is likely the case of dust transport in the SAL (considering that it happens over 5 days). In this situation, the residence time can still be estimated via numerical integration of m^* with the Peclet number varying in time, but it will no longer be given by (2.16).

We highlight that, even at relatively large Peclet numbers, for which the particle behavior is mostly dominated by gravitational settling, the residence time is significantly enhanced by the presence of eddies in the flow. For instance, the relative increase in particle residence time due to turbulent mixing, calculated as $\left[\tau_R\left(\mathrm{Pe}\right) - \tau_R\left(\infty\right)\right]/\tau_R\left(\infty\right)$, is 18 % for $\mathrm{Pe} = 10$ and 57 % for $\mathrm{Pe} = 2$, i.e., τ_R increases respectively by almost a fifth and more than a half of its laminar value in these cases. This suggests that even moderately strong turbulence can considerably impact the settling rate of relatively large particles. As a final remark, notice that Pe is the relevant variable determining the extent to which turbulence impacts dust settling. Translating from Peclet numbers into actual particle sizes, on the other hand, depends on the turbulence intensity of the flow under consideration via K in equation (2.10). For approximate SAL conditions, such a relationship is illustrated in table 2.2.

2.3 Large-eddy simulation of idealized SAL

2.3.1 Averaging notation

Before the numerical simulations are described, it is important to define more accurately the notation to be used throughout the rest of the paper. In general, the mean of any variable η over a given direction, say x, is $\langle\eta\rangle_x$. Reynolds averages $\overline{\eta}$ are considered equivalent to $\langle\eta\rangle_{x,y,t}$, since all simulations are statistically homogeneous in the x- and y-directions. Averages in x and y are calculated over the entire domain, whereas averaging time periods varied case by case, following the criteria that they must be long enough for statistics to converge, but also short enough so that the turbulence (or the dust field, depending on the statistic being calculated) can still be approximated as stationary. Vertical averages are calculated within the turbulent layer only, i.e., $\langle\eta\rangle_z \equiv h^{-1}\int_0^h \eta\,\mathrm{d}z$, and $\langle\eta\rangle_{D_p}$ denotes an average over all simulated particle sizes. Finally, the vertical velocity variance

$\overline{w'^2}$ is also denoted as σ_w^2.

2.3.2 Numerical specifications of LES model and simulation parameters

Our incompressible LES code employs pseudospectral horizontal derivatives and second-order centered finite-difference derivatives in a staggered grid in the vertical direction. Time is advanced by means of a second-order Adams-Bashforth scheme. The subgrid-scale (SGS) model utilized was the scale-dependent Lagrangian dynamic Smagorinsky model by Bou-Zeid et al. (2005). The dust concentration fields were simulated with the finite-volume approach by Chamecki et al. (2008) and Chamecki et al. (2009), and SGS fluxes of dust were calculated using a constant turbulent Schmidt number $\mathrm{Sc} = 0.4$ (Chamecki et al., 2009, eqs. (2)–(4)).

Stress-free boundary conditions were applied to the horizontal velocity components at the top and the bottom of the numerical domain. The vertical velocity w was set to zero at those positions, and Rayleigh damping was implemented within the stratified layers (above and below the neutral SAL, which is defined by $z \in [0,h]$, as shown in figure 3) in order to minimize the reflection of gravity waves back into the domain. The thickness of each stratified layer was set to $h/2$, so that they were thick enough to dissipate the wave energy, but still did not needlessly increase the computational cost of the simulations. As a result, the domain vertical extent was $L_z = 2h$. In the horizontal directions, however, the domain is truncated, given the prohibitive computational cost of simulating a flow extending from Africa to the Americas at large-eddy scale resolution. Hence, in the horizontal we set $L_x = L_y = 4h$.

We used $N^3 = 320^3$ grid points and $h = 1\,\mathrm{km}$, so that $\Delta x/2 = \Delta y/2 = \Delta z = 6.25\,\mathrm{m}$. A timestep of $\Delta t = 0.25\,\mathrm{s}$ was chosen for stability and accuracy. Finally, the Coriolis parameter was set to $f = 5 \times 10^{-5}\,\mathrm{s}^{-1}$, which occurs at a latitude of about $\varphi = 20\,^{\circ}\mathrm{N}$, roughly coinciding with the location where the SAL is generally found in June and July, when the observed transatlantic dust transport typically peaks (Weinzierl et al., 2017).

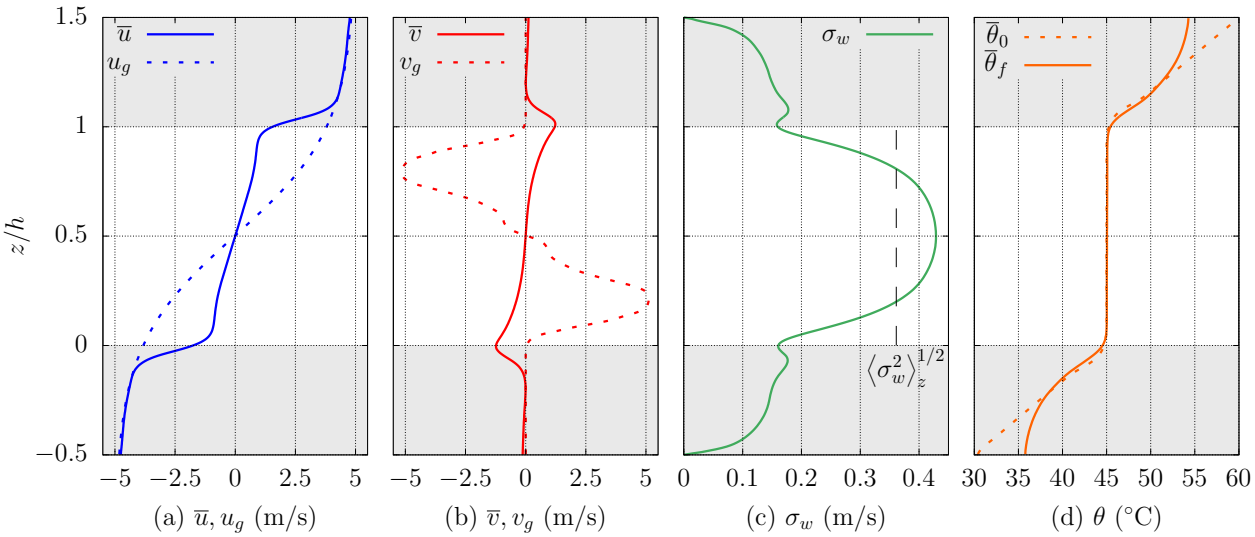

Figure 2.3: Mean LES conditions for BASE flow (WEAK case profiles are presented in the Supporting Information). The mean horizontal velocity $(\overline{u}, \overline{v})$ and the standard deviation of vertical velocity σ_w are calculated using the entire simulation duration (of about 55 h). The potential temperature profiles shown are $\sim$ 4-minute averages, with $\overline{\theta}_0$ and $\overline{\theta}_f$ denoting respectively the temperature structure at the beginning and the end of the simulation. The mean PGF profile driving the flow is prescribed in terms of the geostrophic wind speed (u_g, v_g). The stratified layers, indicated by the gray shaded regions below $z = 0$ and above $z = h$, are not included in the calculation of vertical averages such as $\langle \sigma_w^2 \rangle_z^{1/2}$.

2.3.3 LES flow setup

Temperature profile measurements reveal that the SAL is a nearly neutral layer bounded by inversions at the top and the bottom (e.g., Carlson et al., 1972; Otto et al., 2007). Such observations motivated the potential temperature structure adopted in our numerical simulations, which is depicted in figure 2.3d. The numerical domain includes not only the well-mixed SAL, but also part of the inversions above and below it. It does not include, however, the marine boundary layer (MBL) located below the bottom inversion.

Because the inversion layers are statically stable, growth of the turbulent, interior layer by entrainment is effectively suppressed. In fact, it can be seen in figure 2.3d that, even though the temperature structure changes significantly over time near the boundaries of the numerical domain due to the imposed adiabatic boundary conditions, stable stratification is preserved close to the inner interfaces between the inversions and the neutral interior. Therefore, the simulated SAL thickness

h indeed remained constant in the simulations, and the vertical boundary conditions implemented numerically are of negligible relevance to the turbulence dynamics in the interior. In the horizontal directions, we assume that there is no flux divergence in this truncated domain by adopting periodic boundary conditions in x and y.

The mean velocity profiles are plotted in figures 2.3a and 2.3b. Since the Coriolis effect is taken into account, we follow the usual geophysical convention that the x-direction points eastward and the y-direction points northward. Turbulence was induced in the neutral interior by shear in the mean flow, which in turn was forced by the vertically-varying pressure-gradient force (PGF) prescribed in terms of the geostrophic wind speed (u_g, v_g). Because there is vertical shear in the geostrophic wind, the temperature equation was adapted by means of the change of variables described in Momen et al. (2018) in order to account for the corresponding horizontal temperature gradient arising from thermal wind balance, so that the periodic boundary conditions, implicit to the pseudospectral differentiation scheme, were still valid. Thus, the mean force balance in the interior is similar to that of an Ekman layer, i.e., a balance between the PGF, Coriolis force, and Reynolds stresses (not shown). Geostrophic balance is reestablished in the stratified layers where the stratification is strong enough to suppress turbulence.

The mean velocity profile exhibits approximately uniform shear intensity within the neutral interior, causing the turbulence intensity (as given by σ_w in figure 2.3c) to increase towards the middle of the domain while still being somewhat uniform near the center. The increased shear magnitude at the interior edges of the stratified layers, which occurs as the mean wind transitions to the geostrophic profile, causes a secondary, but much smaller peak in σ_w at the same locations. Nevertheless, we did not observe any evidence that this affected the dynamics of dust transport in the interior in any way.

The adopted zonal geostrophic wind profile $u_g(z)$ follows the shape of a hyperbolic tangent, whereas its meridional counterpart $v_g(z)$ was set so as to reduce mean flow rotation and turbulence variability with height. The magnitude of the geostrophic wind, on the other hand, was adjusted so that the resulting mean shear S in the simulations (see table 2.1) was roughly comparable to the typical shear associated with the AEJ, estimated to be about $5 \times 10^{-3}\,\mathrm{s}^{-1}$ (Cook, 1999b; Weinzierl et al., 2017; Bercos-Hickey et al., 2020). We note that, if the LES shear is much weaker than the

Table 2.1: Flow characteristics in each simulation. Here, $\Delta u_g = u_g(z=h) - u_g(z=0)$, and the amplitude of $v_g(z)$ is proportional to that of $u_g(z)$ in each case. The shear intensity was calculated as $S^2 = (\mathrm{d}\overline{u}/\mathrm{d}z)^2 + (\mathrm{d}\overline{v}/\mathrm{d}z)^2$ and averaged within the interior, where $S(z)$ is uniform (this excludes the thin, strong-shear layers where the wind transitions to geostrophy). The eddy diffusivity estimation is addressed in section 2.4. The mixing timescale τ_t was calculated from its definition in (2.10) with $h = 1\,\mathrm{km}$ and $K = \langle K \rangle_{z,D_p}$, whereas the eddy turnover time was estimated as $\tau_e = h \left\langle \sigma_w^2 \right\rangle_z^{-1/2}$. Note that Δu_g is the only imposed quantity here, as the other variables were diagnosed from the LES output a posteriori.

Flow	Δu_g (m/s)	S (s^{-1})	$\left\langle \sigma_w^2 \right\rangle_z^{1/2}$ (m/s)	$\langle K \rangle_{z,D_p}$ (m^2/s)	τ_t (h)	τ_e (h)
BASE	7.62	2.91×10^{-3}	0.361	32.6	8.5	0.77
WEAK	4.57	2.27×10^{-3}	0.284	25.7	10.8	0.98

values given in table 2.1, production of turbulence kinetic energy (TKE) is not strong enough to balance its dissipation, and the resulting turbulence is either intermittent or decaying, instead of stationary as desired. Conversely, if the mean shear is much stronger, the turbulent layer grows by entrainment, and h is no longer a constant.

Finally, in an attempt to expand the parameter space analyzed, a similar flow (denoted "WEAK", as opposed to "BASE" previously described) with somewhat weaker turbulence (as its name suggests) was simulated. Results for WEAK are qualitatively similar to those for BASE but with less intense features, since the shape of the geostrophic wind speed profiles was kept the same, but their magnitude was reduced to 60 % of their BASE value (see table 2.1). The resulting mean flow shear S and vertical velocity standard deviation $\left\langle \sigma_w^2 \right\rangle_z^{1/2}$ for WEAK were measured to be about 78.1 % and 78.7 % of their BASE values, respectively, which suggests the linear scaling $\left\langle \sigma_w^2 \right\rangle_z^{1/2} \sim S$. Hence, all figures from 2.3 to 2.8 correspond to BASE, but results for WEAK are analogous (WEAK profiles corresponding to figure 2.3 are shown in the Supporting Information). This also served as a check to the similarity solution (2.10)–(2.13) in terms of the Peclet number, since Pe was also varied by changing the strength of turbulent mixing via K, and not only the particle size via w_s (see tables 2.1–2.2). The initial thermal structure is the same in both flows. Varying the turbulence intensity even further while keeping the same flow setup can be challenging, given that weaker turbulence dies out, and stronger turbulence causes the inner layer to grow. We also note that the fraction of total momentum (heat) flux represented by the SGS model in BASE is less than 1 % (10 %) in the SAL interior (except for 4 levels where the total heat flux changes

Table 2.2: Properties of the different size bins simulated in our LES. The gravitational timescale τ_g was calculated from its definition in (2.10) with $h = 1\,\mathrm{km}$, and the diameter values D_p were obtained via (2.17)–(2.18) by assuming aspherical silica dust particles with $\chi = 1.4$ and $\rho_p = 2650\,\mathrm{kg\,m^{-3}}$ in U.S. standard atmospheric air at about 2 km above the ground where $\rho_f = 1.0\,\mathrm{kg\,m^{-3}}$, $\mu_f = 1.7 \times 10^{-5}\,\mathrm{Pa\,s}$, and $g = 9.8\,\mathrm{m\,s^{-2}}$. The Peclet number was calculated as $w_s h \langle K \rangle^{-1}_{z,D_p}$ for each flow presented in table 2.1.

Bin #	1	2	3	4	5	6	7	8	9	10	11	12
w_s (cm/s)	0.2	0.4	0.8	1.6	2	2.4	3.2	4	8	12	16	20
τ_g (h)	139	69.4	34.7	17.4	13.9	11.6	8.7	6.9	3.5	2.3	1.7	1.4
D_p (μm)	5.8	8.2	11.6	16.5	18.4	20.2	23.4	26	37	46	54	61
Pe (BASE)	0.061	0.12	0.25	0.49	0.61	0.74	0.98	1.23	2.45	3.68	4.90	6.13
Pe (WEAK)	0.078	0.16	0.31	0.62	0.78	0.93	1.24	1.56	3.11	4.67	6.22	7.78

sign, namely at $z/h \approx 0.1, 0.33, 0.67, 0.9$). Close to the inversion layers at the top and bottom, these fractions approach $\sim 20\,\%$ for momentum and $\sim 30\,\%$ for heat.

Both flows were initially simulated for about 3 h without dust as a spin-up period (which is about 4 and 3 large eddy turnover times τ_e given in table 2.1, respectively), which was necessary to achieve equilibrium turbulence from the initial condition $\mathbf{u}_0 = (u_g, 0, 0) + \boldsymbol{\delta}\mathbf{u}_0$, where $\boldsymbol{\delta}\mathbf{u}_0$ is a small-amplitude, random noise. After that, the dust fields were initialized and simulated for a duration of $T_{LES} \approx 55\,\mathrm{h}$ for BASE and $T_{LES} \approx 56\,\mathrm{h}$ for WEAK, corresponding to at least 6 or 5 mixing timescales τ_t, respectively. The same particle sizes are simulated in both flows, as described in section 2.3.4.

2.3.4 Definition of dust size bins

In addition to the dynamical variables, concentration fields of 12 independent particle size bins (described in table 2.2) were also simulated. Each of them was initialized with a uniform profile in the neutral interior and zero elsewhere, i.e., the exact same initial condition employed in the one-dimensional mass balance discussed in section 3.3. The settling velocities w_s of the simulated bins were chosen to match relevant dust particle sizes and to span a wide range of Peclet numbers.

The various existing numerical simulation techniques for multiphase flows vary in complexity. They include methods that fully resolve the details of the flow around a single particle (Bagchi et al.,

2003; Burton et al., 2005), Lagrangian tracking of point particles using direct numerical simulation (DNS) data of the carrier fluid (Richter et al., 2018), and Eulerian approaches, which represent particles in terms of continuous concentration fields. Similarly to the theory described in section 3.3, our LES employs the dusty gas approach (Balachandar et al., 2010), which falls into the last category.

The dynamically relevant variable quantifying particle deposition rates, both in the theory and in the LES, is the settling velocity. The functional relationship between w_s and particle size, however, depends on the particle shape. Based on Stokes' law, one can write

$$w_s = \frac{\rho_p g D_{hd}^2}{18 \mu_f \phi\left(\mathrm{Re}_p\right)}, \quad \phi\left(\mathrm{Re}_p\right) = 1 + 0.15 \mathrm{Re}_p^{0.687}, \quad \mathrm{Re}_p = \frac{\rho_f w_s D_{hd}}{\mu_f}, \tag{2.17}$$

where ρ_p and ρ_f are respectively the particle and the fluid densities, and μ_f is the fluid dynamic viscosity (Clift et al., 2005, chap. 5). The non-linear correction due to finite particle Reynolds number Re_p is small but not negligible, and it decreases the estimated w_s by about 10 % for the largest particles (those in bin #12, for which $\mathrm{Re}_p = 0.6$).

In (2.17), we use the effective hydrodynamic diameter D_{hd}, defined as the diameter of a spherical particle with same settling speed as the irregular aerosol of interest (e.g., Westbrook, 2008). Hence, (2.17) can still be used to determine w_s for aspherical particles such as dust, and their volume-equivalent diameter D_p is related to the effective hydrodynamic diameter via

$$D_p = \chi^{1/2} D_{hd}. \tag{2.18}$$

In (2.18), χ is the dynamic shape factor, i.e., the ratio of the actual drag force acting on the irregular aerosol to that experimented by its equivalent-volume sphere (e.g., see Hinds (1999, eq. (3.23)) and Huang et al. (2020)). Similarly to Weinzierl et al. (2017), we use a value of $\chi = 1.4$ for Saharan dust.

Neglecting particle inertia effects is usually a very good approximation in the atmosphere away from the ground (Richter et al., 2018), since the Stokes number there is typically very small. After the particle sizes were defined and turbulence measurements from the simulations became available, the applicability of the dusty gas approach adopted in this study (both in the theory and numerical

simulations) was confirmed. The Stokes number for our heaviest particles was estimated to be at most St ≈ 0.07 in BASE, which has the fastest microscales. Such value is significantly smaller than the upper limit of St $= 0.2$ suggested by Balachandar et al. (2010) beyond which the dusty gas approach is no longer valid. See Appendix B for more details on the estimation of the relevance of inertial effects in our simulations. Moreover, note that we neglect the slip correction factor in (2.17) since it is estimated to increase the terminal velocity of the smallest particles simulated in the LES by less than $4\,\%$.

2.4 Results and discussion

2.4.1 Instantaneous flow fields

Figures 2.4 and 2.5 illustrate the turbulent behavior of the flow with instantaneous snapshots of the dust concentration and fluid vertical velocity fields at $t^* = 1$ for different size particles. The strong fluctuations in vertical velocity within the SAL are caused by the turbulent eddies, while those outside the neutral interior are weaker (due to buoyant destruction of TKE) and associated with gravity waves excited by the eddies within the SAL impinging onto the stratified layers. The signature of large eddies in the dust field is clearly visible for bin #12 (for which w_s has comparable magnitude to $\langle \sigma_w \rangle_z$) and still somewhat apparent for bin #9, with regions of positive vertical velocity generally coinciding with regions of high dust concentration. This pattern is not clearly observed for bin #4 though, since its Peclet number is much smaller, and hence its concentration remains much more uniform throughout the domain. Note that one also expects the dust field to become uncorrelated with the carrrier fluid phase for Pe values much larger than unity (as illustrated in figure 2.1b). Moreover, one can also notice in figure 2.4 that the largest eddies tend to span the entire turbulent layer (i.e., they scale with h), but eddies of many different length scales are present, as is characteristic of turbulent flows in general.

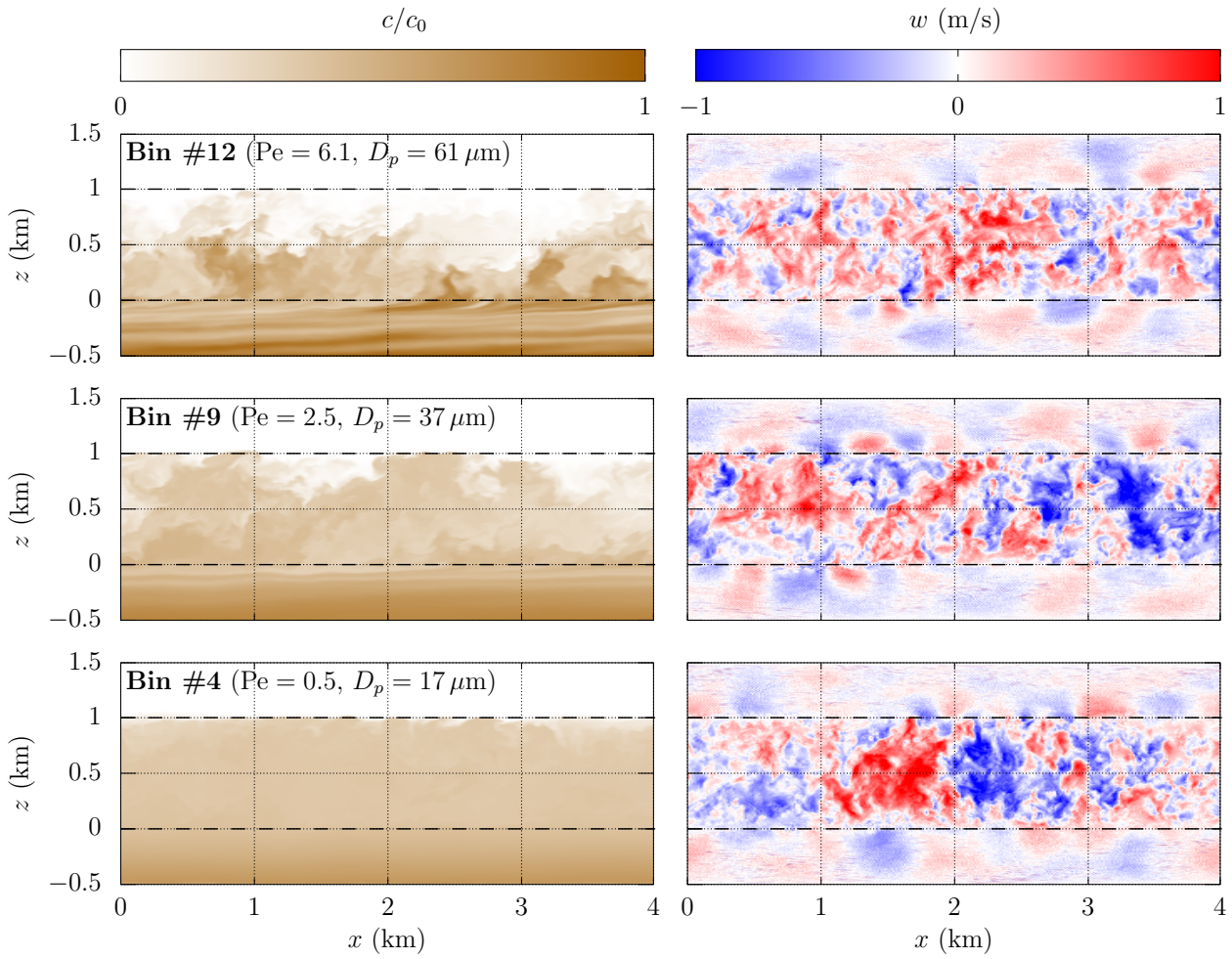

Figure 2.4: Side view of instantaneous dust concentration (left column) and corresponding fluid vertical velocity fields (right column) in BASE at $y = 0.5L_y$ and $t = \tau_g\,(w_s)$, i.e., the instant by which all particles in a given bin would have been removed from the interior ($0 \leq z \leq 1\,$km) if the flow was laminar there. We remark that, in general, the correspondence between Pe and D_p depends upon the turbulent mixing efficiency via K.

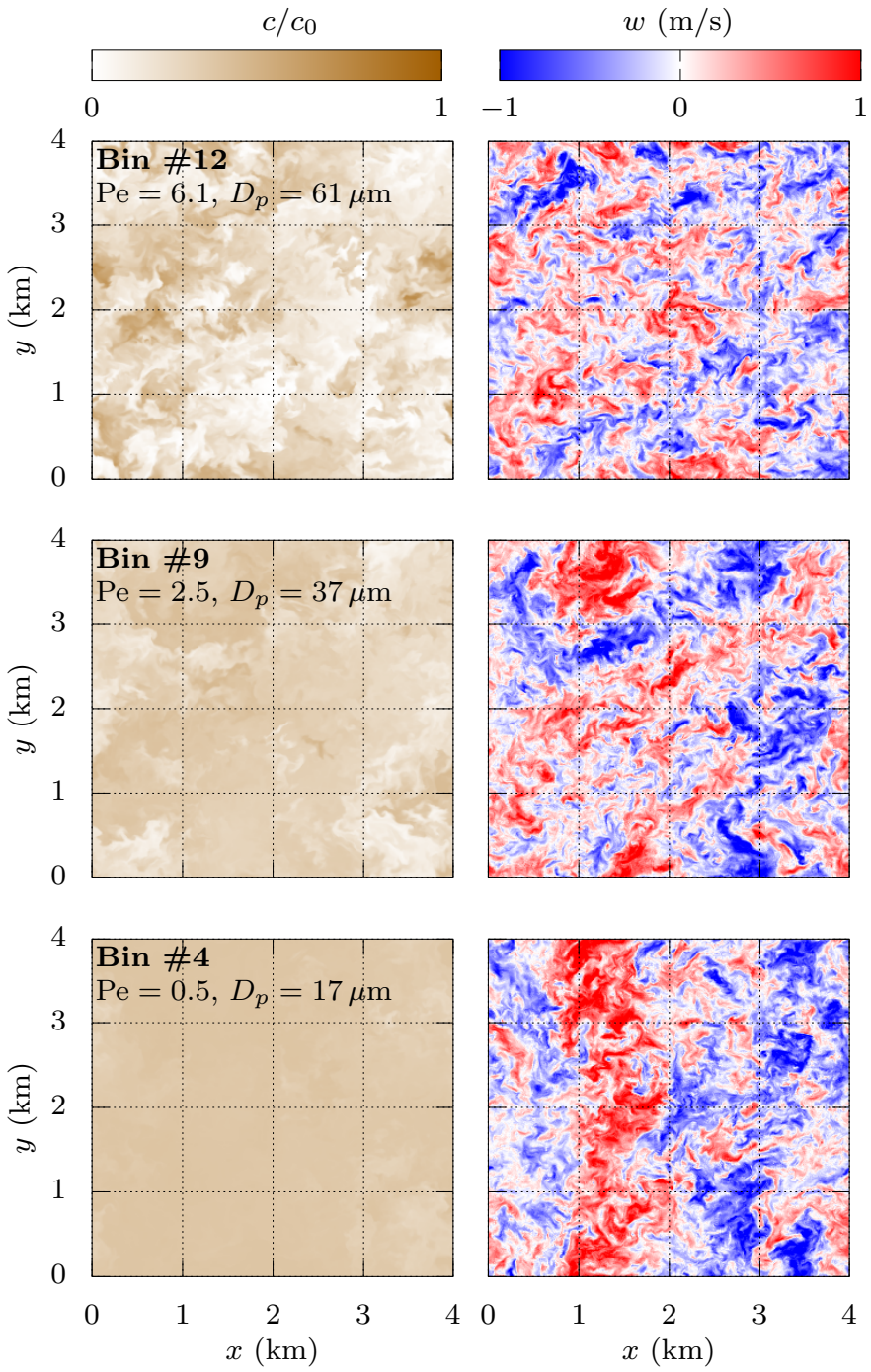

Figure 2.5: Top view of instantaneous dust concentration (left column) and corresponding fluid vertical velocity fields (right column) in BASE at $z = 0.5h$ and $t = \tau_g\,(w_s)$ (i.e., same instants shown in figure 2.4).

2.4.2 Comparison between LES and theory

In order to compare the numerical simulations output data with the theory (i.e., the analytical solutions given by equations (2.10)–(2.13)), one needs to assign a constant eddy diffusivity K to each particle size bin, since this is not defined a priori in the LES, where eddy fluxes are, for the most part, explicitly resolved (with a smaller fraction represented by the SGS model). Thus, two different approaches were utilized to estimate K in this study, as described below.

First, using the time series of aerosol mass within the turbulent layer ($0 < z^* < 1$) obtained by numerical integration of the LES results separately for each size bin, here denoted as $m^*_{LES}(t)$, we looked for the optimal diffusivity $K_\star$ minimizing the mean square error $\mathscr{E}$ with respect to the theoretical solution m^* given by (2.12), i.e.,

$$K_\star = \arg\min_K \left[\mathscr{E}(K)\right], \quad \mathscr{E}(K) = \frac{1}{T_{LES}} \int_0^{T_{LES}} \left[m^*_{LES}(t) - m^*(t,K)\right]^2 \mathrm{d}t. \tag{2.19}$$

In this sense, $K_\star$ can be regarded as the diffusivity value providing the best fit of the model (2.12) to the LES data, i.e., it determines how close the model can get to the data. Note that $K_\star$ so defined is not only a function of the turbulence, but also of the particle size. The theoretical mass decay curves obtained using $\mathrm{Pe} = w_s h K_\star^{-1}$ in (2.12) are plotted in figure 2.6 as gray, solid lines.

Secondly, we diagnosed profiles of eddy diffusivity $K(z,t)$ from LES data using its definition, i.e., $K = -\overline{w'c'}/\partial_z \overline{c}$. Some examples are shown in figures 2.7 and 2.8. Here, $\overline{w'c'}(z)$ and $\overline{c}(z)$ are planar, time averages calculated over a period of duration T_{avg} starting at different instants. The averaging period must be long enough for the statistics to converge, but also relatively small because the dust profiles are very transient, especially for large particles. Hence, we adopted the criterion $T_{avg} \lesssim 0.1\tau_g$, which entails better statistical convergence for smaller particles, for which τ_g is greater. Despite the substantial time variability of fluxes and gradients, however, a fairly robust diffusivity profile was recovered at all times, so that it was natural to take a final time average of those profiles to obtain a single curve $K(z)$ for each bin, some of which are represented by the black squares in figures 2.7 and 2.8.

Since K is assumed to be a constant in our theory, the vertical average of those profiles was also calculated, finally leading to the second eddy diffusivity estimate, denoted simply as $\langle K \rangle_z$.

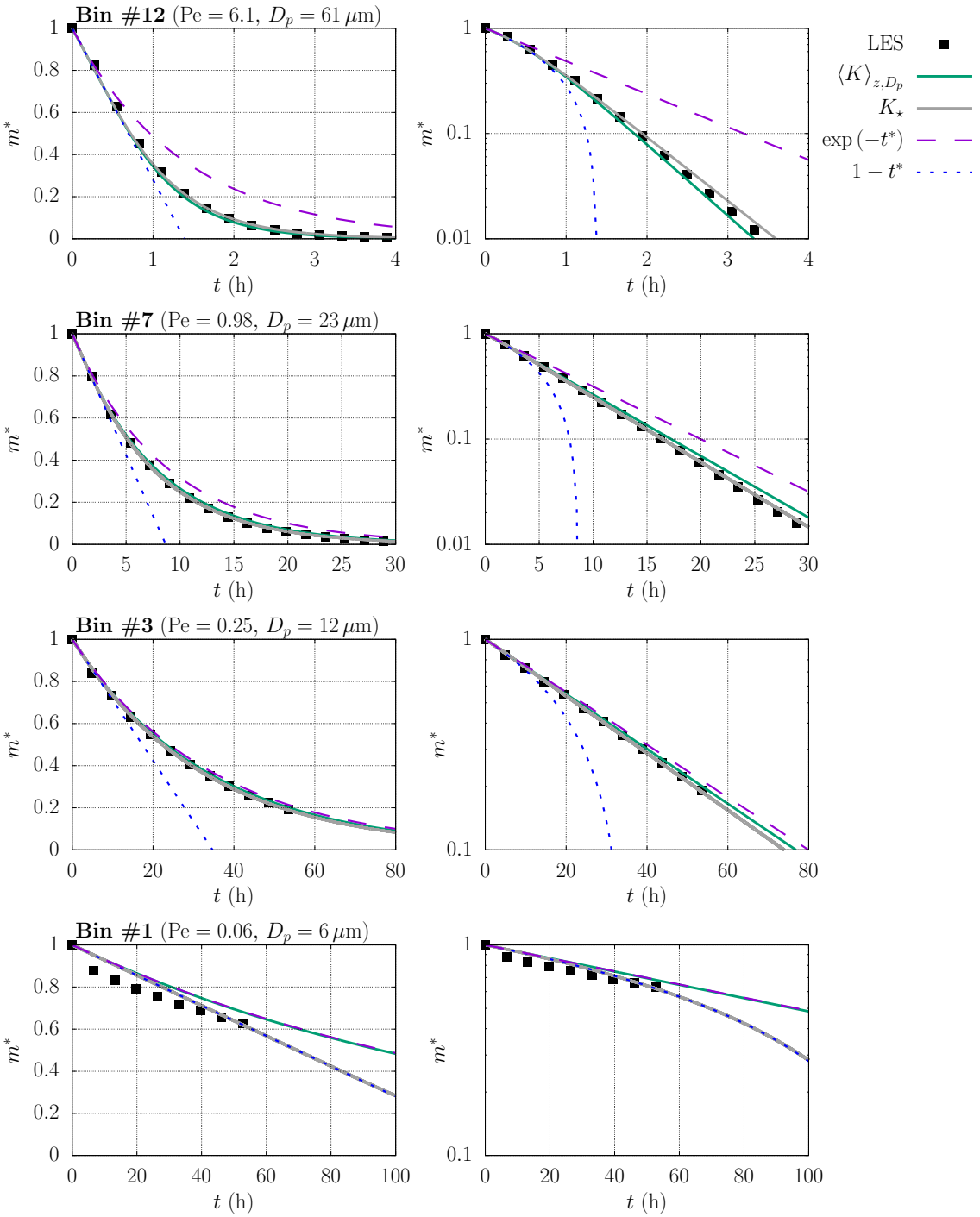

Figure 2.6: Remaining suspended particle mass fraction over time in BASE plotted in linear (left column) and log scales (right column) for different bins. Squares indicate LES values, whereas the solid curves show the theoretical prediction (2.12) calculated with $K = \langle K \rangle_{z,D_p}$ (average diffusivity diagnosed from LES) and $K = K_\star$ (optimal diffusivity defined in (2.19)). The linear and exponential asymptotic limits (2.6) and (2.7) are also plotted for comparison. We remark that, in general, the correspondence between Pe and D_p depends upon the turbulent mixing efficiency via K. Plots of $m^*(t)$ for all simulated bins are available in the Supporting Information.

Furthermore, although the overall shape of $K(z)$ changes significantly with particle size, with somewhat uniform profiles in the bulk at large Pe values becoming more variable with height as the particle size decreases, their mean magnitude $\langle K \rangle_z$, given by the black lines and symbols in figures 2.7 through 2.9, remains relatively robust for all simulated particle sizes. As a result, the diffusivity averaged over all bins $\langle K \rangle_{z,D_p}$ can be taken as representative of the turbulent flow itself. Theoretical mass decay curves obtained using $\mathrm{Pe} = w_s h \langle K \rangle_{z,D_p}^{-1}$ in (2.12) are plotted in figure 2.6 as green, solid lines.

It can be seen in figure 2.6 that, with the exception of the small particles (bin #1 and also bin #2, not shown here — see figures for all simulated bins in the Supporting Information), there is excellent agreement between the LES data and our theory (despite K being assumed constant in the latter). The curves were also plotted in a log scale (on the right column) because the best fit diffusivities $K_\star(D_p)$ provide very similar results to those obtained using $\langle K \rangle_{z,D_p}$, which is a constant, suggesting that the diffusivity dependence on particle size is negligible for this range of Peclet numbers. In fact, $\langle K \rangle_{z,D_p}$ is expected to be a more physical, reliable measure of the diffusivity as opposed to $K_\star$, which depends on the ability of the numerical simulations to reproduce the theoretical solution conditions. This is why Peclet numbers in this paper were calculated using $\langle K \rangle_{z,D_p}$ (unless otherwise stated). Moreover, it can also be seen that the curves progressively approach the exponential limit as the particle size decreases. Therefore, in summary, the LES results validate the analytical model presented in section 3.3.

The concentration and flux profiles presented in the two leftmost columns of figures 2.7 and 2.8 are dynamically coupled via (2.4), which can be re-expressed directly in terms of the variables being plotted as

$$\frac{\partial}{\partial t^*}\left(\frac{\overline{c}}{c_0}\right) = -\frac{\partial}{\partial z^*}\left(\frac{\overline{w'c'}}{w_s c_0} - \frac{\overline{c}}{c_0}\right). \tag{2.20}$$

It is apparent that, except for very small particles, the analytical solution (2.11) for $\overline{c}(z^*, t^*)$ matches the LES data quite well, even though the homogeneous Neumann boundary condition at the top assumed by the model does not seem very applicable to the LES conditions. Concentration estimates obtained from (2.11) do not match the corresponding LES values near $z = h$, which instead tend to vanish with a non-zero gradient. The simulated eddy fluxes, however, do generally vanish at the

boundaries in conformity with the theory.

For small particles, however, a finite eddy flux $\overline{w'c'}$ developed at $z = h$ in the simulations, as is visible in figure 2.8 for bins #1 and #2. Those particles "leak" through the shear layer top because they settle very slowly, and the numerical model is not able to maintain a sharp concentration gradient for such a long time. As a result of this additional sink, m^*_{LES} decays faster than our theory allows (see results for bin #1 in figure 2.6, and the corresponding concentration profiles in figure 2.8). Since this process is not represented by the theory, the analytical solution error $\mathscr{E}$ is thus minimized by a small $K_\star$ value, which instead increases the mass loss rate by reducing the mixing. This is why m^* calculated with $K_\star$ for bin #1 (see figure 2.6) coincides with the laminar solution, for which $K = 0$. Furthermore, for small particles, not only is $K(z)$ more variable with height, but also the concentration profiles become rather well-mixed, in which case the eddy-diffusivity model is unlikely to perform well, since gradients tend to vanish and non-local fluxes due to large eddies become particularly important. All those factors are expected to cause the theory and LES data to mismatch for those bins, leading to unphysical $K_\star$ values which are no longer representative of the diffusivity profiles diagnosed from the LES data. Finally, note that, for even smaller particles, it is possible that removal by detrainment from the turbulent layer becomes the dominant mechanism over gravitational settling, which would invalidate the analytical solution for very small Peclet numbers.

2.4.3 K-dependence on mean shear and particle size

The eddy diffusivity estimates for both simulations were plotted in figure 2.9 for different particle sizes as a function of the settling speed normalized by the turbulence intensity as measured by $\left\langle \sigma_w^2 \right\rangle_z^{1/2}$. The average eddy diffusivity $\langle K \rangle_{z,D_p}$ given in table 2.1 was verified to scale with $\left\langle \sigma_w^2 \right\rangle_z^{1/2}$, which itself scales linearly with the mean flow shear. Therefore, K was normalized by $h^2 S$ in figure 2.9, which to a great extent caused the data to collapse. This is particular relevant because the intensity of turbulent flucutations is not a known quantity a priori (based solely on simulation parameters), nor is it readily measurable in the atmosphere with standard meteorological instrumentation. Thus, being able to relate the eddy diffusivity to the mean shear magnitude S has significant practical

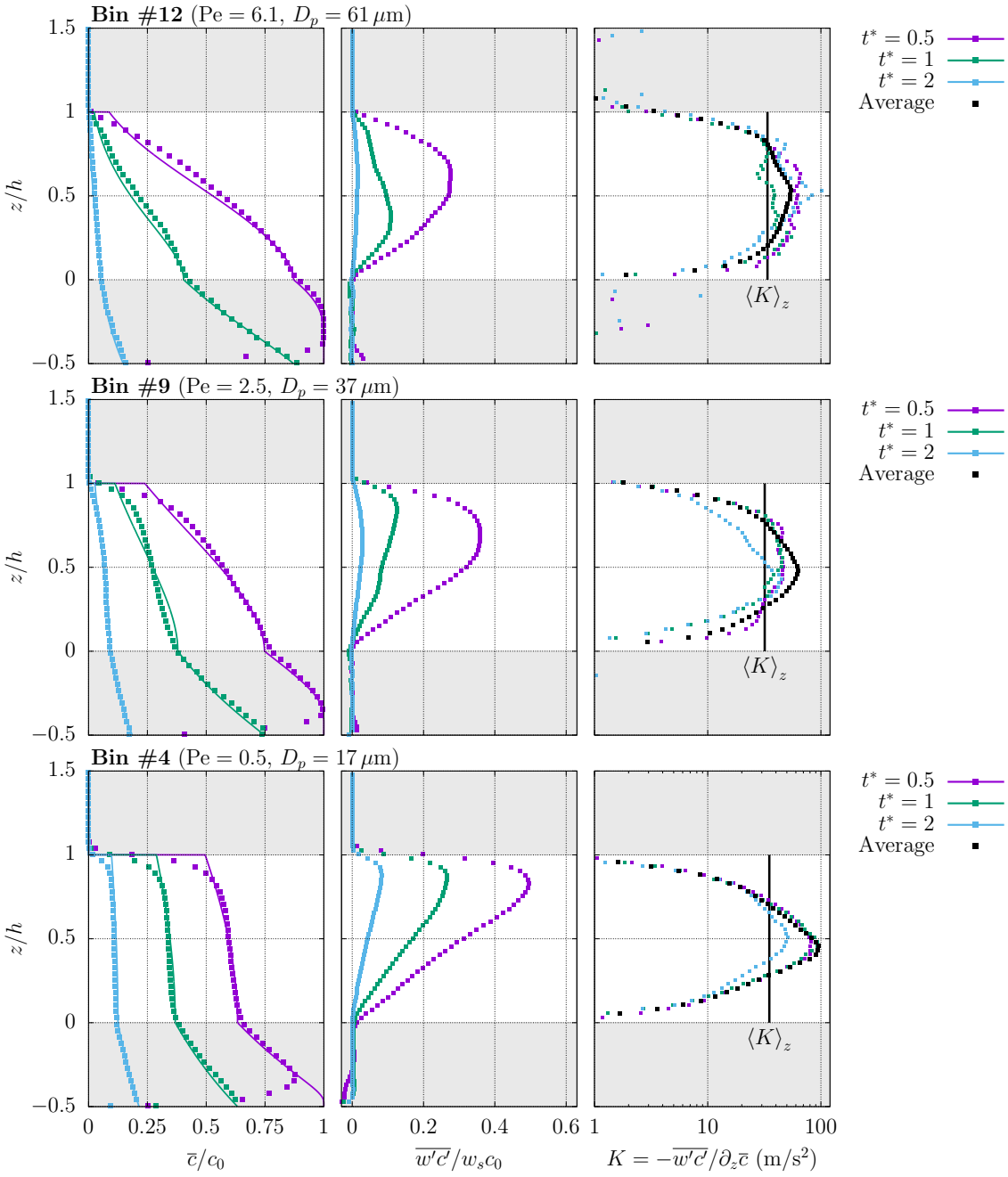

Figure 2.7: Vertical profiles of concentration (left), eddy flux (middle) and eddy diffusivity (right) for different size particles in BASE. Squares indicate LES data, whereas the solid lines on the left panels are the theoretical concentration profiles given by (2.11) calculated with $K = \langle K \rangle_{z,D_p}$ for $z \in [0,h]$, and advected below the turbulent layer as $\overline{c}\,(z^* < 0, t^*) = \overline{c}\,(0, t^* + z^*)$. Although the LES concentrations plotted here are $\sim$ 4-minute averages, the flux and diffusivity profiles are obtained from averages calculated over increasing time intervals T_{avg} for decreasing particle size (but still ensuring that $T_{avg} \lesssim 0.1\tau_g$ for stationarity). The instants t^* shown in the figure correspond to the end of the averaging periods. Vertically-averaged diffusivities $\langle K \rangle_z$ are also shown for each bin. We remark that, in general, the correspondence between Pe and D_p depends upon the turbulent mixing efficiency via K.

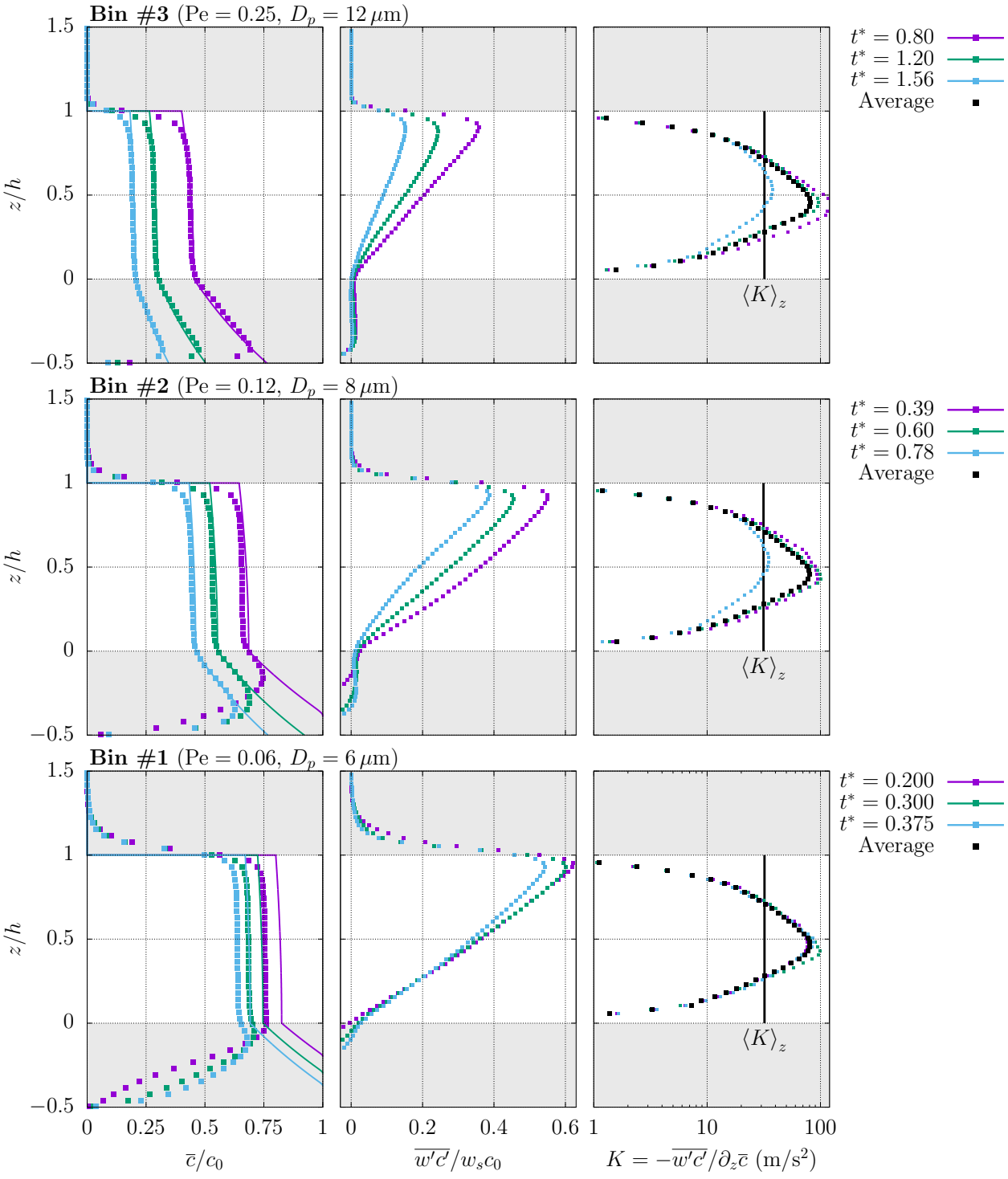

Figure 2.8: Same as figure 2.7 but for smaller particles. No-flux condition at $z = h$ is not respected in LES at small Peclet numbers.

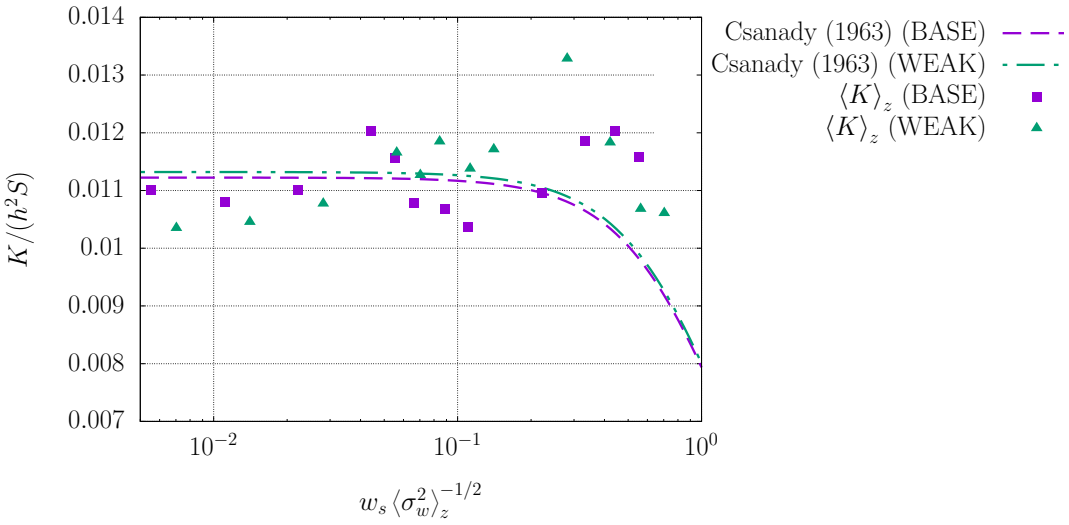

Figure 2.9: Normalized eddy diffusivity as a function of particle size (as given by its normalized settling velocity). The different estimates of K shown are Csanady's model (2.21) with $K_0 = \langle K\rangle_{z,D_p}$, and the vertically-averaged eddy diffusivity $\langle K\rangle_z$ calculated as $-\left\langle \overline{w'c'}/\partial_z\overline{c}\right\rangle_z$ using LES data. Purple and green curves and symbols correspond respectively to BASE and WEAK data which, despite having different turbulence scales (given in table 2.1), collapse after normalization.

value. We highlight that both BASE and WEAK simulations are shown in figure 2.9 in order to illustrate that normalizing the data by turbulence scales (such as the shear magnitude and the rms vertical velocity, which are different in each simulation as presented in table 2.1) causes the data to collapse. This points to the scaling relation $K \sim S$ as a way to generalize the results obtained in this study for shear flows having different turbulence intensities.

Although we do not have enough data to draw a definite conclusion about such relationship, the same linear scaling $K \sim S$ is observed in the canonical mixing layer (ML) (Wygnanski et al., 1970). Hence, it is reasonable to expect that the SAL behaves similarly. Nevertheless, the same shear magnitude produces a smaller eddy flux of momentum $\overline{u'w'}$ in our idealized SAL than it does in a ML, as discussed in the Supporting Information. This may be attributed to the fact that entrainment of laminar fluid into the shear layer is suppressed in the present study by the temperature inversions, which fundamentally differs from the ML dynamics.

It is expected that heavy particles whose settling speed w_s is comparable to the typical magnitude of turbulent fluctuations σ_w decorrelate with the carrier phase velocity due to the crossing-trajectory

effect. As a result, their eddy diffusivity decreases, which was modeled by Csanady (1963) as

$$K = K_0 \left(1 + \beta^2 \frac{w_s^2}{\sigma_w^2}\right)^{-1/2}, \tag{2.21}$$

where β is a constant typically chosen from 1 to 2, and K_0 is the diffusivity of non-settling particles. Note that we cannot determine K_0 with the flow setup adopted in this study, since $\overline{c} = c_0$ at all times and heights if $w_s = 0$. Instead, we use $K_0 = \langle K \rangle_{z,D_p}$ in order to compare our data with (2.21). In figure 2.9, however, our eddy diffusivity data appears to remain independent of particle size even for $w_s \sim \left\langle \sigma_w^2 \right\rangle_z^{1/2}$, instead of following the correction given by (2.21). This is possibly related to the fact that (2.21) was derived for homogeneous isotropic turbulence, which is not quite the case for our simulations due to the anisotropic character of the large-scale forcing, as well as the vertical heterogeneity induced by the boundary conditions. Moreover, non-local fluxes are not well represented by an eddy diffusivity closure, and large eddies spanning the entire layer depth h likely contribute significantly to dust transport in the simulated flows.

2.4.4 Implications for dust airborne lifetime and interpretation of SALTRACE data

Figure 2.10a presents the dimensionless residence time τ_R^* calculated from the analytical solution (2.16), along with values obtained directly from numerical integration of LES data, as a function of the Peclet number. In the turbulent limit (Pe $\to 0$), τ_R^* is twice as large as its laminar limit (Pe $\to \infty$), and most variability occurs in the range $1 \lesssim \text{Pe} \lesssim 10$, which coincides with the range where the Peclet numbers of the converged bins (#7 through #12) are located. The simulations were not long enough for τ_R to be calculated from its definition (2.14) for lighter particles. However, τ_R was also estimated for bins #3 to #12 by integrating the best-fit m^* curves (labeled "$K_\star$" in figure 2.6). These estimates were plotted as hollow symbols in figure 2.10. In general, the values obtained from LES data agree well with the theory, as can also be seen in figure 2.10b, where both estimates are plotted against each other. Deviations from the theory are slightly larger for smaller Pe (larger residence times), in which case K is a stronger function of z (see figures 2.7 and 2.8), and the assumption of a constant eddy diffusivity may introduce small errors.

Deleersnijder et al. (2006) also derived expressions for $\tau_R^*(\text{Pe})$ using non-uniform eddy diffu-

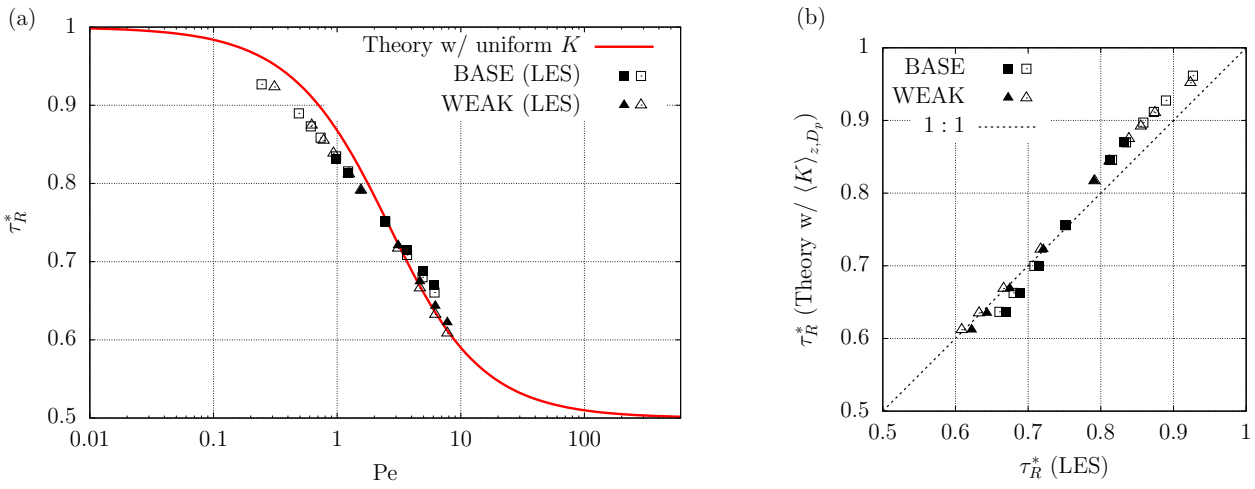

Figure 2.10: (a) Dimensionless residence time as a function of Peclet number as given by exact solution (2.16) (red curve) and obtained from numerical integration of m^* curves from LES for bins #7 through #12 (filled symbols). (b) Theoretical estimate of dimensionless residence time against same quantity obtained via numerical integration of LES data. Squares and triangles correspond respectively to BASE and WEAK. Note that the dimensionless data collapse for both flows, which have different eddy diffusivities, in agreement with the theory (which only depends on Pe). The simulations were not long enough to allow complete removal of particles smaller than those in bin #7, which is why LES estimates were also obtained from integration of the best-fit m^* curves (empty symbols).

sivity profiles. The resulting residence times, however, were not much different from the values given by (2.16), which assumes uniform K. Instead, their results suggested that τ_R is rather robust to different diffusivity profiles, depending much more on their magnitude (since τ_R^* ends up being a function of the Peclet number only). Hence, it is reasonable that, although the diffusivity profiles for the flows simulated in this study decrease towards the laminar layers as shown in figures 2.7 and 2.8, equation (2.16) still provided excellent estimates of τ_R^*.

Figure 2.11a presents the residence time of aerosol particles with volume-equivalent diameter D_p in the LES flows, together with theoretical predictions given by (2.16) using $K = \langle K \rangle_{z,D_p}$ and $K = 0$, i.e., assuming laminar flow, which is intended to represent the estimate of a large-scale model that neglects turbulent mixing. Despite the small deviations of the theory from LES data (which are more visible in figure 2.10), it is clear that incorporating the effect of turbulent mixing greatly improves the estimation of the airborne lifetime of aerosols as opposed to assuming laminar flow. This is especially true for small particles, which settle more slowly, and hence are impacted

by the eddy motions for longer periods of time. The longer aerosol particles remain airborne, the more likely they are to affect climate and weather via radiative and cloud interactions.

In figure 2.11b, the squares indicate the size-resolved, suspended dust concentration ratio between the Caribbean region and West Africa estimated based on SALTRACE measurements. The curves in figure 2.11b present model predictions for the same quantity under different assumptions regarding dust asphericity and the presence or absence of turbulent mixing. The observed c^* data plotted here were calculated as the ratio between size distributions obtained in the SALTRACE Lagrangian experiment described in Weinzierl et al. (2017) (more details on the calculations are given in Appendix C). The theoretical estimates were multiplied by a dilution factor α (defined in equation (C.5)) intended to account for any process not represented in the model described in section 3.3 that affects all particle sizes equally. Such processes may include, for instance, horizontal flux divergence (i.e., dilution by lateral entrainment of non-SAL air into the dust plume due to synoptic-scale, horizontal motions in the atmosphere), since an air parcel leaving Africa disperses during its transatlantic transport and reaches several different locations in the Americas, as well as entrainment into the boundary layer and wet deposition. Downward turbulent mixing of dust at the SAL base into the MBL is known to be an effective dust removal mechanism from the SAL (Carlson et al., 1972; Weinzierl et al., 2017; Rittmeister et al., 2017), and LES of the boundary layer performed by Jähn et al. (2016) confirmed that it takes place in the Caribbean region at a rate dependent upon the magnitudes of the wind shear and temperature inversion between the SAL and the MBL. In fact, wet deposition and convective (turbulent) removal dominate in the Caribbean, whereas dry deposition is more important closer to the North African source regions (Ridley et al., 2012).

Despite the actual complexity of reality, which must be accurately represented if one is to explain measurements in detail, figure 2.11b shows that this simple model, which accounts for particle shape and turbulent mixing, explains to a good extent the otherwise rather surprising presence of super coarse Saharan dust in Barbados. Hence, incorporating the effects of free atmospheric turbulence and particle asphericity in large-scale models presents significant potential for improvement in aerosol long-range transport modeling. Note that, in the laminar case, accounting for particle asphericity simply shifts the largest particle size by a factor of $\chi^{1/2}$ (the well-mixed case is discussed in detail

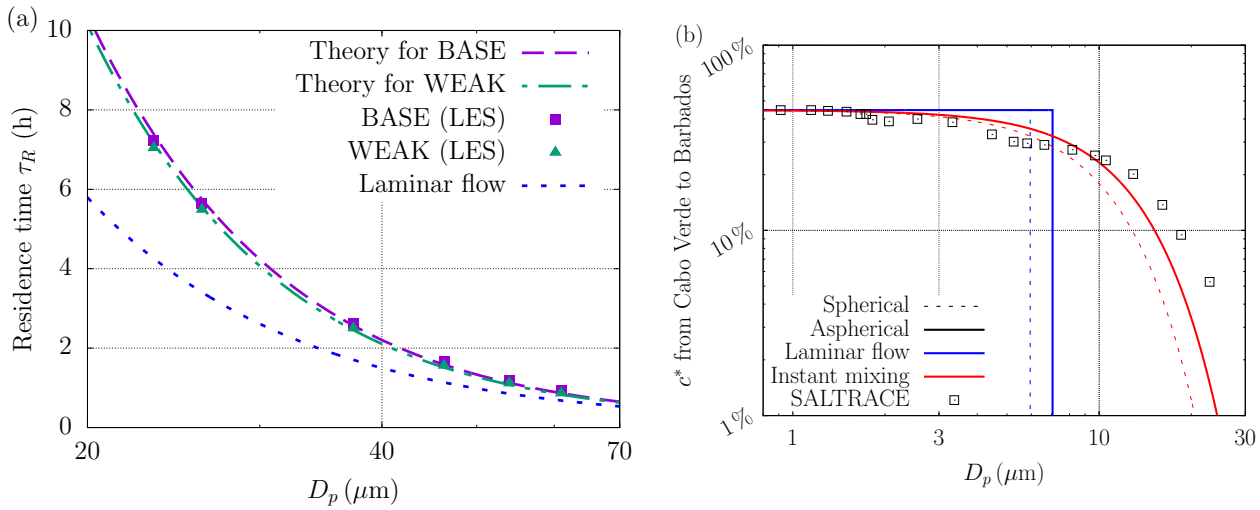

Figure 2.11: (a) Residence time (in hours) as a function of dust geometric diameter D_p obtained from our LES (squares and triangles for BASE and WEAK, respectively, illustrating different turbulence intensities), equation (2.16) with $\mathrm{Pe} = w_s h \langle K \rangle_{z,D_p}^{-1}$ (purple and green dashed lines), and the corresponding estimate when turbulent mixing is neglected (dotted blue line). (b) Size-resolved mass concentration ratio of dust particles remaining airborne from Cabo Verde to Barbados (squares) calculated based on SALTRACE data (Weinzierl et al., 2017, fig. 9) and model predictions assuming the presence and absence of turbulence, spherical and aspherical particles with $\chi = 1.4$, and a SAL thickness of $h = 4\,\mathrm{km}$. The calculations refer to particles reaching a measurement level located 1.3 km below the SAL top in Barbados. Theoretical estimates for c^* are multiplied by a constant factor α (see equations (C.5)–(C.8)) so as to match the measured data at small D_p, which is intended to account for plume dilution and any size-independent processes acting to reduce the concentrations measured in Barbados.

in the Supporting Information).

Several reasons might help explain the remaining discrepancy between models and measurements of coarse dust in figure 2.11b. For instance, size-dependent processes other than dry deposition, such as cloud processing, which contributes to producing larger particles (Wurzler et al., 2000), are capable of altering the dust size distribution in the SAL. Hence, it is possible that the dilution effect was overestimated, and multiplying the model estimates by a factor closer to unity instead would indeed make the theoretical curves approach the observations. Other possible factors leading to mismatch between model and observations include horizontal variability of dust concentration measured in the SAL, the detection of additional aerosol from different sources in the Caribbean, and the effect of electric forces counteracting gravity, not to mention other sources of uncertainty intrinsic to field measurements.

We highlight that simple knowledge of the residence time given by (2.16) is not enough to determine the suspended aerosol concentration fraction $c^* = \alpha m^*$ at a given instant t and height z as plotted in figure 2.11b, which underlines the relevance of the complete analytical solution for c^* given by (2.11). Moreover, equation (2.12) can be used to compute the difference Δm^* between the actual airborne dust mass fraction at any given time and m^* in a laminar flow at the same instant, i.e.,

$$\Delta m^* = \begin{cases} m^*\left(t^*, \mathrm{Pe}\right) - \left(1 - t^*\right), & t^* \leq 1, \\ m^*\left(t^*, \mathrm{Pe}\right), & t^* > 1. \end{cases} \tag{2.22}$$

This is illustrated for different travel times t, eddy diffusivities K, and particle sizes D_p in figure 2.12. First, note that, while the effect of turbulence on the dust airborne lifetime increases monotonically with decreasing particle size (see equation (2.16), and figures 2.10a and 2.11a), Δm^* has a maximum at intermediate particle sizes. After a given transport time, small enough particles are not affected by turbulence because they barely settle. Since in this case no gradient develops for turbulent mixing to act on, Δm^* tends to zero as the particle size decreases. For example, note in figure 2.11b that the curves for laminar and turbulent flow coincide for $D_p \lesssim 3\,\mu$m. On the other hand, Δm^* also vanishes for large enough particles at long enough times, in which case all particles of a given size are completely removed from the SAL, no matter how strong turbulent mixing is. For instance, one can see in figure 2.11b that particles greater than about $30\,\mu$m are completely removed after the 5-day window in both laminar and instant-mixing conditions. As a result, Δm^* peaks at intermediate particle sizes. In the case of the SALTRACE Lagrangian experiment, we notice that the 5-day curve in figure 2.12 indeed shows that Δm^* peaks for D_p in the range 10–$20\,\mu$m.

The peak in Δm^* occurs at $t^* = 1$, regardless of the value of K. This means that, at any time t, particles with $w_s = h/t$ are the most affected by turbulent mixing. In other words, the instant when the effect of turbulence on a given particle size can be most appreciated is $t = \tau_g$, i.e., when gravity would have finished removing those particles from a laminar SAL. Therefore, at shorter times, heavier particles are more affected, whereas smaller particles are more affected over longer times. Finally, while $\Delta m^*\left(D_p\right)$ is greatest when $K \to \infty$ (always peaking at $\Delta m^* = \mathrm{e}^{-1}$ at $t^* = 1$), it is smaller for finite diffusivity values. In this case, Δm^* increases with increasing travel times (as turbulent mixing has more time to act), therefore impacting small-Pe particles more significantly.

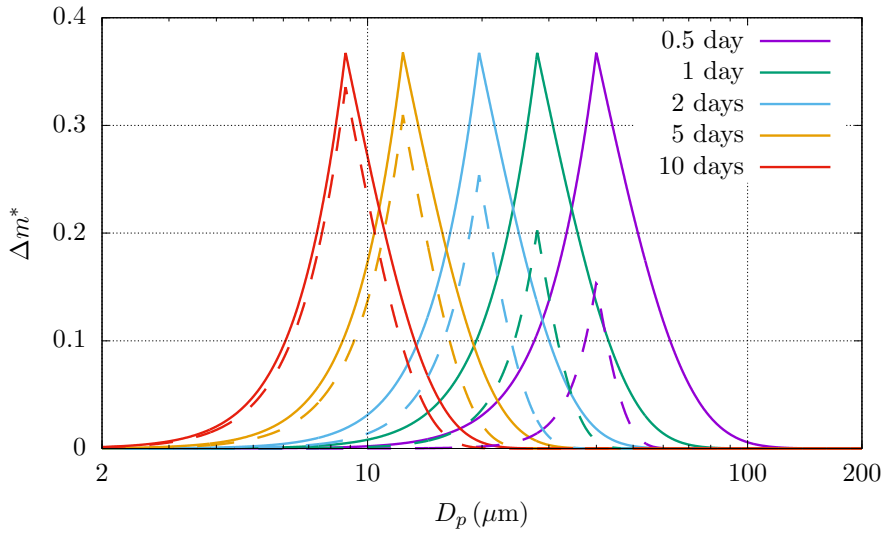

Figure 2.12: Additional SAL dust mass fraction as a result of turbulent mixing according to equation (2.12) in a layer of thickness $h = 4\,\mathrm{km}$ after different travel times (colors) for instant mixing, i.e., $K \to \infty$ (solid lines), and $K = 32.6\,\mathrm{m}^2/\mathrm{s}$ (dashed lines).

2.5 Conclusions

In spite of the importance of coarse desert dust in the Earth system, current models consistently underestimate its concentration in the atmosphere. With this motivation, the present study employed a simple advection-diffusion model to represent the competing effects of settling and turbulent mixing on the suspended lifetime of dust in the SAL. The results were validated with LES data for particles in a turbulent shear layer contained between stable inversions (much like the SAL). Despite the height dependence of the eddy diffusivity and the potential contribution of non-local fluxes (both factors being especially relevant for small particles) in the numerical simulations, this simple model provided reasonable estimates for low-order moments and integral measures such as the size-resolved suspended aerosol mass over time, as well as the concentration profiles and residence time of particles in the atmosphere. However, it is possible that this model becomes inadequate for very small particles whose dominant removal mechanism from the turbulent layer is detrainment (rather than gravitational settling).

The particle airborne lifetime τ_R depends solely on the particle Peclet number, is rather independent from the diffusivity profile, and can increase by up to a factor of 2 due to turbulent mixing when compared to laminar flow. A constant diffusivity value, scaling with the flow mean shear, i.e., $K \sim S$,

was enough to describe the behavior of all size bins, though it is possible that this is no longer the case for particles larger than those considered in this study, for which the crossing-trajectory effect may start manifesting.

Furthermore, our simplified analytical representations of turbulent mixing and aerosol asphericity were able to explain to a considerable extent the presence of super coarse Saharan dust in the Caribbean observed in the SALTRACE Lagrangian experiment measurements. Nevertheless, this coarse dust long range transport conundrum is not yet completely solved, and the problem requires further investigation. A better particle shape parametrization, as well as a model including electric forces, may bring theoretical estimates closer to observations.

Moving forward, it might be of interest to add other processes to the prototype turbulent shear flow simulated in the present study, so that it becomes a more realistic representation of some particular flow of interest. For instance, one can incorporate buoyancy effects (including feedback from the dust field due to particle-radiation interaction) to simulate the SAL more accurately. In fact, a more complete SAL representation need also include realistic PGF profiles, which could be utilized in order to determine whether turbulence actually develops in the SAL and what the associated TKE budget is. In the Caribbean region, however, deep convection, wet deposition and mixing with the boundary layer also play a fundamental role in the fate of the dust size distribution, and the flow dynamics is expected to be rather different from the that of the numerical simulations presented in this study.

CHAPTER 3

Shear-induced vertical mixing in a stratified Saharan Air Layer

Authors: Rodrigo Rodakoviski and Marcelo Chamecki.

Abstract:

Recent studies have suggested vertical turbulent mixing in the Saharan Air Layer (SAL) as a possible mechanism explaining the observed long-range transport of coarse Saharan dust particles. Nevertheless, buoyancy profiles measured in the SAL typically display some degree of stable stratification, implying that any turbulence in this elevated layer must be stratified. In this paper, we idealize the SAL as a stratified shear layer where turbulence is triggered by the instability of the African Easterly Jet, and stratification occurs due to lateral entrainment of stratified, non-SAL air from the surroundings. Analytical solutions obtained for this idealized set-up are combined with LES data and results from the stratified turbulence community to produce a simple parameterization of the eddy diffusivity in a weakly stratified SAL as a function of layer depth, shear magnitude, and gradient Richardson number Ri_g. Our results suggest that even small eddy diffusivity values are enough to significantly impact the airborne lifetime of particles as large as super-coarse dust (with a diameter greater than $10\,\mu$m). Therefore, even after accounting for the stabilizing effect of buoyancy, turbulent mixing in the SAL remains a likely explanation for the long-range transport of coarse Saharan dust. Moreover, the diffusivities calculated for our elevated SAL set-up decay faster with Ri_g than typical ABL models, highlighting the importance of employing appropriate parameterization schemes in climate models to represent slow processes (particularly affected by small diffusivities values) accurately.

3.1 Introduction

Coarse desert dust particles have repeatedly been observed in very far ($\sim 10^3$ km) locations from their sources (Betzer et al., 1988; Weinzierl et al., 2017; Van Der Does et al., 2018). This has long been a mystery, since simple calculations based on Stokes' graviational settling rates (which assumes dust falling in a laminar environment) predict that such particles should be removed from the atmosphere farily quickly, which would limit their horizontal transport. Moreover, climate models typically employ similar simple parameterizations for dust settling, and therefore tend to overestimate dust deposition rates (Maring et al., 2003; Kim et al., 2014). Given that dust interacts with clouds (Karydis et al., 2011; Boose et al., 2016) and radiation (Kok et al., 2017; Otto et al., 2007), it is fundamental that climate models accurately parameterize its airborne lifetime. This is especially true for dust in the coarse mode (with diameter $> 5\,\mu$m), which produces a net warming of the climate system due to absorption of both short-wave (SW) and long-wave (LW) radiation but is severely underestimated by models (Adebiyi et al., 2020).

About half of the global loading of dust has its origin in Northern Africa (Kok et al., 2021). Dust emitted by the Sahara Desert surface is distributed vertically by turbulent mixing in a deep, convective boundary layer whose capping inversion reaches about 6 km above the ground (Garcia-Carreras et al., 2015). Especially in the summer months, the African Easterly Jet (AEJ) transports this dust-laden Saharan air over the tropical North Atlantic (figure 3.1), above the cool marine layer, forming the elevated Saharan Air Layer (SAL) (Carlson, 2016). As a result, the SAL is an initially well-mixed layer capped above and below by stable inversions, with its bottom inversion typically about 1 to 2 km above the ocean surface. The barotropic and baroclinic instability of the AEJ generates African Easterly Waves (AEWs, like the one in figure 3.1), which periodically contribute to the transport of dust (Nathan et al., 2022).

In the SAL, multiple hypotheses have been suggested to explain the long-range transport of coarse dust. These include aspherical particle shapes (Huang et al., 2020; Mallios et al., 2020), uplift in deep convection events such as thunderstorms or tropical cyclones (Van Der Does et al., 2018), as well as electrical fields (Toth III et al., 2020; Mallios et al., 2022) and vertical turbulent mixing within the elevated SAL (Rittmeister et al., 2017; Gutleben et al., 2021). In a previous paper

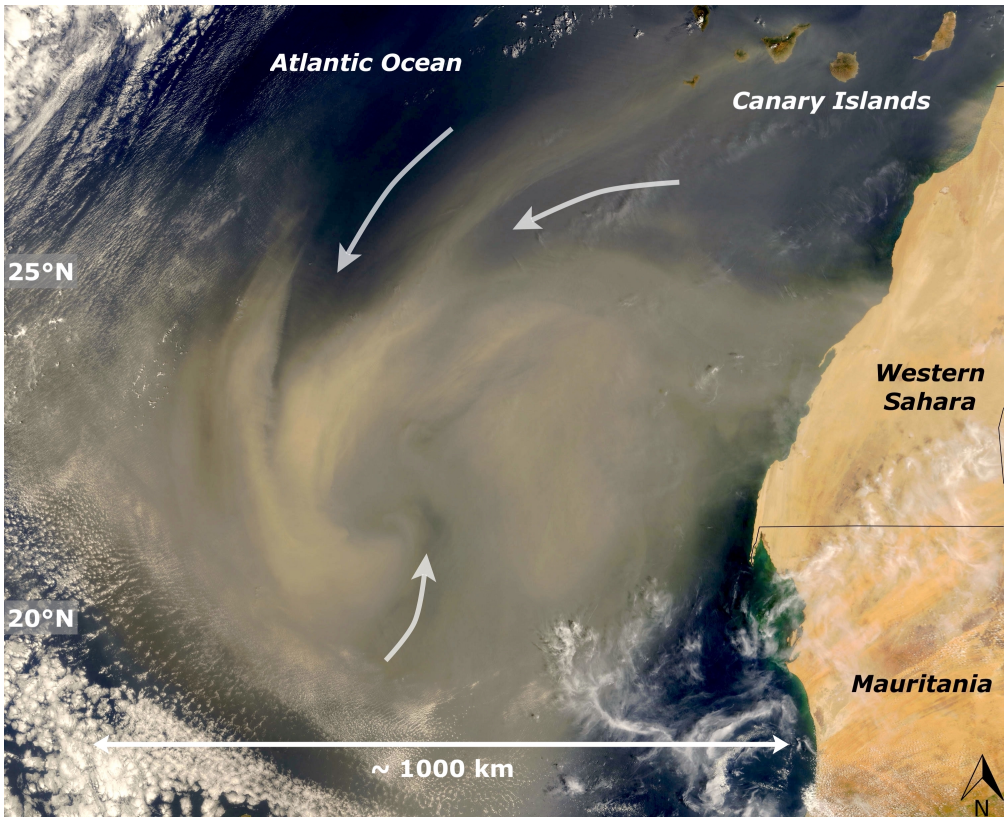

Figure 3.1: Saharan dust plume over the Atlantic Ocean off the west coast of Africa captured by the Moderate Resolution Imaging Spectroradiometer (MODIS) onboard the Terra satellite on September 4, 2005 (color enhanced for better visualization). The large-scale eddy is several hundred kilometers wide, and variations in dust concentrations within it are visible, as well as lateral entrainment of dust-free air into the plume (indicated by the curved arrows). Credit: NASA's Earth Observatory (adapted).

(Rodakoviski et al., 2023), we showed that, together with dust asphericity, small-scale turbulent mixing in the SAL helps explain the long-range transport of coarse dust to a great extent.

Previous investigations have suggested that turbulence could be produced in the SAL interior by convective forcing mechanisms. In their idealized model, Gasteiger et al. (2017) assumed that SAL convection was triggered by dust sunlight absorption. Ryder (2021) showed that the nearly well-mixed thermodynamical profiles in the SAL are associated with a positive anomaly in water vapor concentration in the upper SAL. The efficient emission of LW radiation by water vapor can thus cool the SAL top and produce convective motion. In order for these to be valid turbulence producing mechanisms in the SAL, the overall heating rate profile $\dot{q}(z)$ resulting from radiative interactions must decrease with height z. One can expect local gravitational instabilities to cause the flow to overturn in sublayers where $\mathrm{d}_z\dot{q} < 0$, leading to a local adjustment of the lapse rate to a neutral profile in those sublayers (Frank et al., 1993). Gutleben et al. (2019, fig. 4) showed that dust radiative interactions have a relatively small contribution to the overall heating rate compared to cooling due to water vapor LW emission. Using lidar observations of moisture near the Caribbean (in the western North Atlantic), their calculated $\dot{q}(z)$ profile shows strong cooling at the top, suggesting convective mixing in the SAL. Otto et al. (2007, fig. 10), on the other hand, using radiosonde measurements of water vapor near the Canary Islands (in the eastern North Atlantic), found $\mathrm{d}_z\dot{q} > 0$ for the most part, suggesting a stratifying effect instead. This could be an indication that $\dot{q}(z)$ may change with longitude as the SAL moves over the Atlantic, and also across different dust events.

Whereas there appears to be some uncertainty regarding the overall effect of $\dot{q}(z)$, temperature measurements consistently show that the SAL is generally weakly stratified rather than perfectly well-mixed (e.g., Ryder et al., 2018; Gutleben et al., 2019; Gutleben et al., 2021; Ryder, 2021). This can also be seen in the profiles of potential temperature θ in figure 3.2a. Although well-mixed sublayers (possibly resulting from local shear or gravitational instabilities) are visible in individual observations, the ensemble-averaged profile clearly shows an overall stable stratification in the SAL. Hence, even though the SAL is sometimes described as a well-mixed layer (which can be a useful approximation in some contexts), it is more accurately described as being *nearly* well-mixed.

Whereas it is possible that the SAL might sometimes depart the African continent already with

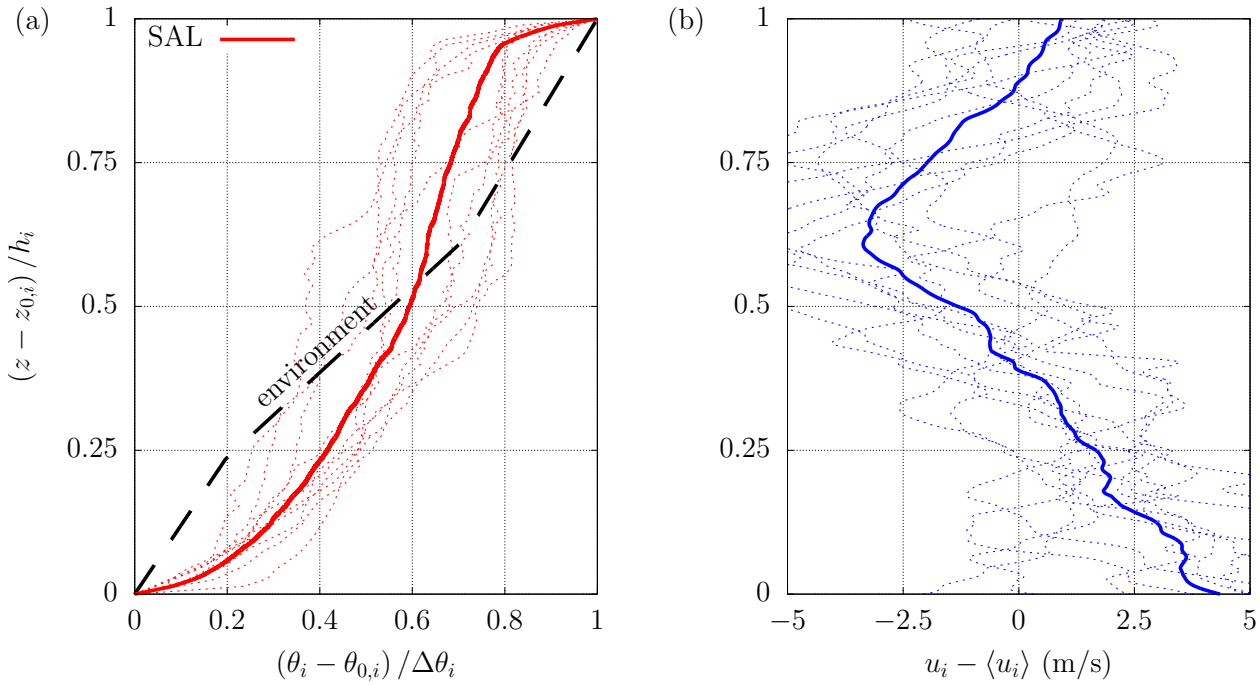

Figure 3.2: (a) Normalized potential temperature profiles reveal that the SAL interior (red lines) is more weakly stratified than the surrounding air (black, dashed lines). (b) SAL zonal winds have strong vertical shear due to the AEJ. Thin, dotted lines are individual observations (each denoted by an index *i* on the labeled axes), whereas the thick lines correspond to ensemble averages. Data were collected during the SALTRACE and AER-D field campaigns, as described in Rittmeister et al. (2017) and Ryder et al. (2018), respectively. The environmental profile was taken as the standard tropical profile defined in Anderson et al. (1986). Data processing details are available in Appendix D.

some initial (weak) stratification, the idea of vigorous and persistent convective mixing spanning this elevated layer in its full depth is inconsistent with recurrent observations of weak stability. Hence, if radiative interactions do not have a widespread net stratifying effect, there must exist another stratification mechanism which dominates.

In the present study, we hypothesize that lateral entrainment of stratified, dust-free air into SAL plumes (as indicated by curved arrows in figure 3.1) contribute to the observed stable SAL profiles. As the SAL mixes with the non-SAL air in its surroundings, properties such as momentum, buoyancy and dust concentrations are mixed. For example, using data from Weinzierl et al. (2017), Rodakoviski et al. (2023) showed that fine dust concentrations are diluted to a factor $\simeq 0.45$ as the SAL moves across the Atlantic due to lateral spreading of the plume. Similarly, Saharan air that

is initially well-mixed (due to boundary-layer turbulence over land) has a temperature anomaly relative to the stratified free-troposphere over the tropical Atlantic. Mixing such two air masses together would result in a profile with intermediate stratification, which is consistent with the weakly stratified SAL profile shown in figure 3.2a.

One can expect properties entrained at large scales to cascade down to scales comparable to the SAL height h as a result of a series of inertial and shear instabilities, similarly to the processes that generate clear-air turbulence (CAT) in the upper atmosphere (Dörnbrack et al., 2022). Moreover, the presence of stable stratification suggests that any SAL turbulence is generated mechanically rather than convectively. This is a reasonable conjecture, since the AEJ produces strong vertical wind shear in the SAL interior (Bercos-Hickey et al., 2020), as seen in figure 3.2b. In nature, stratified shear turbulence away from solid boundaries is commonplace. Examples include the upper atmosphere near the Jet Stream (Tse et al., 2003), as well as the equatorial upper ocean, where shear is induced by the Equatorial Undercurrent (Peters et al., 1988). Some of the highest diapycnal diffusivities in the ocean are produced by the shear instability of the oscillating tidal flow exchanging water between the Atlantic and Mediterranean basins (Gregg, 1998).

The stable buoyancy configuration in the SAL tends to reduce vertical eddy mixing rates due to the work against gravity necessary to overturn stably stratified fluids. Hence, it can limit the potential of turbulence to increase the airborne lifetime of dust particles. Our previous study (Rodakoviski et al., 2023) modeled the SAL as a neutral layer. Therefore, the goal of the present study is to estimate by how much turbulent mixing in the SAL is reduced due to stable stratification, and to determine whether turbulence is still a reasonable explanation for the long-range transport of coarse Saharan dust given more realistic conditions. To that end, we present a brief review on relevant stratified turbulence results in section 3.2. Next, we develop a theoretical framework and a large-eddy simulation (LES) set-up for a stratified SAL-like flow in sections 3.3 and 3.4, respectively. Results obtained from these models and their implications for dust transport are discussed in section 3.5, where we show that turbulence can still play an important role in keeping SAL dust aloft despite stable stratification. Concluding remarks are made in section 3.6.

3.2 Some stratified turbulence results

3.2.1 Averaging notation

Before we proceed, a note on the averaging notation used in the rest of this paper is appropriate. Our idealized flow (presented in section 3.3) is statistically stationary and homogeneous in the horizontal directions x, y. Hence, for any variable η, its Reynolds average (denoted by an overbar, i.e., $\overline{\eta}$) is equivalent to its average in x, y, t, where t is time. A prime denotes a turbulent fluctuation $\eta' = \eta - \overline{\eta}$. Vertical averages (in the z-direction) are indicated by angled brackets, i.e., $\langle \eta \rangle$. The velocity vector is (u, v, w), where w is vertical velocity. In what follows, stratified turbulence parameters (such as the mixing coefficient Γ) are defined in a way that is most suitable to the problem at hand.

3.2.2 Parameter space and flow regimes

Scale analysis reveals that, at scales comparable to the SAL height h, the effects of Earth's rotation on the flow dynamics are negligible, and the so-called *stratified turbulence* regime takes place. Indeed, by choosing $h \simeq 2\,\mathrm{km}$, a Coriolis frequency of $f \simeq 5 \times 10^{-5}\,\mathrm{s}^{-1}$ for the tropical North Atlantic, and a typical velocity increment across the AEJ of $\Delta\overline{u} \simeq 10\,\mathrm{m\,s}^{-1}$, one calculates a Rossby number $\mathrm{Ro} \sim 10^2$. This is in contrast to the synoptic scales of AEWs (figure 3.1), whose horizontal dimension is $\sim 10^3\,\mathrm{km}$ and for which $\mathrm{Ro} \sim 10^{-1}$, indicative of geostrophic turbulence and strong influence of Earth's rotation. A forward energy cascade from such large scales is expected to provide energy to small-scale, stratified turbulence in the SAL.

For a given material (e.g., air or water) with fixed Prandtl number Pr, a stratified shear flow can be described by the gradient Richardson, Froude, and buoyancy Reynolds numbers (Caulfield, 2021), here defined as

$$\mathrm{Ri}_g = \frac{N^2}{S^2}, \quad \mathrm{Fr}_T = \frac{1}{\tau_e N}, \quad \mathrm{Re}_b = \frac{\langle \varepsilon \rangle}{\nu N^2}, \tag{3.1}$$

respectively. In (3.1), N and S are the background buoyancy and shear frequencies, ν is molecular viscosity, and $\tau_e \equiv \langle k \rangle / \langle \varepsilon \rangle$ is the eddy turnover time, where k and ε are the turbulence kinetic energy (TKE) and its viscous dissipation rate. Note that Fr_T defined in (3.1) is equivalent to a horizontal Froude number if one chooses $U \equiv \langle k \rangle^{1/2}$ and $\ell_h \equiv U^3 / \langle \varepsilon \rangle$ as velocity and horizontal

length scales. If the Reynolds number is defined as $\mathrm{Re} = \ell_h U/\nu$, it follows that $\mathrm{Re}_b = \mathrm{ReFr}_T^2$.

When $\mathrm{Re}_b \lesssim 1$, a regime of viscously-affected stratified turbulence takes place, in which most of the energy dissipation occurs due to vertical shearing of nearly horizontal pancake-like vortices in the flow (Bartello et al., 2013). Many earlier numerical and experimental studies achieved small Fr_T at the expense of small Re, and therefore were in this regime (e.g., Lin et al., 1979; Herring et al., 1989). On the other hand, if Re_b is large but $\mathrm{Fr}_T \gtrsim 1$, one finds a regime of weakly stratified turbulence, in which buoyancy is transported by the flow similarly to a passive scalar (Garanaik et al., 2019; Issaev et al., 2022).

One regime of particular interest for geophysical flows is that defined by the distinguished limit $\mathrm{Re} \gg 1$, $\mathrm{Fr}_T \ll 1$, such that $\mathrm{Re}_b = \mathrm{ReFr}_T^2 \gg 1$. This is the expected regime in the middle atmosphere and the upper ocean given typical conditions (Brethouwer et al., 2007). It is a regime of strongly stratified turbulence, also referred to as "layered anisotropic stratified turbulence" (LAST) in the geophysical community (Falder et al., 2016), in which relatively well-mixed layers of depth $\ell_z \sim U/N$ tend to form, separated by sharp interfaces of stronger stratification (Caulfield, 2021). This implies $\mathrm{Fr}_T \sim \ell_z/\ell_h$ in this regime. Mixing and energy dissipation are very intermittent in space and time, as they mostly take place within transient turbulent patches embedded in a rather quiescent flow (Portwood et al., 2016). These regions of small (or negative) *local* gradient Richardson number Ri_ℓ are responsible for much of the flow forward energy cascade, which is nearly isotropic at small enough scales despite strong stratification (provided that $\mathrm{Re}_b \gg 1$).

In order to determine where the SAL falls within this parameter space, ideally one would use the definitions in (3.1) together with robust estimates of $\langle k \rangle$ and $\langle \varepsilon \rangle$. These could be obtained from extensive measurements of $k(z)$ and $\varepsilon(z)$ taken over several locations, for several dust events. In the lack of such a comprehensive turbulence dataset, however, we use the mean flow quantities $\Delta\overline{u} \simeq 10\,\mathrm{m\,s^{-1}}$ and $h \simeq 2\,\mathrm{km}$ in lieu of U and ℓ_h, respectively, for a rough estimate. Using $\nu = 1.7 \times 10^{-5}\,\mathrm{m^2\,s^{-1}}$ and $N \simeq 0.009\,\mathrm{s^{-1}}$, one finds $\mathrm{Re} \sim 10^9$ and $\mathrm{Fr}_T \simeq 0.6$. Here, N was estimated based on the SAL interior stratification (excluding the inversion layers at its edges) from the SALTRACE dataset described in Rittmeister et al. (2017) (also used to produce figure 3.2a). For comparison, the standard tropical profile from Anderson et al. (1986) has $N \simeq 0.014\,\mathrm{s^{-1}}$ at similar heights to the SAL, whereas $N > 0.015\,\mathrm{s^{-1}}$ has been usually observed near the tropopause

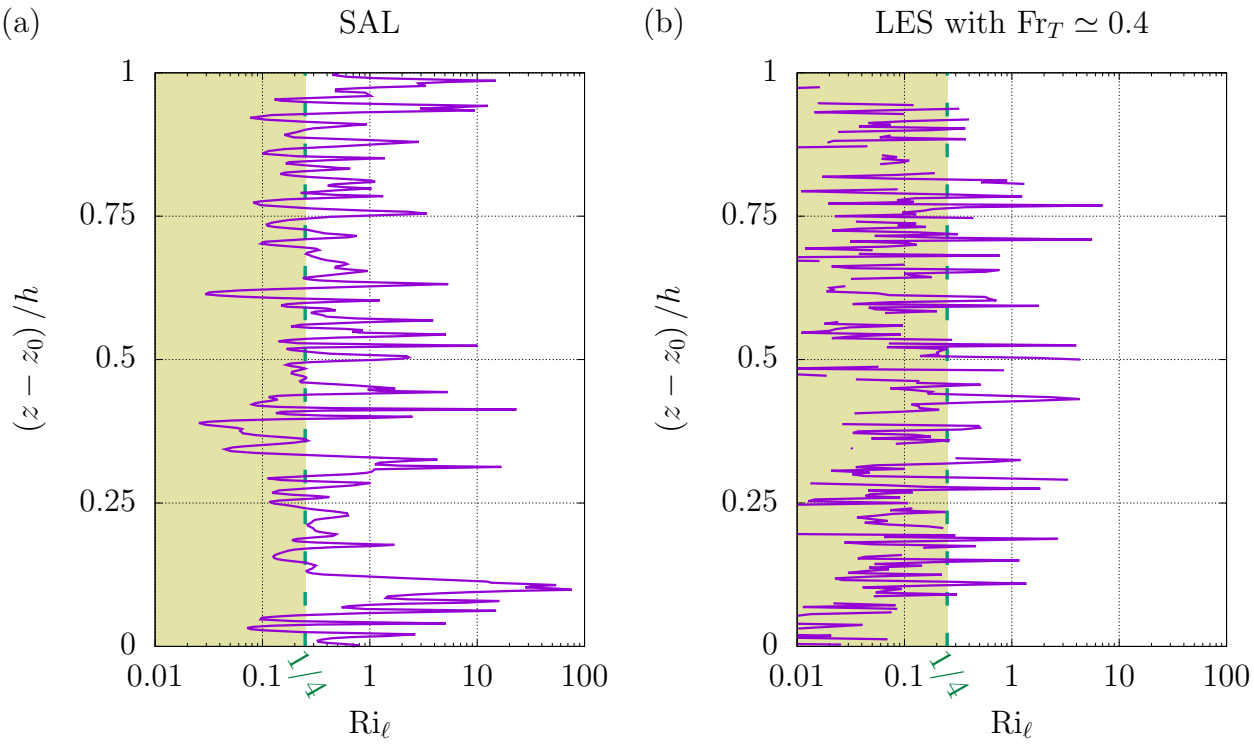

Figure 3.3: Vertical profile of instantaneous, local Richardson number based on (a) SAL data collected by the dropsonde released at 13:17 UTC from AER-D flight b932 and (b) LES data from run P1H3 (as described in section 3.4). Small values suggest local shear instabilities. The range $\mathrm{Ri}_\ell < 0.25$ of linear instability according to the Miles–Howard criterion is indicated for reference (Miles, 1961; Howard, 1961), but turbulence can exist at Ri_ℓ values exceeding unity (Galperin et al., 2007).

(Schumann et al., 1995; Dörnbrack et al., 2022).

Whereas it is clear that the SAL has large Re (as usual for geophysical flows), estimating Fr_T is a more subtle task. For instance, consider the instantaneous profile of local Richardson number calculated from SAL data shown in figure 3.3a. When compared to the LES profile in figure 3.3b, calculated for a run with $\mathrm{Fr}_T \simeq 0.4$ (as described in section 3.4), it is evident that the SAL has larger Ri_ℓ values. This suggests that, at least sometimes, the SAL might be more strongly stratified than our rough estimate based on mean flow parameters indicates. Hence, in order to estimate a lower bound on Fr_T, we assume the LAST regime, in which Fr_T scales with the aspect ratio of turbulent structures, ℓ_z/ℓ_h. Using the bulk aspect ratio of the SAL as a rough approximation instead (with a horizontal lengthscale of $\sim 10^3$ km as indicated in figure 3.1), we estimate $\mathrm{Fr}_T \sim 10^{-3}$ as a lower limit. Hence, if we admit that Fr_T may range from 10^{-3} to 10^0, it follows that Re_b ranges

from 10^3 to 10^9. Therefore, given the existing variability in SAL conditions and limited turbulence observations, it seems plausible to admit that turbulence in the SAL may be anywhere from nearly neutral to strongly stratified.

3.2.3 Parameterization of turbulent mixing

We now turn to the closure problem of stratified turbulence. For a horizontally homogeneous flow with no subsidence (i.e., $\overline{w} = 0$), the TKE balance is

$$\partial_t k = P - \partial_z T - B - \varepsilon. \tag{3.2}$$

Here, P is shear production, T represents transport terms, and the buoyancy flux $B = -\overline{w'b'}$ is the rate of conversion of TKE into potential energy (where $b = g(\theta - \theta_0)/\theta_0$ is the buoyancy field, $g = 9.8\,\mathrm{m\,s^{-2}}$ is the acceleration due to gravity and θ_0 is a reference temperature). Transport terms vanish in a vertical average sense (assuming no boundary fluxes), and under stationary conditions, $\langle P \rangle = \langle B \rangle + \langle \varepsilon \rangle$. The mixing coefficient Γ and the flux Richardson number Ri_f are defined as

$$\Gamma \equiv \frac{\langle B \rangle}{\langle \varepsilon \rangle}, \quad \mathrm{Ri}_f \equiv \frac{\langle B \rangle}{\langle P \rangle}, \quad \Gamma = \frac{\mathrm{Ri}_f}{1 - \mathrm{Ri}_f}, \tag{3.3}$$

where the last relationship assumes stationary conditions.

The scaling of Γ with different dimensionless quantities has been an active topic of discussion in the stratified turbulence community, in particular because it can be used to estimate momentum and heat diffusivities ($K_u = P/S^2$ and $K_\theta = B/N^2$, respectively), which are related to Γ via

$$\frac{\langle K_u \rangle}{\nu} = (1 + \Gamma)\,\mathrm{Ri}_g \mathrm{Re}_b, \quad \frac{\langle K_\theta \rangle}{\kappa} = \mathrm{Pr}\Gamma \mathrm{Re}_b, \tag{3.4}$$

where κ is the molecular diffusivity for heat. At least in principle, Γ is a function of all dimensionless parameters defined in (3.1), and different scaling relations have been found. Analysing DNS and laboratory data, Shih et al. (2005) found $\Gamma \sim \mathrm{Re}_b^{-1/2}$ at large Re_b and weak stratification. This scaling has also been reproduced by recent studies (e.g., Salehipour et al., 2015). At lower Re_b values and stronger stratification, however, Shih et al. (2005) found $\Gamma \simeq 0.2$, which was suggested by Osborn (1980) as an upper bound for the mixing coefficient. On the other hand, Maffioli et al.

(2016) and Garanaik et al. (2019) have argued in favor of Froude-number scalings instead. They found $\Gamma \sim \mathrm{Fr}_T^{-2}$ for weak stratification and $\Gamma \sim \mathrm{Fr}_T^{-1}$ for intermediate Fr_T values, with an asymptotic value close to 0.3 as $\mathrm{Fr}_T \to 0$. Such Froude-number scalings have also been observed in recent studies (e.g., Issaev et al., 2022), although Young et al. (2022) found better data collapse after incorporating the dimensionless shear rate $S^* = \tau_e S$ into them.

The existence of different scalings in the literature is at least partly due to the multitude of dimensionless parameters influencing the problem. A variable parameter across different studies may act as a confounding variable, and hidden correlations between variables limit the region of the full parameter space that can be explored (Caulfield, 2021). Therefore, disentangling the dependence of Γ on the various dimensionless parameters of stratified turbulence is not a trivial task. In particular, the behavior of Γ in the LAST regime is still a rather controversial question, especially due to the challenge of simultaneously achieving small Fr_T and large Re_b in computer or laboratory experiments. As discussed in section 3.4, numerical studies must resolve a broad range of lengthscales in this regime. Moreover, the strong intermittency of LAST increases the computational cost of computing representative averages of flow properties.

In order to determine the relevant scaling for parameterizing mixing in the SAL, we turn our attention to an idealized SAL flow with similar forcing but simple enough to provide some analytical results. This stratified shear flow is forced by a height-varying pressure-gradient force (PGF) and a net stabilizing heat flux, as described in section 3.3. LES results for this flow are presented in section 3.4.

3.3 Theory for stratified SAL flow

3.3.1 Problem set-up

The Reynolds-averaged equations of motion for an incompressible, stationary, horizontally homogeneous flow forced by a mean PGF in the x-direction and temperature nudging are

$$\begin{aligned} \overline{v} = \overline{w} &= 0, \\ \mathrm{d}_z \overline{u'w'} &= -\partial_x \overline{\phi}, \\ \mathrm{d}_z \overline{w'^2} &= -\partial_z \overline{\phi} + \overline{b}, \\ \mathrm{d}_z \overline{w'\theta'} &= \frac{\Theta_{env} - \overline{\theta}}{\tau_h}, \end{aligned} \tag{3.5}$$

where the Coriolis force was neglected at the scales of interest (following the scale analysis from section 23.2.2), as well as molecular diffusion terms. In (3.5), $\phi = p/\rho_0$ is the geopotential function (where p is pressure and ρ_0 is a reference density), τ_h is the lateral entrainment timescale, and $\Theta_{env}(z)$ is the potential temperature profile in the environment surrounding our domain, from which air is entrained into the SAL. Here, it is assumed to be the linear profile

$$\Theta_{env}(z) = \theta_0 + \Delta\Theta \frac{z}{h}. \tag{3.6}$$

Our prototype SAL is defined between $z = 0$ and h, so $\Delta\Theta$ is the overall temperature jump in the surroundings. Because the inversion layers above and below the SAL limit vertical motion and mixing at its edges, we use the free-slip, adiabatic boundary conditions

$$\overline{w} = \partial_z \overline{u} = \partial_z \overline{v} = \partial_z \overline{\theta} = 0 \quad \text{at} \quad z = 0, h. \tag{3.7}$$

Continuity with the above boundary conditions justifies $\overline{w} = 0$ in (3.5).

In our idealized SAL, mean shear is forced by a vertically-varying horizontal PGF. This is motivated by the fact that, in the actual SAL, the AEJ is primarily in geostrophic balance at the large scales, being forced by a PGF that varies with height due to the meridional gradient in virtual temperature produced by surface conditions (Cook, 1999a). At the small scales being considered in this study, however, the PGF profile is just used to force shear turbulence. For a stationary solution

satisfying (3.5) to exist, it must satisfy the integral constraint

$$\int_0^h \partial_x \overline{\phi}\, \mathrm{d}z = -\overline{u'w'}\Big|_{z=0}^{h} = 0 \tag{3.8}$$

Here, we choose the linear profile

$$-\partial_x \overline{\phi}\,(z) = M\left(1 - \frac{2z}{h}\right), \tag{3.9}$$

where the magnitude M sets how fast the PGF changes in z.

The RHS of the temperature equation in (3.5) nudges the SAL temperature profile to that of its surroundings at timescale τ_h. This is a simplified representation of the heating rate resulting from lateral entrainment of buoyancy properties that cascade down from large, quasi-geostrophic scales to the scales of stratified turbulence. In reality, lateral entrainment causes horizontal divergence of advective heat fluxes at large scales, but we parameterize it as a source term in (3.5) for simplicity (which is also compatible with horizontal homogeneity). Lateral entrainment also mixes momentum, but we neglect such a nudging term in the momentum equations. Because the SAL is stratified after all (figure 3.2a), we also neglect the radiative heating rate term $\dot{q}\,(z)$ compared to lateral entrainment. These simplifications reduce the size of the parameter space that defines the idealized problem, and make it possible to find an approximate solution to it.

The system (3.5) contains no time derivatives, even though conditions for a Lagrangian air mass in the SAL change with time as it moves westward, away from the African coast. We assume that background flow properties evolve slowly enough so that turbulence within such a parcel is in local equilibrium with its forcing (PGF and internal heating) at all times. This eliminates the dependence of the flow dynamics on its particular history, so mixing coefficients and other turbulence properties can be uniquely determined by a small set of forcing parameters (namely, h, M, τ_h, and $\Delta b_{env} \equiv g\Delta\Theta/\theta_0$).

3.3.2 Closure

We will use an eddy diffusivity closure for the eddy fluxes in (3.5). The momentum eddy diffusivity is defined based on the streamwise velocity as $K_u = \overline{u'w'}/S$, with $S \equiv |\mathrm{d}_z\overline{u}|$. It is related to the

buoyancy diffusivity via the turbulent Prandtl number $\mathrm{Pr}_T \equiv \langle K_u \rangle / \langle K_\theta \rangle$.

Substituting the linear PGF profile (3.9) into the RHS of the streamwise momentum equation in (3.5), and integrating in the vertical, one finds a parabolic profile for $\overline{u'w'}$. Assuming uniform shear in the interior (verified a posteriori with LES), this implies a quadratic eddy viscosity profile given by

$$K_u(z) = \frac{z(h-z)}{\tau_u}, \quad \tau_u \equiv \frac{Sh}{M}. \tag{3.10}$$

We highlight that the above solution does not satisfy the boundary conditions (3.7) as it assumes $S > 0$ everywhere. Hence, it should be regarded as an approximate solution away from the walls, although LES results respecting such free-slip boundary conditions reveal that S remains constant up to very close to the walls (see figure 3.8).

The solution (3.10) to the streamwise momentum balance may be vertically averaged and rearranged to solve for the shear magnitude, which we state in dimensional and dimensionless forms as

$$S = \frac{Mh}{6\langle K_u \rangle} \quad \Longleftrightarrow \quad \frac{hS^2}{M} = \alpha^2 \tag{3.11}$$

respectively, where $\tau_p \equiv \sqrt{h/M}$ and $\alpha \equiv \tau_u/\tau_p$. The dimensionless parameter α compares the eddy mixing and PGF timescales (τ_u and τ_p, respectively), such that small α values indicate fast eddy mixing compared to the forcing timescale, which decreases S (whereas weaker turbulence corresponds to larger α and S).

Similarly, given uniform stratification $N^2 \equiv g\theta_0^{-1}\mathrm{d}_z\overline{\theta}$ in the interior (also verified a posteriori with LES), the temperature equation in (3.5) with the linear environmental profile (3.6) can be integrated to find a quadratic eddy diffusivity for heat given by

$$K_\theta(z) = \frac{z(h-z)}{\tau_\theta}, \quad \tau_\theta \equiv 2\tau_h \left(1 - \frac{\Delta b_{env}}{hN^2}\right)^{-1}. \tag{3.12}$$

Again, we emphasize that (3.12) is an approximate solution valid away from the walls, since it does not satisfy the adiabatic boundary conditions (3.7) at $z = 0, h$.

Taking the vertical average of (3.12) and rearranging the terms to solve for the buoyancy

frequency leads to

$$N^2 = \frac{\Delta b_{env}}{h + 12\tau_h \langle K_\theta \rangle / h} \quad \Longleftrightarrow \quad \frac{hN^2}{\Delta b_{env}} = \frac{1}{1+2/\gamma}, \tag{3.13}$$

where $\gamma \equiv \tau_\theta / \tau_h$ is the dimensionless parameter comparing the rate of stratification to that of eddy mixing. Note that N^2 goes zero as $\gamma \to 0$ (i.e., stratification becomes weaker if eddy mixing dominates over the stratifying lateral heating), but $N^2 = \Delta b_{env}/h$ for $\gamma \to \infty$ (i.e., the environmental lapse rate is recovered in the absence of turbulent mixing).

In order to calculate K_u and K_θ using equations (3.10) and (3.12), one needs to estimate quantities such as M, τ_h and Δb_{env}. These variables may be well defined in the idealized problem presented in this section, but accurately estimating them based on limited field data or within more complete models can be a more challenging and subtle task. Fortunately, a simpler semi-empirical expression can be obtained for the eddy diffusivities by using LES data combined with scalings from the stratified turbulence literature and the analytical results from this section. Before deriving such an expression in section 3.5, however, we describe our LES experiments in section 3.4.

3.4 Large-eddy simulations

3.4.1 Numerical details and resolution requirements

Our LES code calculates vertical derivatives using a second-order centered finite-difference scheme in a staggered grid. Horizontal derivatives are computed with a pseudospectral scheme, and time is advanced via a second-order Adams-Bashforth scheme. We employ the scale-dependent Lagrangian dynamic Smagorinsky subgrid-scale (SGS) model described in Bou-Zeid et al. (2005).

The boundary conditions (3.7) are applied in the vertical direction. Such solid-wall conditions are necessary in the absence of rotation, since the stratified layers capping the SAL above and below it are in geostrophic balance. Hence, we do not include such stratified layers in our current simulation domain (which comprises only the SAL), as opposed to our previous simulations described in Rodakoviski et al. (2023), which incorporate the Coriolis effect. Albeit simpler in this sense, our current set-up is able to reproduce the neutral results obtained previously in that study (as

shown in section 3.5). Moreover, the lack of rotation eliminates the need of reconciling horizontal temperature gradients (associated with a vertically-varying PGF) with periodic boundary conditions (Momen et al., 2018).

The horizontal extent of our domain was set to $L_x = L_y = 4h$, and in the vertical we used $h = 1\,\mathrm{km}$. All runs used $N^3 = 320^3$ grid points, such that their spatial resolution is $\Delta x/4 = \Delta y/4 = \Delta z = 3.125\,\mathrm{m}$. The timestep was chosen to prevent numerical instabilities, and ranged from $\Delta t = 0.04$ to $0.36\,\mathrm{s}$.

Two important lengthscales that must be resolved are the Ozmidov and Corrsin lengthscales ($\ell_O \equiv \sqrt{\langle\varepsilon\rangle / N^3}$ and $\ell_C \equiv \sqrt{\langle\varepsilon\rangle / S^3}$, respectively), above which the effects of large-scale stratification and shear become important. Because our SGS scheme assumes a Kolmogorov cascade at (and below) the filter width $\Delta \equiv (\Delta x \Delta y \Delta z)^{1/3} \simeq 7.9\,\mathrm{m}$, it is important that $\Delta \lesssim \ell_O, \ell_C$. In fact, Khani (2018) has shown that LES can reproduce direct numerical simulations (DNS) results for stratified turbulence if the LES filter scale is small enough to resolve ℓ_O. As discussed in Appendix H, this criterion becomes exceptionally restrictive in the LAST regime.

3.4.2 Parameter space and LES runs

Next, we perform a dimensional analysis of the idealized problem described in section 3.3 in order to design our LES experiments efficiently. The independent variables defining our problem are h, τ_h, M, Δb_{env}. Only two independent dimensionless groups can be built from this list. Here, we define

$$\Pi_1 \equiv \frac{\Delta b_{env}}{M} = \left(\frac{\tau_p}{\tau_b}\right)^2, \qquad \Pi_2 \equiv \frac{\tau_h^2 \Delta b_{env}}{h} = \left(\frac{\tau_h}{\tau_b}\right)^2, \tag{3.14}$$

where $\tau_b \equiv \sqrt{h/\Delta b_{env}}$. All other dimensionless quantities in this problem are uniquely determined by the pair Π_1, Π_2. This includes, for instance, α, γ, Γ and $h^{-2} S^{-1} \langle K_\theta \rangle$.

We fixed $h = 1\,\mathrm{km}$ and $\Delta b_{env} \simeq 9.2 \times 10^{-2}\,\mathrm{m\,s^{-2}}$ (calculated with $\Delta\Theta = 3\,\mathrm{K}$ and $\theta_0 = 318\,\mathrm{K}$), and varied Π_1 and Π_2 by utilizing the values listed in table 3.1 for M and τ_h. Using dust concentration measurements from the SALTRACE campaign (Weinzierl et al., 2017), we estimate that $\tau_h \simeq 6\,\mathrm{days}$ for the SAL, which is within the range of simulated values in table 3.1 (calculation details are available in Appendix E). We named our LES runs PiHj, where i is a number from 1 to 4 labeling

Table 3.1: Forcing parameters defining each LES case, and symbols/colors used to represent their bulk statistics in subsequent figures. Each value of M is combined with each value of τ_h to produce 16 different flows.

Case	Defining parameter	Symbol/Color
P1Hj	$M = 0.1\,\mathrm{mm/s^2}$	■
P2Hj	$M = 0.4\,\mathrm{mm/s^2}$	▲
P3Hj	$M = 0.8\,\mathrm{mm/s^2}$	◆
P4Hj	$M = 2.0\,\mathrm{mm/s^2}$	●
PiH0	$\tau_h = \infty$	
PiH1	$\tau_h = 240\,\mathrm{h}$	
PiH2	$\tau_h = 24\,\mathrm{h}$	
PiH3	$\tau_h = 3\,\mathrm{h}$	

the value of M, and j is a number from 0 to 3 labeling the value of τ_h according to table 3.1. The combination of these parameters results in 16 independent LES runs, 4 of which (runs PiH0) are neutral reference cases with no lateral entrainment (i.e., $\tau_h = \infty$).

Flow statistics were computed after approximate stationarity was achieved, which took longer for runs with stronger stratification and weaker PGF (i.e., smaller τ_h and M). Time averages were calculated over several eddy turnovertimes (at least $22\tau_e$, more than $100\tau_e$ in some cases). However, our results show that the mixing timescales $\tau_u, \tau_\theta \gg \tau_e$ in large Ri_g runs. As a result, the averaging interval $T_{avg} < \tau_u, \tau_\theta$ for runs P1H2, P1H3, and P2H3. These are also the runs that took the longest to achieve equilibrium, and turbulence was actually slowly decaying during the interval used to calculate statistics. This is shown in figure 3.4 in terms of the TKE phase space introduced by Chamecki et al. (2018), which is based on the vertical average of the TKE balance (3.2) written as

$$\frac{\langle B \rangle}{\langle \varepsilon \rangle} = \left(\frac{\langle P \rangle}{\langle \varepsilon \rangle} - 1 \right) - \frac{\partial_t \langle k \rangle}{\langle \varepsilon \rangle}. \tag{3.15}$$

Most runs are close to the $\partial_t \langle k \rangle = 0$ isoline, but they tend to depart from it as M and τ_h decrease. Therefore, the slower mixing timescales associated with stronger stratification limit how strongly stratified our LES runs can be, as longer simulations are necessary not only to achieve a steady state, but also for statistics to converge.

Figures 3.5 and 3.6 show snapshots of temperature and vertical velocity on a xz-plane for different LES runs (see xy-plane snapshots in figure 3.7). Turbulent eddies span the entire vertical

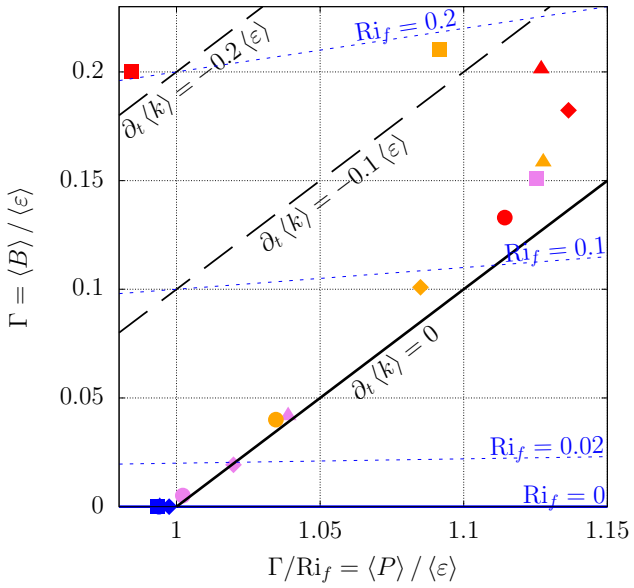

Figure 3.4: TKE phase space (based on Chamecki et al. (2018)) summarizing energy balance in all 16 LES runs. The blue, short-dashed lines correspond to constant flux Richardson number values (the solid line denoting the neutral case), whereas the black, long-dashed lines indicate the average decay rate of turbulence (the solid line denoting stationarity). Symbols and colors denote different PGF magnitudes and heating rates respectively, and are defined in table 3.1.

extent of the domain in the least stratified case (P4H1), whereas their size is severely reduced under stronger stratification (cf. case P1H3). P1H3 also has the smallest Corrsin and Ozmidov scales among all of our LES runs (namely, $\ell_C \simeq 6.3\,\mathrm{m}$, $\ell_O \simeq 22\,\mathrm{m}$). Even though our LES filter width resolves ℓ_O in this case, it barely resolves ℓ_C. More importantly, however, it can be seen in figure 3.6c that our grid size is not small enough to resolve the near-wall eddies in P1H3. Hence, spatial resolution requirements also limited how strongly stratified our numerical experiments could be. Regardless of these numerical limitations, however, the scale estimates from section 3.23.2.2 indicate that our weakly stratified runs are still useful models of the SAL.

Figure 3.8 shows some LES mean vertical profiles. When forced by a linear PGF profile and temperature nudging as described in section 3.33.3.1, the flow dynamics naturally produces uniform interior shear and stratification. Note that this is in contrast to other numerical studies which imposed uniform S and/or N by embedding them directly into the equations of motion (e.g., Shih et al., 2000; Laval et al., 2003). Very close to the walls, however, S and N drop to zero to satisfy the boundary conditions (3.7). In our LES runs, S ranges from 1.3×10^{-3} to $2.0 \times 10^{-2}\,\mathrm{s}^{-1}$, which includes the bulk value for the SAL of $S \simeq 5 \times 10^{-3}\,\mathrm{s}^{-1}$ estimated based on the discussion in section

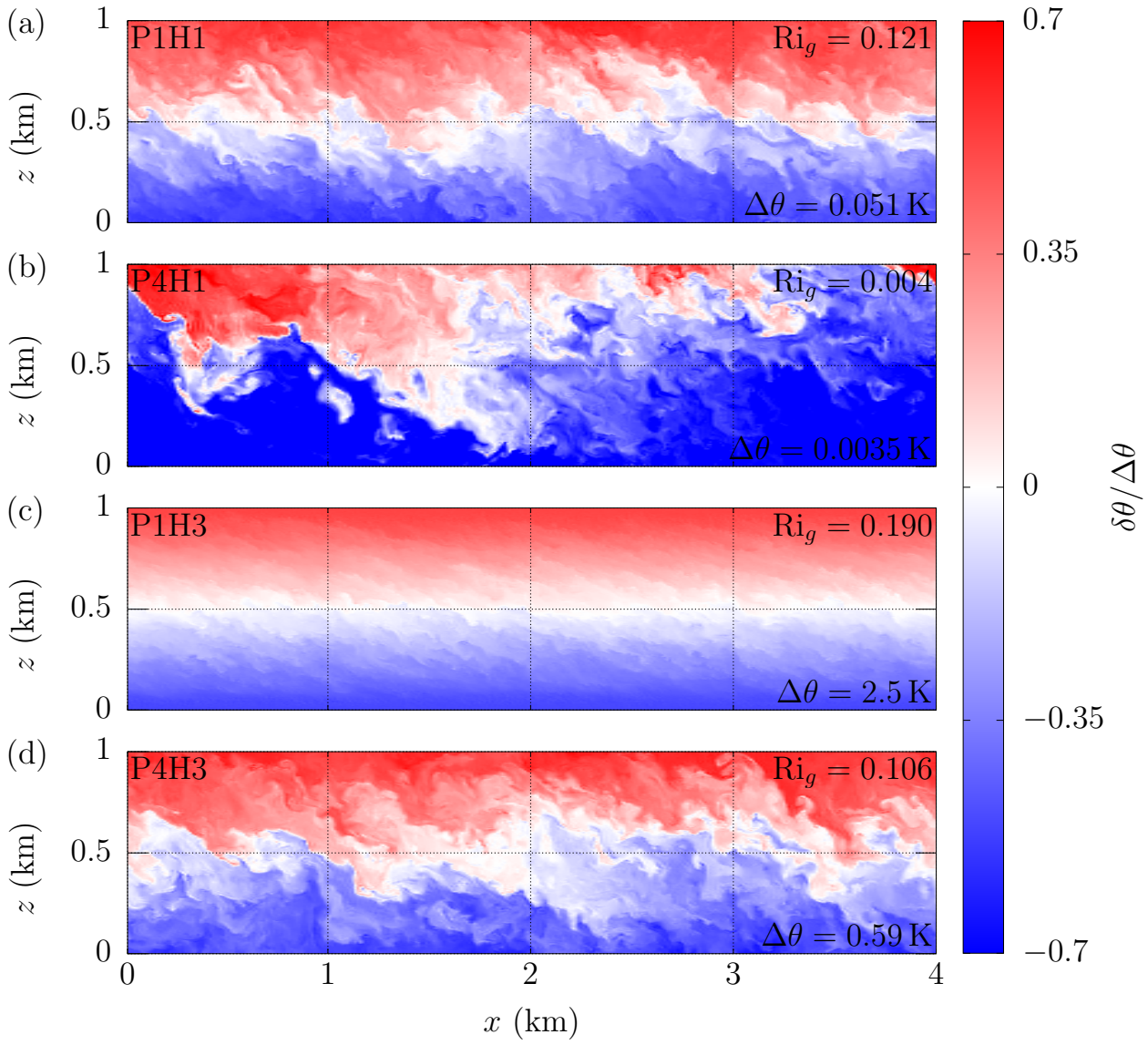

Figure 3.5: Vertical cross-section of LES instantaneous temperature (in terms of $\delta\theta \equiv \theta - \langle\overline{\theta}\rangle$ normalized by $\Delta\theta \equiv \overline{\theta}(h) - \overline{\theta}(0)$) in (a) a reference case, and the effect of increasing (b) PGF, (c) stratifying heating rate, or (d) both. Note the different colorbar ranges in each case.

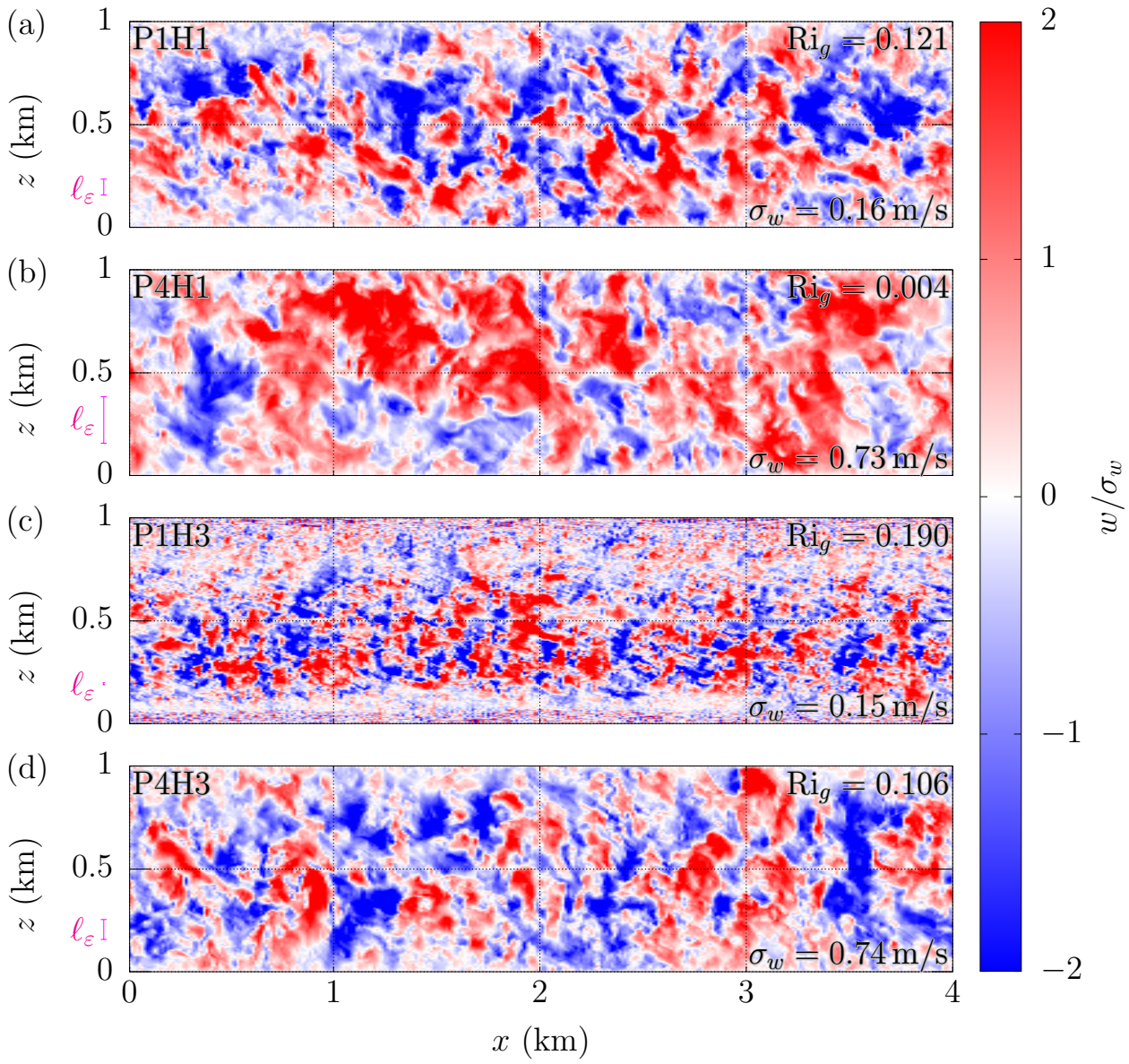

Figure 3.6: Same as figure 3.5 but for vertical velocity. Note that the RMS vertical velocity σ_w (defined in (3.18)) is determined by the PGF magnitude, whereas the correlation lengthscale (i.e., the eddy sizes) shrinks with increasing stratification. A visual representation of ℓ_ε is next to each plot for scale comparison.

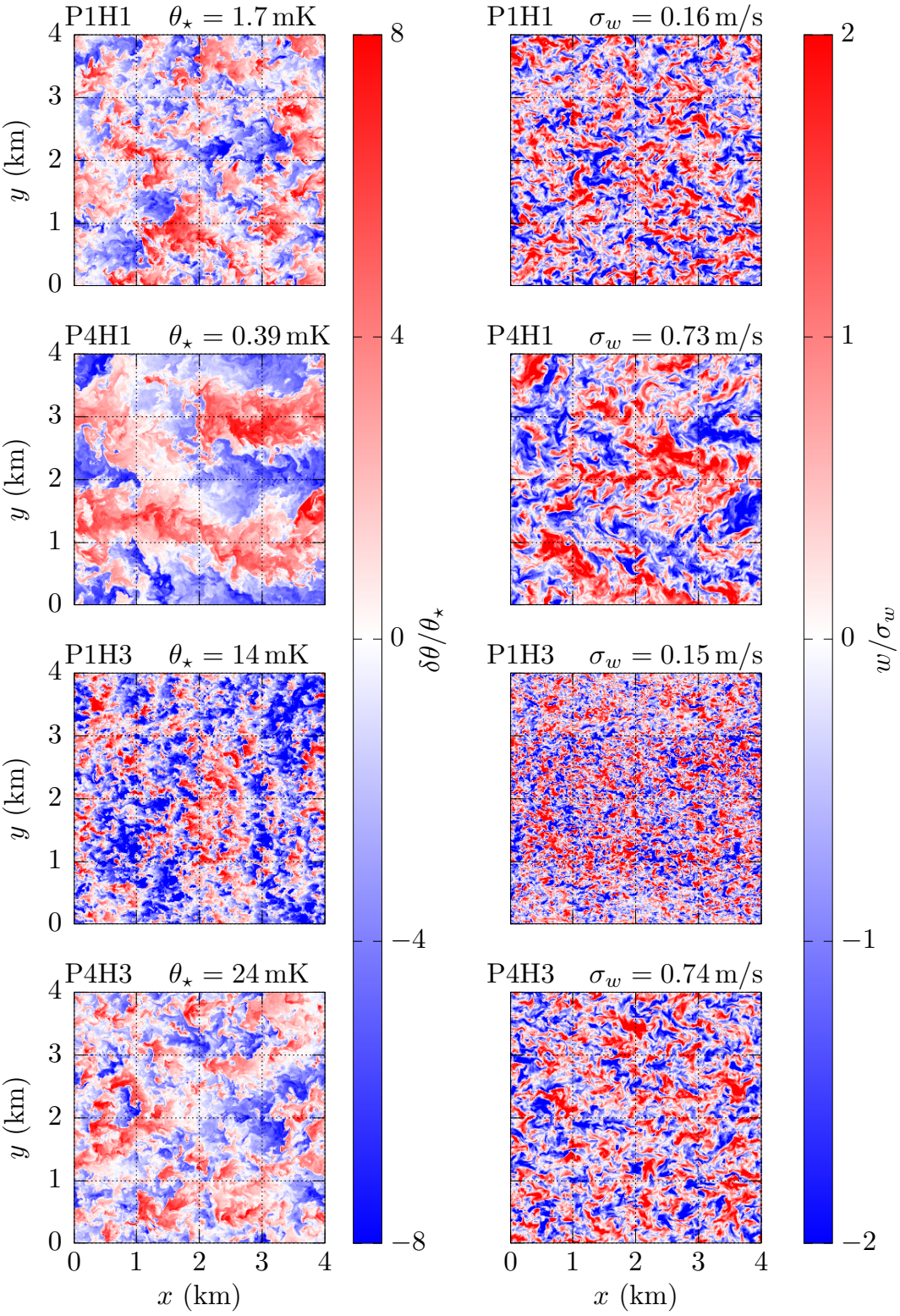

Figure 3.7: Horizontal cross-section of LES instantaneous temperature anomaly (left column) and vertical velocity (right column) at the midplane $z^* = 0.5$. Here, $\theta_\star \equiv -\left\langle \overline{w'\theta'} \right\rangle / \sigma_w$.

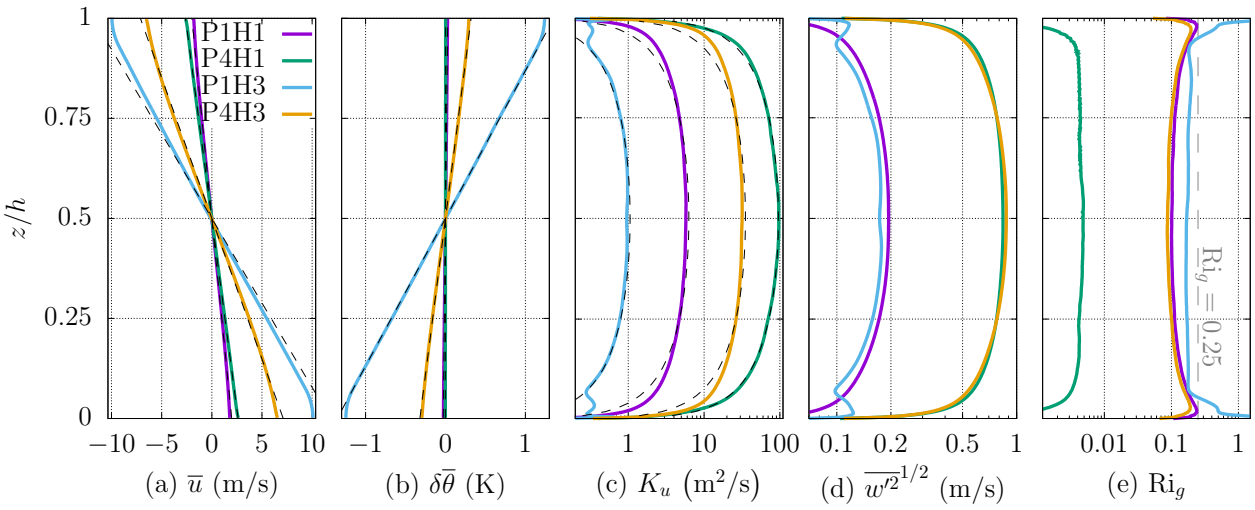

Figure 3.8: Mean flow statistics for selected LES experiments. LES profiles (solid lines) are compared to analytical solutions (black, dashed lines), which assume constant S, N and parabolic K profiles.

3.23.2.2. Similarly, N ranges from 0 to $8.8 \times 10^{-3}\,\mathrm{s}^{-1}$ in our simulations, which approximately coincides with its estimated range in the SAL.

Figures 3.8a–c show that the LES profiles match the analytical results from section 3.33.3.2. This can also be seen in figure 3.9, in which the mixing timescales τ_u, τ_θ were calculated by taking the vertical average of the quadratic diffusivity profiles (3.10) and (3.12) and rearranging as

$$\tau_u = \frac{h^2}{6\langle K_u \rangle}, \qquad \tau_\theta = \frac{h^2}{6\langle K_\theta \rangle}, \tag{3.16}$$

where eddy diffusivities were computed from LES results via their definition. Therefore, we confirm that, in our idealized scenario described in section 3.33.3.1, S and N are constant, and the profiles of K_u and K_θ can indeed be predicted by (3.10) and (3.12).

3.5 Results and discussion

3.5.1 A semi-empirical mixing-length model for the diffusivity

In what follows, we use LES results to derive simpler, alternative expressions to (3.10) and (3.12) for the momentum and heat diffusivities. For a stationary flow with uniform shear and stratification,

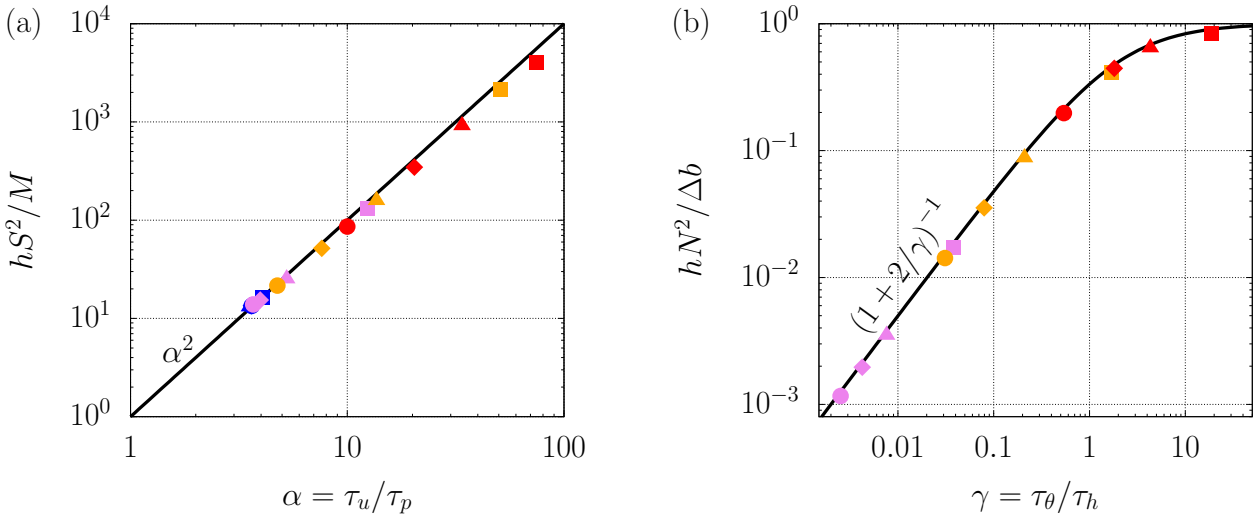

Figure 3.9: Normalized (a) shear and (b) stratification as a function of dimensionless ratios between mixing and forcing timescales from the analytical solutions (3.11) and (3.13) (solid lines), and LES (symbols as defined in table 3.1). Turbulent mixing dominates for small α, γ, while the mechanical and buoyancy forcings produce stronger shear and stratification as α and γ increase.

the vertically-averaged eddy diffusivities can be expressed in terms of the mixing coefficient defined in (3.3) as

$$\langle K_u \rangle = \frac{\langle P \rangle}{S^2} = \frac{(1+\Gamma)\langle \varepsilon \rangle}{S^2}, \quad \langle K_\theta \rangle = \frac{\langle B \rangle}{N^2} = \frac{\Gamma \langle \varepsilon \rangle}{N^2}. \tag{3.17}$$

Next, define a dissipation lengthscale and vertical velocity scale

$$\ell_\varepsilon \equiv \frac{\sigma_w^3}{\langle \varepsilon \rangle}, \quad \sigma_w \equiv \left\langle \overline{w'^2} \right\rangle^{1/2}. \tag{3.18}$$

The dissipation lengthscale is displayed to scale next to the snapshots in figure 3.6, and it is comparable to the typical eddy size. Rewritting the diffusivities in terms of these quantities,

$$\langle K_u \rangle = \frac{(1+\Gamma)\,\sigma_w^3}{\ell_\varepsilon S^2}, \quad \langle K_\theta \rangle = \frac{\Gamma \sigma_w^3}{\ell_\varepsilon N^2}. \tag{3.19}$$

Note that no additional assumptions were made to rewrite (3.17) as (3.19).

Figure 3.10a shows that most of our simulations follow the weak stratification scaling $\Gamma \sim \mathrm{Fr}_T^{-2}$ of Garanaik et al. (2019). Only our 3 most strongly stratified runs depart from that scaling, plateauing at $\Gamma \simeq 0.2$, i.e., the upper bound suggested by Osborn (1980). Our results also reproduce the scaling $\Gamma \sim \mathrm{Re}_b^{-1/2}$ (figure 3.10b), but better data collapse is observed with the Froude-number scaling.

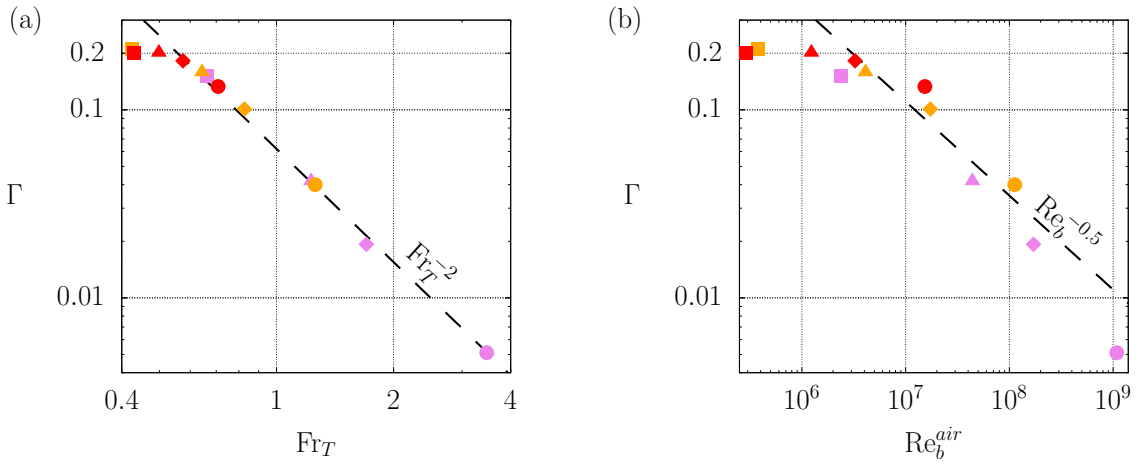

Figure 3.10: Mixing coefficients from LES (symbols defined in table 3.1) follow theoretical scalings for weakly stratified turbulence (dashed lines) and seem to plateau at 0.2. The Froude number (a) collapses our data better than the buoyancy Reynolds number (b).

Note that, because LES does not resolve the viscous dissipation scales, we used air viscosity to calculate Re_b^{air} via its definition in (3.1). The resulting values should be representative of the SAL provided that the SGS model accurately represents the energy cascade rate, as discussed by Chor et al. (2022).

The Froude number and the mixing coefficient can be written as

$$\mathrm{Fr}_T = \frac{\sigma_w^3}{\ell_\varepsilon \langle k \rangle N} = \frac{\beta \sigma_w}{\ell_\varepsilon N}, \quad \Rightarrow \quad \Gamma \sim \mathrm{Fr}_T^{-2} = \frac{\ell_\varepsilon^2 N^2}{\beta^2 \sigma_w^2}, \tag{3.20}$$

where we find the same value of $\beta \equiv \sigma_w^2 / \langle k \rangle \simeq 0.360$ for all LES runs (figure 3.11a). This is consistent with the scaling $\langle \varepsilon \rangle \sim \sigma_w^2 / \tau_e$ from Garanaik et al. (2019) for weak stratification, since $\langle \varepsilon \rangle = \langle k \rangle / \tau_e = \beta^{-1} \sigma_w^2 / \tau_e$. Moreover, note that, since $\ell_h \equiv \langle k \rangle^{3/2} / \langle \varepsilon \rangle$, it follows that $\ell_h = \beta^{-3/2} \ell_\varepsilon \simeq 4.63 \ell_\varepsilon$.

Combining (3.19) with (3.20), we find that the buoyancy diffusivity follows a mixing-length model

$$\langle K_\theta \rangle = \frac{\Gamma \sigma_w^3}{\ell_\varepsilon N^2} \sim \frac{\sigma_w \ell_\varepsilon}{\beta^2} \quad \Rightarrow \quad \langle K_\theta \rangle = C'_\theta \sigma_w \ell_\varepsilon. \tag{3.21}$$

A similar derivation for the eddy viscosity can be found in Appendix F. It also results in a mixing length model, i.e., $\langle K_u \rangle = C'_u \sigma_w \ell_\varepsilon$. From our LES data, $C'_u = 0.37 \pm 0.02$ and $C'_\theta = 0.45 \pm 0.02$ (figure 3.11b), implying constant $\mathrm{Pr}_T \simeq 0.84$ (which is also its average value across our LES runs).

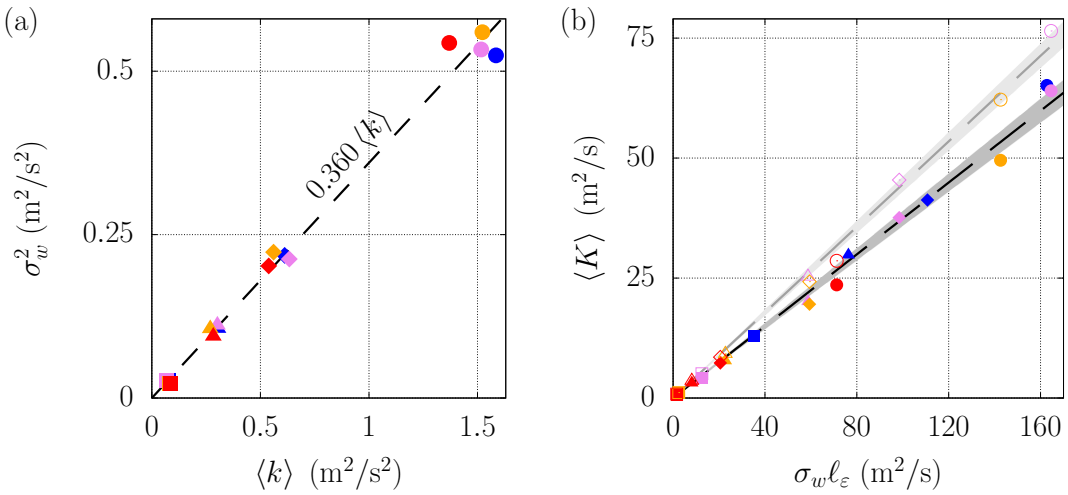

Figure 3.11: (a) Vertical velocity variance fractional contribution to TKE is approximately constant and equal to $\beta \simeq 0.360$. (b) Eddy diffusivity follows a mixing-length model under weak stratification, with best-fit slopes $C_u' \simeq 0.37 \pm 0.2$ and $C_\theta' \simeq 0.45 \pm 0.2$ at a 99% confidence level. Filled (empty) symbols and black (gray) lines denote the eddy diffusivity for momentum (buoyancy). The shaded regions indicate the uncertainty of the slopes.

$\mathrm{Pr}_T < 1$ has also been observed in previous simulations of stratified turbulence (e.g., Shih et al., 2005) and several studies investigating the stable atmospheric boundary layer (Li, 2019).

3.5.2 Richardson-number dependence

The next step is to estimate the velocity and length scales in the mixing-length model (3.21). It can be seen in figure 3.8d that the RMS vertical velocity profiles varies little with τ_h, depending mostly on M. In fact, the ultimate source of σ_w^2 is shear production, since the energy that it initially injects into u-variance is subsequently redistributed in all 3 directions by pressure. Assuming that shear production is approximately balanced by viscous dissipation (ignoring the smaller conversion rate into potential energy), one can write $\langle P \rangle \sim \sigma_w^3 / \ell_\varepsilon$. Using (3.11) to write $\langle P \rangle \sim M^2 h^2 / \langle K_u \rangle$ with $\langle K_u \rangle \sim \sigma_w \ell_\varepsilon$, we find $\sigma_w^2 \sim Mh$. This scaling is closely reproduced by our LES data (figure 3.12a). This is a more general result that also applies for ABL z-less states (i.e., very stable conditions away from the ground), with the friction velocity u_* replacing $\sqrt{Mh}$ (Nieuwstadt, 1984).

Whereas σ_w is not affected by stratification, ℓ_ε shrinks with increasing Ri_g, as revealed by the

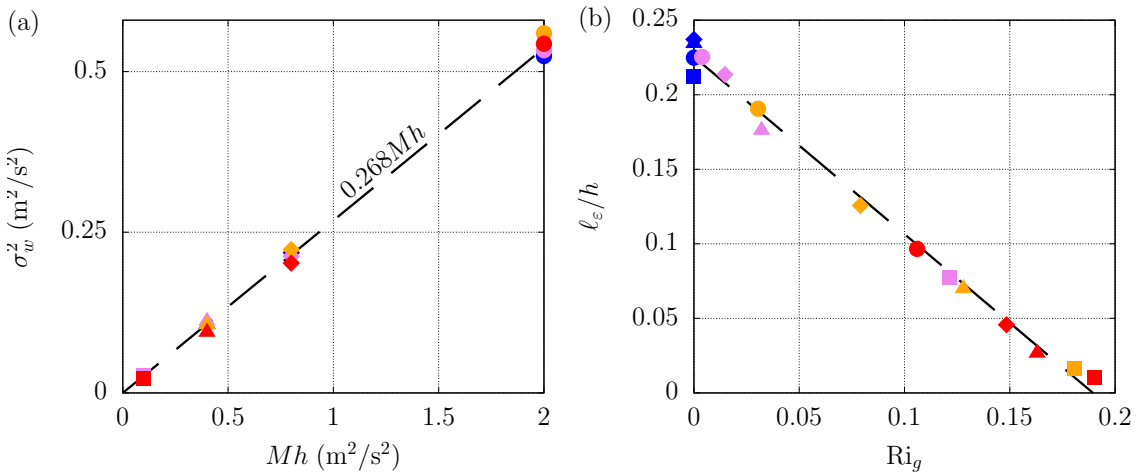

Figure 3.12: (a) Vertical velocity variance scales with Mh with a slope $\sigma_w^{*2} \simeq 0.268$ (calculated based on mixing-layer data). (b) Dimensionless dissipation lengthscale ℓ_ε/h decays linearly with Ri_g in our idealized SAL flow set-up. The Richardson number determines ℓ_ε/h when $\mathrm{Ri}_g > 0$, although M becomes relevant under neutral conditions where buoyancy control is absent.

linear fit derived from our LES data

$$\frac{\ell_\varepsilon}{h} \simeq m\,(r - \mathrm{Ri}_g)\,, \tag{3.22}$$

where $m \simeq 1.189$ and $r \simeq 0.190$. It can be seen in figure 3.12b that ℓ_ε varies a little with M under neutral conditions but not for $\mathrm{Ri}_g > 0$, when stratification effects dominate. Writing (3.21) in terms of $\sigma_w^* \equiv \sigma_w/\sqrt{Mh}$ and combining with (3.22), we find

$$\frac{\langle K_u \rangle}{\sqrt{Mh^3}} = C_u' \sigma_w^* m\,(r - \mathrm{Ri}_g)\,, \quad \frac{\langle K_\theta \rangle}{\sqrt{Mh^3}} = C_\theta' \sigma_w^* m\,(r - \mathrm{Ri}_g)\,. \tag{3.23}$$

Alternatively, we can use the analytical solution (3.11) to rewrite (3.23) in terms of S (instead of M, as shear data is more commonly available), resulting in

$$\frac{\langle K_u \rangle}{h^2 S} = C_u\,(r - \mathrm{Ri}_g)^2\,, \quad \frac{\langle K_\theta \rangle}{h^2 S} = C_\theta\,(r - \mathrm{Ri}_g)^2\,, \tag{3.24}$$

where $C_u = 6C_u'^2 \sigma_w^{*2} m^2 = \mathrm{Pr}_T C_\theta$. In order to determine the value of these empirical coefficients, we note that, under neutral conditions, (3.24) implies $\langle K_u \rangle = C_u r^2 h^2 S$. Similar scalings have also been obtained from experimental mixing layer data. For instance, figure 40 in Wygnanski et al. (1970) shows that $K_u \simeq 0.002xV$, where V is the imposed free-stream velocity difference and x is the distance downstream. Using the fully developed mixing-layer thickness $\delta \simeq 0.174x$ (Brown

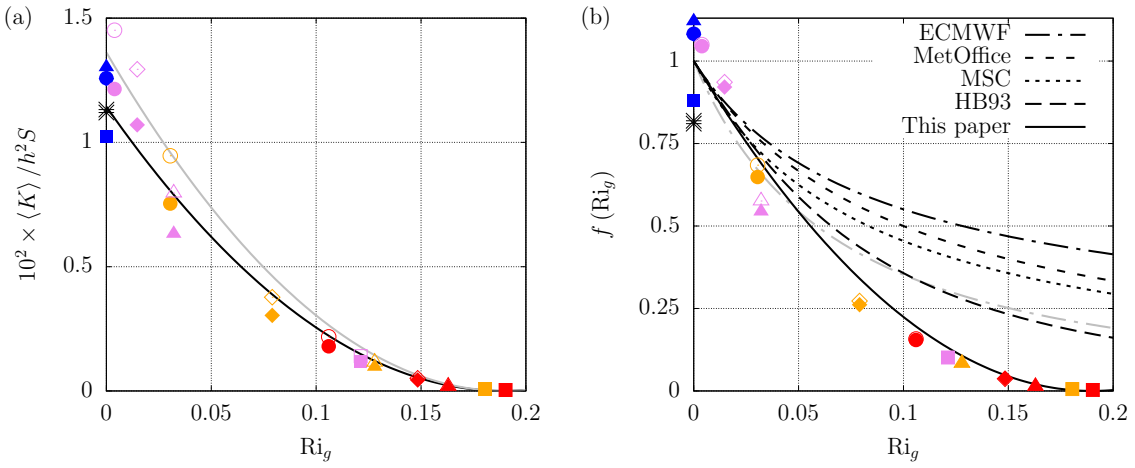

Figure 3.13: (a) Diffusivity normalized by h^2S decays with the square of Ri_g under weak stratification (defined here as $\mathrm{Ri}_g \lesssim r$). The eddy diffusivities for momentum (buoyancy) are denoted by filled (empty) symbols and black (gray) lines. Black asterisks denote the bin-averaged dust diffusivities for the two LES runs from Rodakoviski et al. (2023), which utilized a baroclinic (but neutral) SAL idealization bounded by stratified fluid layers (rather than solid walls, as in the present study). (b) Stability functions defined according to (3.25) employed by the schemes used by the ECMWF (European Centre for Medium-Range Weather Forecasts), MetOffice (Met Office, UK), and MSC (Meterological Service of Canada), as described in Cuxart et al. (2006), as well as the ones utilized in Bretherton et al. (2009, referred to as HB93) and this paper.

et al., 1974), we get $K_u \simeq 0.0115\delta V$, where the velocity and length scales V and δ replace their SAL counterparts hS and h, respectively. Therefore, by setting $C_u r^2 = 0.0115$, we find $C_u \simeq 0.319$. This implies $\sigma_w^* \simeq 0.518$, which matches our LES data (figure 3.12a).

Note that one can combine (3.11), (3.21), and (3.22) to find $K \sim \ell_\varepsilon^2 S$. Hence, the neutral relationship $K \sim h^2 S$ breaks down for $\mathrm{Ri}_g > 0$ because stratification causes ℓ_ε to decrease.

Figure 3.13a shows good agreement between our LES data and (3.24). Note that these semi-empirical expressions were derived based on the assumption of weak stratification. Hence, they should be regarded as useful approximations to the complete solution valid for small $\mathrm{Ri}_g \lesssim r$. For stronger stratification regimes, (3.20)–(3.24) break down. Although $\langle K \rangle$ may become really small at large Ri_g values (e.g., Peters et al., 1988), it does not vanish at $\mathrm{Ri}_g = r$ since ℓ_ε does not really go to zero at that value (as implied by the dashed line in figure 3.12b). We do not have enough strongly stratified runs in order to find a better approximation for ℓ_ε / h at larger Ri_g values. However, we note that the model described in Bretherton et al. (2009) also predicts no turbulence above $\mathrm{Ri}_g = 0.19$.

Most free-tropospheric turbulence parameterizations are simple extensions of ABL parameteri-

zations (e.g. Holtslag et al., 1993; Bretherton et al., 2009). Many of the latter can be written in terms of mixing lengths λ (typically ranging from 40 to 200 m) and stability functions $f(\mathrm{Ri}_g)$ (Cuxart et al., 2006). Our model (3.24) can be put in this format as follows:

$$\langle K_u \rangle = \lambda_u^2 S f(\mathrm{Ri}_g), \quad \lambda_u = C_u^{1/2} r h \simeq 107\,\mathrm{m}, \quad f(\mathrm{Ri}_g) = \left(1 - \frac{\mathrm{Ri}_g}{r}\right)^2, \tag{3.25}$$

with an equivalent definition for $\langle K_\theta \rangle$ using $\lambda_\theta = \lambda_u \mathrm{Pr}_T^{-1/2}$. The stability functions used by different models are depicted in figure 3.13b in comparison with the function defined in (3.25) and our LES data. It is clear that our model, which was developed for an elevated layer forced similarly to the SAL, predicts a much faster decay in $\langle K \rangle$ as Ri_g grows than typical ABL parameterizations. We attribute this difference to the fact that, in the ABL, the ground imposes a no-slip boundary condition at all times. This different set-up presumably affects how fast diffusivities decay with increasing Ri_g. From a mixing-length modeling perspective, this decay is contained in the lengthscale ℓ_ε, given that the velocity scale (u_* in the ABL, $\sqrt{Mh}$ in the SAL) is independent of static stability.

We remark that the only assumptions necessary to obtain equations (3.23)–(3.25) from (3.19) are weak stratification (thus $\Gamma \sim \mathrm{Fr}_T^{-2}$ and $\beta = \text{constant}$), $\sigma_w^2 \sim Mh$ (regardless of stratification), the empirical linear decay of ℓ_ε with Ri_g following (3.22), and the analytical solution (3.11) (which assumes constant S).

3.5.3 Implications for Saharan dust

The average residence time of dust particles in a non-turbulent SAL is $h/2w_s$, where $w_s(D_p)$ is the settling velocity of a particle of diameter D_p (Rodakoviski et al., 2023, eqns. (17)–(18)). The relative increase in their airborne lifetime due to turbulent mixing is

$$\Delta\tau_R^* = \frac{1}{\mathrm{Pe}} - \frac{1 - e^{-\mathrm{Pe}}}{\mathrm{Pe}^2}, \quad \mathrm{Pe} = \frac{w_s h}{\langle K_c \rangle}, \tag{3.26}$$

where K_c is the dust eddy diffusivity. Assuming $K_c = K_\theta$, we can combine (3.24) and (3.26) to estimate the impact of weakly stratified turbulent mixing on dust deposition rates. In the example shown in figure 3.14a, the deposition of coarse and super-coarse dust ($D_p > 5$ and $10\,\mu$m, respectively) is considerably delayed (even by a factor of 2) for a range of values of $\mathrm{Ri}_g > 0$.

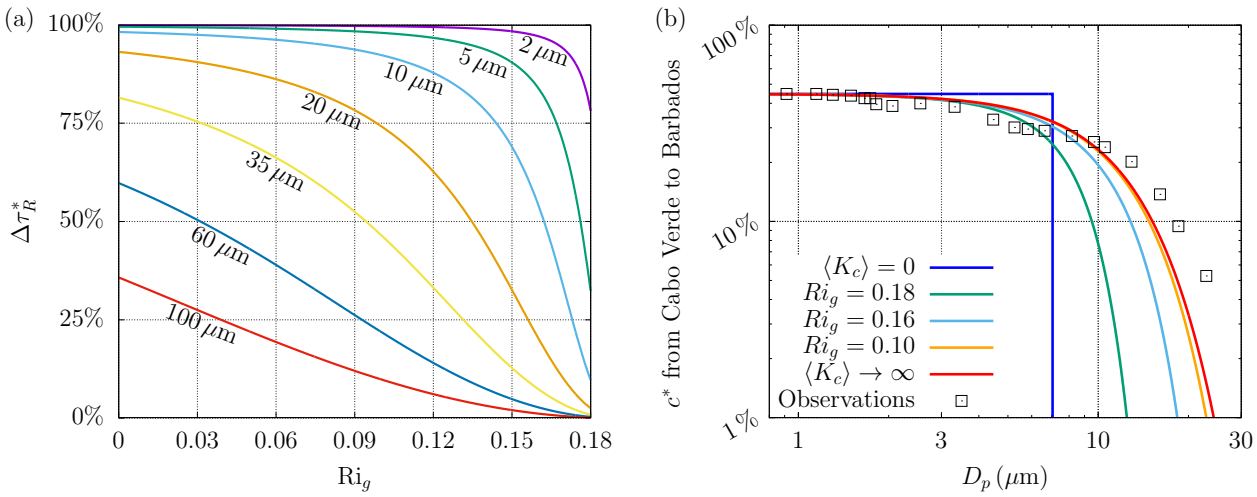

Figure 3.14: (a) Relative increase in average residence time of SAL dust (equation (3.26)) due to vertical turbulent mixing with respect to laminar case as a function of particle size and Ri_g. Calculations assume $h = 2\,\mathrm{km}$, $S = 4\times10^{-3}\,\mathrm{s}^{-1}$, $g = 9.8\,\mathrm{m\,s}^{-2}$, air density $\rho_f = 1.0\,\mathrm{kg\,m}^{-3}$ and viscosity $\mu_f = 1.7\times10^{-5}\,\mathrm{Pa\,s}$, dust density $\rho_p = 2650\,\mathrm{kg\,m}^{-3}$ and shape factor $\chi = 1.4$ (Rodakoviski et al., 2023, eqns. (17)–(18)). (b) Fraction of concentration of different size dust remaining airborne from Cabo Verde to Barbados assuming different stratification conditions and $h = 4\,\mathrm{km}$ (colored curves) and calculated based on field data from the SALTRACE campaign (symbols, Weinzierl et al., 2017). Cases $\mathrm{Ri}_g = 0.10$ and $\mathrm{Ri}_g = 0.18$ have associated $\langle K_c\rangle \simeq 200\,\mathrm{m}^2\,\mathrm{s}^{-1}$ and $2\,\mathrm{m}^2\,\mathrm{s}^{-1}$, respectively, which shows that even weak turbulent mixing makes a significant difference in the airborne lifetime of coarse particles.

Size-resolved dust concentration measurements were taken during the SALTRACE campaign before and after a SAL air mass traveled across the North Atlantic over about 5 days (Weinzierl et al., 2017, fig. 9). In figure 3.14b, we used that data to compare the concentration fraction c^* of dust remaining airborne after the transatlantic trip to estimates for different stratification scenarios obtained by combining (3.24) and Rodakoviski et al. (2023, eqn. (11)). It takes $\mathrm{Ri}_g \gtrsim 0.10$ for the analytical prediction for $c^*(D_p)$ to depart from the instant mixing limit ($\mathrm{Pe} \to 0$ as $\langle K_c \rangle \to \infty$). This suggests that, even under weak stratification, turbulence may be strong enough to vertically mix even super-coarse dust concentration profiles almost perfectly. Furthermore, including at relatively large $\mathrm{Ri}_g \simeq 0.18$, when $\langle K_c \rangle = O(1)\ \mathrm{m^2\,s^{-1}}$, coarse particles are significantly impacted by turbulence. Therefore, despite the substantial decrease in eddy diffusivity magnitudes caused by stable buoyancy stratification, vertical eddy mixing still has a very pronounced impact on dust deposition rates under weakly stratified conditions. Hence, even in a stratified SAL, turbulence can explain observations of coarse Saharan dust in the Americas to a substantial degree. As mentioned in section 3.1, other processes such as deep convective uplift events are likely important contributors as well (Van Der Does et al., 2018).

3.6 Concluding remarks

As indicated by the scale estimates from section 3.2.2, shear turbulence in the SAL may be anywhere from nearly neutral to strongly stratified. For a given SAL event, its exact nature must be a result of the forcing conditions. These include the SAL depth, the exact initial conditions as it leaves the African continent (e.g., perfectly well-mixed or containing a residual stratification), the thermodynamical structure $\Theta_{env}(z)$ of the surrounding air, as well as the horizontal PGF profile $-\nabla_h \overline{\phi}(z)$ and the lateral entrainment rate τ_h^{-1} resulting from synoptic-scale dynamics. A more realistic study would not only allow for these forcing conditions to vary over time, but also include other processes such as cloud dynamics, vertical entrainment at the SAL top and bottom, as well as the internal heating profile $\dot{q}(z)$ resulting from radiative interactions involving dust and water vapor.

Although stable stratification considerably reduces eddy diffusivity values (figure 3.13), our results in figure 3.14 show that vertical mixing due to stratified shear turbulence can significantly

increase the airborne mass and lifetime of even coarse dust in the SAL (for the levels of stratification tested here). Note that the instant mixing (red) curve in figure 3.14b is an upper limit (defined by $\mathrm{Pe} \to 0$ as $\langle K_c \rangle \to \infty$) to the effect of eddy mixing on settling dust concentrations (Rodakoviski et al., 2023), which in that case is approached by $\langle K_c \rangle = 200\,\mathrm{m^2\,s^{-1}}$ (under weak stratification). However, measured concentrations were above this conceptual limit, indicating that other processes might also be important to keep coarse dust aloft for longer times. For instance, strong updrafts in thunderstorms and tropical cyclones might be relevant contributors, as they can lift coarse particles to great heights in scattered events (Van Der Does et al., 2018).

Finally, we highlight that even the small diffusivity values found at large Ri_g could produce plenty of mixing in the long timescales for horizontal transport in the upper atmosphere. Figure 3.14b shows one situation where this becomes relevant, but this is expected to be more generally true (not only for dust in the SAL). Small K values could also significantly impact atmospheric chemistry, given that reaction rates can be limited by inhomogeneities in reactant concentrations (Donaldson et al., 1972). This also means that determining the correct form of the decay of K as Ri_g increases is critical. Figure 3.13b suggests that K decays faster with Ri_g in the upper atmosphere than in the ABL, putting into question the use of the latter in the free-troposphere, where a no-slip boundary promoting the development of shear instabilities and turbulence is absent.

CHAPTER 4

Conclusions

4.1 Summary

In this dissertation, we used LES and an analytical approach to describe the turbulent mixing of settling dust in two different idealized SAL set-ups. We found that the relative increase in dust airborne lifetime caused by turbulence is given by

$$\Delta\tau_R^* = \frac{1}{\mathrm{Pe}} - \frac{1-e^{-\mathrm{Pe}}}{\mathrm{Pe}^2}, \quad \mathrm{Pe} = \frac{w_s h}{\langle K_c \rangle}. \tag{4.1}$$

Hence, the increase due to turbulence in the airborne lifetime of dust in the SAL depends only on the Peclet number, and it is limited to a factor of 2 at most. Moreover, we found that models do approach SALTRACE observations when turbulent mixing is taken into account. This is ilustrated in figures 2.11b and 3.14b. Therefore, particle asphericity and turbulent mixing greatly help explain the presence of coarse Saharan dust in the Americas.

Observations show that the SAL is nearly well-mixed, but typically presents some degree of stratification. Hence, SAL turbulence must be generally stratified and produced by shear (mainly due to the AEJ). Based on this idea, we have also developed a theoretical framework that allowed us to find an algebraic expression for the dust eddy diffusivity in the SAL as a function of the gradient Richardson number, namely,

$$\langle K_c \rangle = C_\theta h^2 S \left(r - \mathrm{Ri}_g\right)^2, \tag{4.2}$$

where $C_\theta \simeq 0.38$ and $r \simeq 0.19$. This is a faster decay with increasing Ri_g than seen in typical ABL models, which is thought to be mainly a consequence of the absence of a solid wall in the SAL.

Even though buoyancy stratification causes eddy mixing to be greatly reduced, we also learned that even small diffusivity values can play an important role in processes that are slow enough,

which includes the transport of dust in the SAL, as depicted in figure 3.14. Therefore, even under strong stratification, intermittent mixing events should contribute a reasonable amount to reducing dust deposition rates (at least for particles caught in such events). However, other processes (such as deep convection events), may indeed be relevant and necessary to fully explain the observed long-range transport of coarse Saharan dust.

4.2 Future work

There are several aspects of this problem that require further investigation. For instance, the effect of strong updrafts in deep convection events on the airborne dust mass could be investigated by means of numerical simulations (e.g., Lagrangian point particles in an LES). This involves the coupling between the MBL and the SAL, which also occurs via entrainment fluxes through the SAL bottom inversion. As mentioned in chapter 2, downward eddy fluxes of dust towards the MBL are known to be an effective dust removal mechanism from the SAL (Carlson et al., 1972; Jähn et al., 2016; Weinzierl et al., 2017), but they have been neglected in the studies that compose this dissertation. The role of MBL and SAL turbulence in maintaining the inversion layer that separates them is also of interest, since different configurations involving these layers have been observed (Rittmeister et al., 2017). The effects of aerosol cloud processing and wet deposition, which become increasingly important as the SAL approaches the Caribbean (Ridley et al., 2012), have not been addressed in this dissertation either.

Furthermore, a more comprehensive, realistic approach could also be potentially very informative. For instance, we could allow the forcing conditions to evolve in time so as to simulate a semi-Lagrangian LES box that moves with the SAL mean zonal speed. Nudging the wind speed and potential temperature profiles to observations at several locations over the tropical North Atlantic could provide us with a better understanding regarding the turbulence characteristics in the SAL, as well as its potential impacts on dust deposition rates. Field campaigns designed to measure turbulent quantities (e.g., vertical profiles of Reynolds stresses and eddy heat fluxes) following a Lagrangian SAL plume would be ideal to validate the ideas presented in this dissertation. Finally, one end goal would be to implement vertical eddy mixing schemes such as (4.1)–(4.2) in climate models in

order to verify whether they bring simulations of the dust system on Earth closer to observations, therefore solving (at least partly) the coarse-dust long-range transport conundrum.

APPENDIX A

Asymptotic solution for large Peclet numbers

At large Pe values, the series solution (2.12) converges slowly. A useful alternative expression (Brenner, 1962) for the mass decay is then given by

$$m^*(t^*,\mathrm{Pe}) \sim M_1(t^*,\mathrm{Pe}) + M_2(t^*,\mathrm{Pe}) - M_3(t^*,\mathrm{Pe}) \quad \text{as} \quad \mathrm{Pe} \to \infty, \tag{A.1}$$

where

$$M_1 = (1-t^*)\left\{1 - \frac{1}{2}\mathrm{erfc}\left[\sqrt{\frac{\mathrm{Pe}}{4t^*}}(1-t^*)\right]\right\} + \frac{\mathrm{e}^{\mathrm{Pe}}}{2}(1+t^*)\,\mathrm{erfc}\left[\sqrt{\frac{\mathrm{Pe}}{4t^*}}(1+t^*)\right], \tag{A.2}$$

$$\begin{aligned} M_2 = \frac{1}{3}\sqrt{\frac{\mathrm{Pe}t^*}{\pi}}\left[2t^* + 3(1+t^*) + \frac{\mathrm{Pe}}{2}(1+t^*)^2\right] \times \\ \times \left\{\exp\left[-\frac{\mathrm{Pe}(1-t^*)^2}{4t^*}\right] - \exp\left[-\frac{\mathrm{Pe}\left(4+t^{*2}\right)}{4t^*}\right]\right\}, \end{aligned} \tag{A.3}$$

$$\begin{aligned} M_3 = \mathrm{e}^{\mathrm{Pe}}\left[t^* + \frac{\mathrm{Pe}}{2}t^*(1+t^*) + \frac{\mathrm{Pe}}{2}(1+t^*)^2 + \frac{\mathrm{Pe}^2}{12}(1+t^*)^3\right] \times \\ \times \left\{\mathrm{erfc}\left[\sqrt{\frac{\mathrm{Pe}}{4t^*}}(1+t^*)\right] - \mathrm{erfc}\left[\sqrt{\frac{\mathrm{Pe}}{4t^*}}(2+t^*)\right]\right\}. \end{aligned} \tag{A.4}$$

APPENDIX B

Significance of particle inertia

From table 2.2, our largest particle has response time $\tau_p = w_s/g = 0.0204\,\mathrm{s}$ and diameter $D_p = 61.0\,\mu\mathrm{m}$. In BASE, where turbulence is stronger, the TKE dissipation rate measured from the LES output peaks near the domain center at a value of $\varepsilon = 1.96 \times 10^{-4}\,\mathrm{m^2\,s^{-3}}$. The corresponding Kolmogorov length and time scales in the atmosphere (assuming air with kinematic viscosity $\nu = \mu_f/\rho_f = 1.7 \times 10^{-5}\,\mathrm{m^2\,s^{-1}}$) are hence $\eta_K = \left(\nu^3/\varepsilon\right)^{1/4} = 2.24\,\mathrm{mm}$ and $\tau_K = \sqrt{\nu/\varepsilon} = 0.295\,\mathrm{s}$. Therefore, our greatest Stokes number is $\mathrm{St} = \tau_p/\tau_K = 0.069$, which is significantly smaller than the value of $\mathrm{St} = 0.2$ suggested by Balachandar et al. (2010) as the maximum Stokes number for which the dusty gas approach is still a reasonable approximation.

Furthermore, assuming that the LES filter scale, given by $\Delta = (\Delta x \Delta y \Delta z)^{1/3} = 9.92\,\mathrm{m}$, occurs in the inertial subrange where Kolmogorov scaling is valid, the timescale of the smallest resolved eddy in BASE is estimated as $\tau_\Delta = \tau_K\,(\Delta/\eta_K)^{2/3} = 79.5\,\mathrm{s}$. Hence, $\tau_p/\tau_\Delta \lesssim 3 \times 10^{-4}$ in our simulations, which is less than the maximum acceptable value of 10^{-3} for that ratio provided by Balachandar et al. (2010, fig. 2) for LES using the dusty gas approach. Moreover, $D_p/\eta_K \lesssim 3 \times 10^{-2}$ in our simulations, i.e., all simulated particles are much smaller than the Kolmogorov lengthscale (and thus also much smaller than the smallest resolved eddies in the LES), so the point-particle approximation, implicit in the dusty gas approach, is also valid.

In conclusion, particle inertia effects can be safely neglected in this study, since the response time of the heaviest simulated particles is still much smaller than the timescale of the fastest, smallest resolved eddies. Therefore, (2.3) is a good model for the problem at hand.

APPENDIX C

Calculation of $c^*(D_p)$ with SALTRACE data and theory

If we denote the airborne dust mass in the Cabo Verde and Barbados regions as m_0 and m_f respectively, we can write

$$m^* = \frac{m_f}{m_0} = \frac{c_f \, \delta V_f}{c_0 \, \delta V_0}, \tag{C.1}$$

where c and δV respectively refer to the mass concentration and the volume of a Lagrangian fluid element at each location. Defining a plume spread coefficient as $\alpha_v = \delta V_0 / \delta V_f$ (where $\alpha_v < 1$ due to entrainment of non-SAL air into the plume), we can relate the mass ratio to the concentration ratio $c^* = c_f / c_0$ at the two locations via

$$c^* = \alpha_v m^*. \tag{C.2}$$

In order to relate mass concentration c to number concentration n, we write

$$c(D_p) = n(D_p) \times \underbrace{\rho_p(D_p)}_{\text{particle density}} \times \underbrace{\left(\frac{1}{6}\pi D_p^3\right)}_{\text{particle volume}}, \tag{C.3}$$

where, by definition, the volume-equivalent diameter D_p is used to calculate the volume for any particle shape. With the assumption that $\rho_p(D_p)$ remains unchanged from Cabo Verde to Barbados, we have that

$$c^*(D_p) = \frac{n_f(D_p)}{n_0(D_p)}. \tag{C.4}$$

The number size distributions n_0 and n_f were obtained from SALTRACE measurements (Weinzierl et al., 2017, fig. 9) in order to generate figure 2.11b.

We further assume that dry deposition is negligible for the smallest particle size available in the data. This is confirmed by figure 2.12, which shows that particles with $D_p < 2\,\mu$m have negligible settling after around 5 days of transport. However, we also need to consider the possibility that, even for those small particles, $m^* = \alpha_0 < 1$ due to processes other than entrainment of non-SAL air into the plume (e.g., wet deposition). Under the assumption that these processes affect all particle sizes equally, we accounted for their effect by calculating the concentration fraction as $c^* = \alpha m^*$, where α is an overall dilution factor estimated as

$$\alpha = \alpha_0 \alpha_v = \left.\frac{n_f}{n_0}\right|_{\text{smallest } D_p} \approx 0.447. \tag{C.5}$$

If concentration measurements are taken at a height z_m from the SAL base at an instant t_m, assuming a well-mixed initial profile, theory for the laminar case predicts that

$$c^*(D_p) = \begin{cases} \alpha, & D_p \leq D_{p,max}, \\ 0, & D_p > D_{p,max}, \end{cases} \tag{C.6}$$

where the maximum diameter is given implicitly by

$$w_s(D_{p,max}) = \frac{h - z_m}{t_m}. \tag{C.7}$$

As described in Weinzierl et al. (2017), for a travel time of $t_m = 5\,$days, the greatest particle size to be detected at a distance $h - z_m = 1.3\,$km from the SAL top is that with settling velocity $w_s = 0.26\,\text{km}\,\text{day}^{-1}$ which, according to equations (2.17)–(2.18) and the values given in table 2.2, corresponds to $D_{p,max} = 7.05\,\mu$m. The well-mixed limit, on the other hand, predicts that

$$c^*(D_p) = \alpha \exp\left[-\frac{w_s(D_p)\,t_m}{h}\right]. \tag{C.8}$$

Equations (C.6)–(C.8) were used to plot the theoretical curves in figure 2.11b.

APPENDIX D

Ensemble averages

Here we describe the calculations behind figure 2 in the main text in greater detail. Temperature observations are from radiosondes launched by the German Weather Service aboard the research vessel *Meteor* during the M96 cruise in May 2013 in the context of the Saharan Aerosol Long-range Transport and Aerosol-Cloud-interaction Experiment (SALTRACE), as described in Rittmeister et al. (2017). Wind data were obtained from dropsondes released from the BAe146 research aircraft operated by the UK Facility for Atmospheric Airborne Measurements in August 2015 in the context of the AERosol Properties-Dust (AER-D) field campaign, as described in Ryder et al. (2018).

For the SALTRACE dataset, we inferred the SAL location from soundings profiles (such as N and moisture content) as well as backward trajectories from NOAA's HYSPLIT model. For the AER-D dataset, we used aerosol profiles from Ryder et al. (2018) to help define SAL limits.

Let each realization (measured profile) be denoted with an index i. The vertical coordinate was normalized such that $z_i^* = (z - z_{0,i})/h_i$, where $z_{0,i}$ is the SAL base height above MSL and h_i is its depth. Thick lines correspond to the ensemble averages $[(\theta_i - \theta_{i,0})/\Delta\theta_i]$ and $[u_i - \langle u_i \rangle]$, where $\theta_{0,i} = \theta(z_i^* = 0)$, $\Delta\theta_i = \theta(z_i^* = 1) - \theta_{0,i}$, and $\langle u_i \rangle$ is the vertical average of u_i. The normalized vertical coordinated is defined for the ensemble averages such that

$$[f_i](z^*) = \frac{1}{N}\sum_{i=1}^{N} f_i(z_i^* = z^*), \tag{D.1}$$

where f_i is an observed profile. The environmental profile is taken as the standard tropical atmosphere Θ_{env} from Anderson et al. (1986), and normalized using its values at $[z_0] \simeq 1.4\,\text{km}$ and $[z_0 + h]$, where $[h] \simeq 2.6\,\text{km}$. The temperature and wind profiles are from the SALTRACE and AER-D datasets, respectively. In the SALTRACE dataset, $[\Delta\theta] \simeq 9.7\,\text{K}$.

APPENDIX E

Estimating τ_h from SALTRACE data

Integrating the concentration equation from Rodakoviski et al. (2023, eqn. (4)) over a horizontal area A and in the vertical, we find that the dust mass within the SAL changes over time as

$$\frac{\mathrm{d}m}{\mathrm{d}t} = -w_s A c_b - \frac{m}{\tau_h}, \tag{E.1}$$

where $c_b = c\,(z=0)$. Note that we added a nudging term for lateral entrainment of dust-free environmental air (with $c=0$) with same timescale as for the buoyancy equation. This will act to dilute dust concentrations. Normalizing by $m\,(t=0) = m_0$ and $\tau_g = h/w_s$,

$$\frac{\mathrm{d}m^*}{\mathrm{d}t} = -\frac{1}{\tau_g}\frac{Ahc_b}{m_0} - \frac{m^*}{\tau_h} \quad \Rightarrow \quad \frac{\mathrm{d}m^*}{\mathrm{d}t^*} = -\frac{Ahc_b}{m_0} - \frac{\tau_g}{\tau_h}m^*. \tag{E.2}$$

Note that Ahc_b/m_0 starts at 1 and goes down to 0 just like m^*. For fine dust with negligible settling over timescales where lateral entrainment occurs (i.e., $\tau_g \gg \tau_h$), the gravitational settling term above can be neglected, the lateral dilution term dominates and

$$m^* = e^{-t/\tau_h} \quad \Rightarrow \quad \tau_h = \frac{t}{\ln\,(1/m^*)}. \tag{E.3}$$

From Rodakoviski et al. (2023), for dust with diameter $D_p \simeq 0.9\,\mu$m (which is approximately well-mixed), $m^* = 0.447$ and $t = 5$ days, resulting in $\tau_h \simeq 6.2$ days according to dust concentration measurements from the SALTRACE campaign. Note that, for this size dust, the gravitational settling timescale $\tau_g \simeq 229$ days $\gg \tau_h$.

APPENDIX F

Dimensionless shear rate S_* effects

F.1 Momentum diffusivity

For momentum, we note that $\langle K_u \rangle$ has two contributions,

$$\frac{\langle \varepsilon \rangle}{S^2} \sim S_*^{-2} \sigma_w \ell_\varepsilon, \quad \frac{\Gamma \langle \varepsilon \rangle}{S^2} \sim Ri_g \sigma_w \ell_\varepsilon. \tag{F.1}$$

The first contribution dominates because $\Gamma \lesssim 0.2$, so

$$\langle K_u \rangle = (1+\Gamma) \frac{\ell_\varepsilon \sigma_w}{\beta^2 S_*^2} \simeq \frac{\ell_\varepsilon \sigma_w}{\beta^2 S_*^2} \equiv C_u'' S_*^{-2} \sigma_w \ell_\varepsilon. \tag{F.2}$$

However, our LES data collapsed better when the dependence on S_* was removed. S_* did not vary extensively in our simulations (despite several other parameters being extensively varied), so our LES data set is not appropriate to test this dependence. We therefore incorporate S_* into the constant, so that $\langle K_u \rangle = C_u' \sigma_w \ell_\varepsilon$.

F.2 Buoyancy diffusivity

Young et al. (2022) found better scaling with $\Gamma \sim Fr_T^{-2} S_*^{-1}$. This indeed slightly improved collapse of our Γ values, but the resulting scaling $\langle K_b \rangle \sim S_*^{-1} \sigma_w \ell_\varepsilon$ does not collapse the LES data as well as a simple mixing length model. It does not affect our $\langle K_u \rangle$ scaling, since it is independent from Γ.

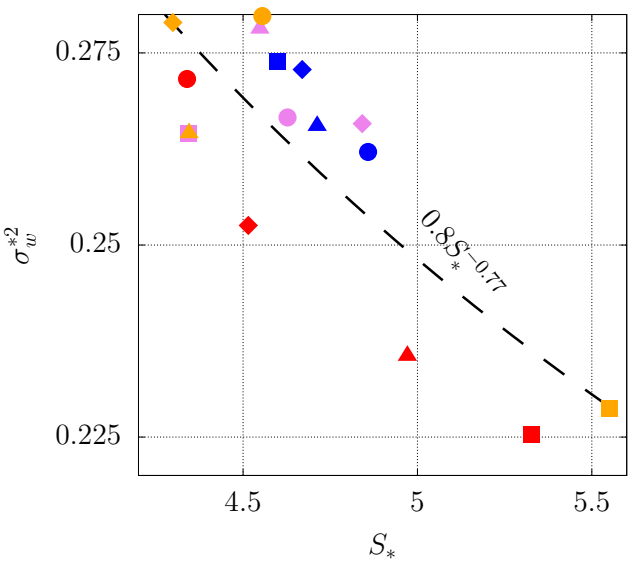

Figure F.1: Dimensionless vertical velocity variance scaling with dimensionless shear rate suggested by analytical solution is not clear in LES data.

F.3 Relationship with σ_w^*

The shear magnitude from the momentum equation solution, $S = Mh/6\langle K_u \rangle$, can be made dimensionless by using the eddy turnover time

$$\tau_e = \frac{\langle k \rangle}{\langle \varepsilon \rangle} = \frac{\sigma_w^2}{\beta \langle \varepsilon \rangle} = \frac{\ell_\varepsilon}{\beta \sigma_w} \quad \Rightarrow \quad S_* = \tau_e S = \frac{\ell_\varepsilon Mh}{6\beta \sigma_w \langle K_u \rangle}. \tag{F.3}$$

If a simple mixing-length model is used for the diffusivity,

$$S_* = \frac{Mh}{6\beta \sigma_w^2 C_u'} = \frac{1}{6\beta \sigma_w^{*2} C_u'} \quad \Rightarrow \quad \sigma_w^{*2} = \left(\frac{1}{6\beta C_u'}\right) S_*^{-1}. \tag{F.4}$$

If the diffusivity scaling with S_*^{-2} is maintained,

$$S_* = \frac{Mh}{6\beta \sigma_w^2 C_u'' S_*^{-2}} \quad \Rightarrow \quad \sigma_w^{*2} = \left(\frac{1}{6\beta C_u''}\right) S_*. \tag{F.5}$$

Figure F.1 shows that our LES data suggest a decrease in σ_w^{*2} as S_* increases, supporting the mixing-length model. We do not vary S_* extensively in our study (as opposed to Young et al. (2022), for instance), so our dataset is not ideal to test these relations. For that reason, we treat σ_w^* and S_* as a constant.

APPENDIX G

Independent dimensionless parameters

G.1 Aspect ratio

In reality, the finite horizontal extent of the LES domain adds two aspect ratios to the list of controling parameters (eqn. (14) in the main text), but we do not investigate their influence on the flow dynamics and keep $h/L_x = h/L_y = 0.25$ fixed. In practice, they will only influence the solution if they are not small enough (which would be unphysical). So as long as these ARs are small enough, which they are, we prevent artificial effects of the periodic boundary conditions, and the solution should be independent of these ARs.

G.2 Another analytical expression for the eddy diffusivity

Note that (3.24) depends solely on Ri_g, but from the Buckingham Π theorem it could depend on something else. This possible simplification may have arisen from correlations between dimensionless parameters in our LES runs, which may have emerged from the flow physics (i.e., there is an attractor, and not the entire phase space is accessible for real flows), or it may be a result of our LES exploring only a limited subset of the entire parameter space (e.g., mostly weakly stratified flows, or the fact that S_* and σ_w^* did not vary extensively in our simulations).

Moreover, we have no guarantee that we can use (3.24) with such a broad range of values for Δb, h and S so as to produce Π_1, Π_2 values for which (3.24) has not been tested for. This is because (3.24) was derived based on an empirical fit based on LES data combining 4 different values of Π_1 with 4 different values of Π_2. Hence, although our LES runs were designed to simulate typical SAL conditions, any given SAL event might be different (e.g., strongly stratified).

We can force Ri_g to appear in an analytical expression for the eddy diffusivities by taking the ratio between the dimensional solutions in (3.11) and (3.13). Recognizing the dimensionless variables that show up and rearranging the terms, one can write the following quadratic equation for the vertically-averaged eddy viscosity:

$$\frac{\langle K_u \rangle^2}{Mh^3} - \left(\frac{\mathrm{Ri}_g \Pi_2^{1/2}}{3\,\mathrm{Pr}_T\,\Pi_1^{3/2}} \right) \frac{\langle K_u \rangle}{\sqrt{Mh^3}} - \frac{\mathrm{Ri}_g}{36\Pi_1} = 0. \tag{G.1}$$

This equation has only one positive solution which is given by

$$\frac{\langle K_u \rangle}{\sqrt{Mh^3}} = \frac{1}{6}\sqrt{\frac{\mathrm{Ri}_g}{\Pi_1}} \left(\Lambda + \sqrt{1+\Lambda^2} \right), \quad \Lambda \equiv \frac{\sqrt{\mathrm{Ri}_g \Pi_2}}{\mathrm{Pr}_T\,\Pi_1}. \tag{G.2}$$

Using the momentum equation solution (3.11), we can rewrite $\langle K_u \rangle$ in terms of the shear magnitude, namely

$$\frac{\langle K_u \rangle}{h^2 S} = \frac{\mathrm{Ri}_g}{6\Pi_1} \left(\Lambda + \sqrt{1+\Lambda^2} \right)^2. \tag{G.3}$$

The temperature diffusivity is $\langle K_\theta \rangle = \mathrm{Pr}_T^{-1} \langle K_u \rangle$. This does not depend on the empirical fit for ℓ_ε from our LES, so it may be more general than (3.24) which depends only on Ri_g. However, this analytical solution depends on more than 2 dimensionless parameters, so it is somewhat redundant. For instance, it may look like $\langle K_u \rangle$ increases with Ri_g, but there are hidden dependences among the variables, so Ri_g cannot change while Π_1 and Λ are simultaneously held constant. This can be seen by taking the ratio between the dimensionless solutions in (3.11) and (3.13) to obtain

$$\mathrm{Ri}_g = \frac{\Pi_1}{\alpha^2 (1 + 2/\gamma)}. \tag{G.4}$$

This shows that Ri_g can be determined by forcing parameters (via Π_1) and the flow turbulent response (via α, γ), which is ultimately uniquely determined by (Π_1, Π_2). Unfortunately, it is challenging to get rid of this kind of redundance in this problem.

There are also asymptotic relations for small and large Λ:

$$\frac{\langle K_u \rangle}{h^2 S} \to \frac{\mathrm{Ri}_g}{6\Pi_1} \text{ as } \Lambda \to 0, \qquad \frac{\langle K_u \rangle}{h^2 S} \to \frac{2\mathrm{Ri}_g \Lambda^2}{3\Pi_1} = \frac{2\mathrm{Ri}_g^2 \Pi_2}{3\,\mathrm{Pr}_T\,\Pi_1^3} \text{ as } \Lambda \to \infty. \tag{G.5}$$

So the explicit dependence upon Π_2 is removed at small Λ. In our simulations, small Λ is associated with high Ri_g

APPENDIX H

Richardson number considerations

H.1 Parameterizing mixing in global models

Our model is based on the Richardson number Ri_g defined in (3.1), which is calculated based on background N^2 and S^2, which are already smooth ensemble averages. Global models evolve averaged variables, and our model can thus be used under weak stratification. At strong stratification, only local values of Ri_ℓ will be small, and the potential for local shear/convective stability (and the associated potential for turbulent mixing) is better described by Ri_ℓ, such as the profiles in figure 3.3. Large-scale models, however, generally compute averages over grid cells, so they are insensitive to the locally small Ri_ℓ values, and one should use caution when parameterizing turbulent mixing using Ri_g under strong stratification.

Ri_ℓ can be well described in terms of PDFs, like the ones in figure figure H.1. The PDFs calculated from numerical simulation data of Brethouwer et al. (2007) show a peak at $\mathrm{Ri}_\ell = 0$ when $\mathrm{Re}_b > 1$, indicating the presence of intense 3D mixing. The PDF of Dörnbrack et al. (2022) for data collected near the tropopause peak near $\mathrm{Ri}_\ell \simeq 1$.

We also note that, although (3.24) and other models set $\langle K \rangle = 0$ at a certain critical $\mathrm{Ri}_g = r$ value, in reality some eddy mixing still takes place at $\mathrm{Ri}_g > r$. For instance, Peters et al. (1988) found eddy diffusivity coefficients much larger than their molecular counterparts (by more than one order of magnitude) at large Ri_g values. Moreover, the interpretation and usage of the linear stability threshold $\mathrm{Ri}_g = 0.25$ of Miles (1961) and Howard (1961) is often wrong, as discussed by Galperin et al. (2007). Issaev et al. (2022) reports clearly observing sustained turbulence and vigorous mixing at $\mathrm{Ri}_g > 0.25$. So turbulence does not shut down above $\mathrm{Ri}_g = 0.25$, and although $\langle K \rangle$ is substantially reduced, it can still be relevant for flows (and processes) with long timescales.

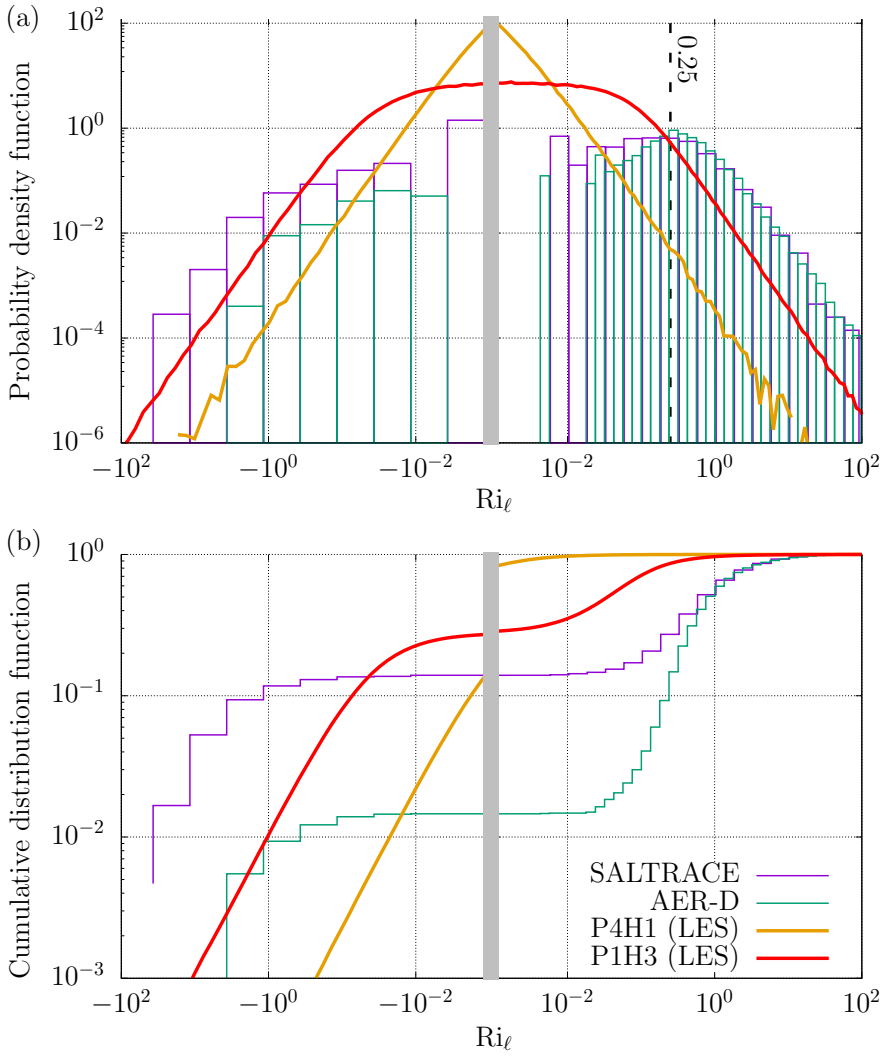

Figure H.1: Observed and simulated (a) PDF and (b) CDF of instantaneous, local Richardson number in the SAL (bars) and our LES (thick lines). Note that AER-D data peaks around 0.25.

H.2 Resolution effects on Richardson number estimates

In measurements and simulations, it is important to resolve the Ozmidov and Corrsin scales, since coarse profiles remove both large and small Ri_ℓ peaks, whereas smoothed profiles seem to insert a bias towards large Ri_g, as shown in figure H.2. This would have the implication of underestimating turbulent mixing.

Meeting resolution requirements is especially challenging in the LAST regime. Because $\mathrm{Fr}_T \sim (\ell_O/\ell_z)^2$ and $\mathrm{Re}_b \sim (\ell_O/\eta_K)^{4/3}$, where $\eta_K = \sqrt[4]{\nu^3/\langle\varepsilon\rangle}$ is the Kolmogorov microscale, the limits defining LAST ($\mathrm{Fr}_T \ll 1$, $\mathrm{Re}_b \gg 1$) imply $\eta_K \ll \ell_O \ll \ell_z$ (Bartello et al., 2013). Hence, the Ozmidov scale is well below the integral scale in this regime, meaning that a broad range of scales must be resolved in LES (and even more so in DNS). On the other hand, under weak stratification, ℓ_O can be large, and a large Re_b value guarantees that there will be an inertial range of scales that is unaffected by large-scale stratification at which the grid size can be placed.

H.3 SAL sublayers

In general, the SAL does not have uniform S and N (and therefore Ri_g) in the interior like in our idealized set-up. Our theory might be applicable to uniform sublayers where that condition is approximately met, like the ones in figure H.3. However, those are instantaneous profiles which are evolving in time. Note that they display the staircase-like profile akin to the LAST regime of stratified turbulence.

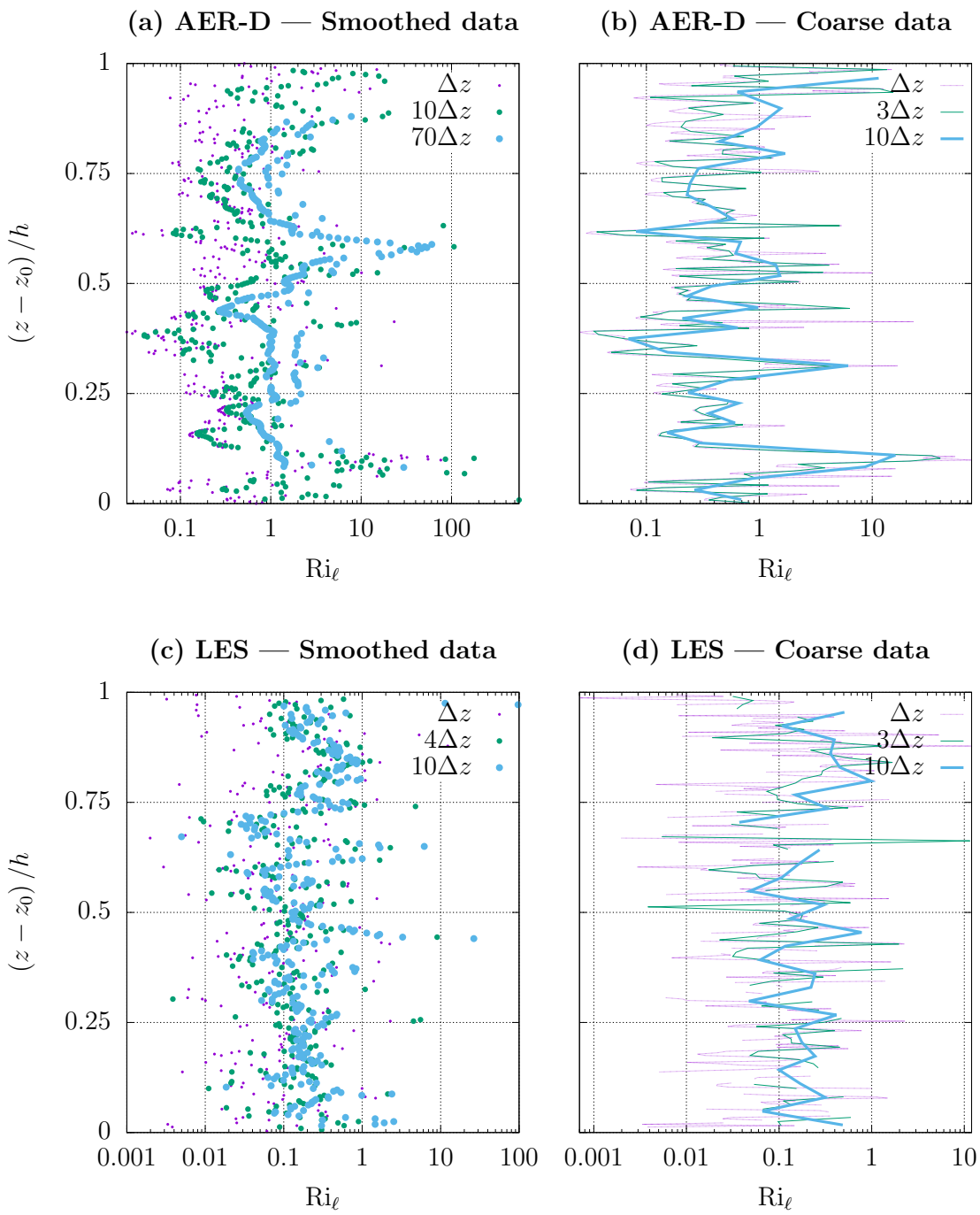

Figure H.2: Local, instantaneous gradient Richardson number profiles based on AER-D observations (top row) and LES (bottom row) data. The left column shows the effect of applying a moving average on temperature and wind profiles, whereas the right column shows the effect of sampling those data with a coarser resolution on the resulting Ri_ℓ. This shows that the actual Richardson number might be smaller than observed or modeled due to effects of spatial averaging or coarse resolution.

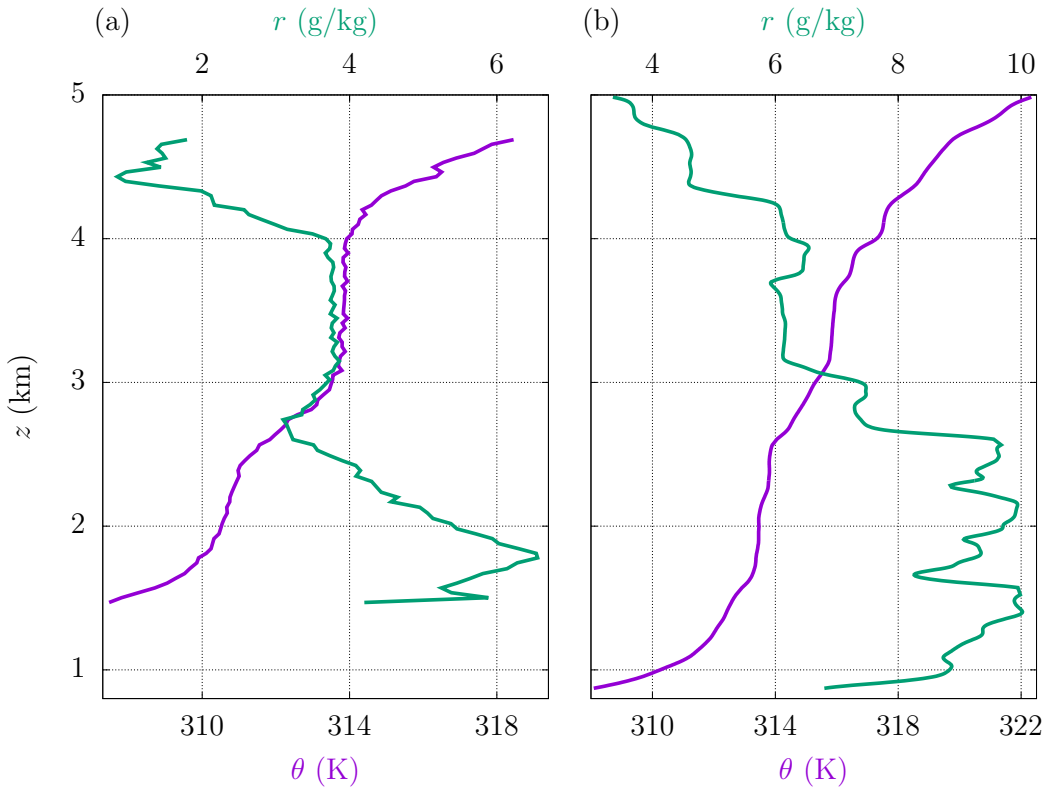

Figure H.3: Examples of SAL profiles of potential temperature θ and water vapor mixing ratio r observed during the (a) SALTRACE and (b) AER-D campaigns showing nearly well-mixed sublayers separated by stratified regions.

Bibliography

[1] Adeyemi A Adebiyi and Jasper F Kok. “Climate models miss most of the coarse dust in the atmosphere”. In: *Science advances* 6.15 (2020), eaaz9507.

[2] GP Anderson, SA Clough, FX Kneizys, JH Chetwynd, and EP Shettle. *AFGL atmospheric constituent profiles (0–120 km). Air Force Geophysics Laboratory Tech. Rep*. Tech. rep. AFGL-TR-86-0110, 1986.

[3] Prosenjit Bagchi and S Balachandar. “Effect of turbulence on the drag and lift of a particle”. In: *Physics of fluids* 15.11 (2003), pp. 3496–3513.

[4] S Balachandar and John K Eaton. “Turbulent dispersed multiphase flow”. In: *Annual review of fluid mechanics* 42 (2010), pp. 111–133.

[5] P Bartello and SM Tobias. “Sensitivity of stratified turbulence to the buoyancy Reynolds number”. In: *Journal of Fluid Mechanics* 725 (2013), pp. 1–22.

[6] Emily Bercos-Hickey, Terrence R Nathan, and Shu-Hua Chen. “On the relationship between the African Easterly Jet, Saharan mineral dust aerosols, and West African precipitation”. In: *Journal of Climate* 33.9 (2020), pp. 3533–3546.

[7] Emily Bercos-Hickey, Terrence R Nathan, and Shu-Hua Chen. “Saharan dust and the African easterly jet–African easterly wave system: Structure, location and energetics”. In: *Quarterly Journal of the Royal Meteorological Society* 143.708 (2017), pp. 2797–2808.

[8] PR Betzer, KL Carder, RA Duce, JT Merrill, NW Tindale, M Uematsu, DK Costello, RW Young, RA Feely, JA Breland, et al. “Long–range transport of giant mineral aerosol particles”. In: *Nature* 336.6199 (1988), pp. 568–571.

[9] Yvonne Boose, Berko Sierau, M Isabel García, Sergio Rodríguez, Andrés Alastuey, Claudia Linke, Martin Schnaiter, Piotr Kupiszewski, Zamin A Kanji, and Ulrike Lohmann. “Ice nucleating particles in the Saharan Air Layer”. In: *Atmospheric Chemistry and Physics* 16.14 (2016), pp. 9067–9087.

[10] Elie Bou-Zeid, Charles Meneveau, and Marc Parlange. “A scale-dependent Lagrangian dynamic model for large eddy simulation of complex turbulent flows”. In: *Physics of fluids* 17.2 (2005).

[11] Howard Brenner. “The diffusion model of longitudinal mixing in beds of finite length. Numerical values”. In: *Chemical Engineering Science* 17.4 (1962), pp. 229–243.

[12] Christopher S Bretherton and Sungsu Park. “A new moist turbulence parameterization in the Community Atmosphere Model”. In: *Journal of Climate* 22.12 (2009), pp. 3422–3448.

[13] Geert Brethouwer, Paul Billant, Erik Lindborg, and J-M Chomaz. “Scaling analysis and simulation of strongly stratified turbulent flows”. In: *Journal of Fluid Mechanics* 585 (2007), pp. 343–368.

[14] Garry L Brown and Anatol Roshko. “On density effects and large structure in turbulent mixing layers”. In: *Journal of Fluid Mechanics* 64.4 (1974), pp. 775–816.

[15] Tristan M Burton and John K Eaton. “Fully resolved simulations of particle-turbulence interaction”. In: *Journal of Fluid Mechanics* 545 (2005), pp. 67–111.

[16] Toby N Carlson. “The Saharan elevated mixed layer and its aerosol optical depth”. In: *The Open Atmospheric Science Journal* 10.1 (2016).

[17] Toby N Carlson and Joseph M Prospero. “The large-scale movement of Saharan air outbreaks over the northern equatorial Atlantic”. In: *Journal of Applied Meteorology and Climatology* 11.2 (1972), pp. 283–297.

[18] CP Caulfield. “Layering, instabilities, and mixing in turbulent stratified flows”. In: *Annual Review of Fluid Mechanics* 53 (2021), pp. 113–145.

[19] Marcelo Chamecki, Nelson L Dias, and Livia S Freire. “A TKE-based framework for studying disturbed atmospheric surface layer flows and application to vertical velocity variance over canopies”. In: *Geophysical Research Letters* 45.13 (2018), pp. 6734–6740.

[20] Marcelo Chamecki, Charles Meneveau, and Marc B Parlange. “A hybrid spectral/finite-volume algorithm for large-eddy simulation of scalars in the atmospheric boundary layer”. In: *Boundary-layer meteorology* 128.3 (2008), pp. 473–484.

[21] Marcelo Chamecki, Charles Meneveau, and Marc B Parlange. “Large eddy simulation of pollen transport in the atmospheric boundary layer”. In: *Journal of Aerosol Science* 40.3 (2009), pp. 241–255.

[22] Chia-Te Chien, Katherine RM Mackey, Stephanie Dutkiewicz, Natalie M Mahowald, Joseph M Prospero, and Adina Paytan. “Effects of African dust deposition on phytoplankton in the western tropical Atlantic Ocean off Barbados”. In: *Global Biogeochemical Cycles* 30.5 (2016), pp. 716–734.

[23] Tomas Chor, Jacob O Wenegrat, and John Taylor. “Insights into the Mixing Efficiency of Submesoscale Centrifugal–Symmetric Instabilities”. In: *Journal of Physical Oceanography* 52.10 (2022), pp. 2273–2287.

[24] Roland Clift, John R Grace, and Martin E Weber. “Bubbles, drops, and particles”. In: (2005).

[25] Kerry H Cook. “Generation of the African easterly jet and its role in determining West African precipitation”. In: *Journal of climate* 12.5 (1999), pp. 1165–1184.

[26] Kerry H Cook. “Generation of the African easterly jet and its role in determining West African precipitation”. In: *Journal of climate* 12.5 (1999), pp. 1165–1184.

[27] GT Csanady. “Turbulent diffusion of heavy particles in the atmosphere”. In: *Journal of Atmospheric Sciences* 20.3 (1963), pp. 201–208.

[28] Joan Cuxart, Albert AM Holtslag, Robert J Beare, E Bazile, Anton Beljaars, A Cheng, L Conangla, M Ek, F Freedman, R Hamdi, et al. “Single-column model intercomparison for a stably stratified atmospheric boundary layer”. In: *Boundary-Layer Meteorology* 118 (2006), pp. 273–303.

[29] Peter Davidson. *Turbulence: an introduction for scientists and engineers*. Oxford university press, 2015.

[30] Eric Deleersnijder, Jean-Marie Beckers, and Eric JM Delhez. “The residence time of settling particles in the surface mixed layer”. In: *Environmental Fluid Mechanics* 6.1 (2006), pp. 25–42.

[31] Paul J DeMott, Kenneth Sassen, Michael R Poellot, Darrel Baumgardner, David C Rogers, Sarah D Brooks, Anthony J Prenni, and Sonia M Kreidenweis. “African dust aerosols as atmospheric ice nuclei”. In: *Geophysical Research Letters* 30.14 (2003).

[32] Coleman duP Donaldson and Glenn R Hilst. “Effect of inhomogeneous mixing on atmospheric photochemical reactions”. In: *Environmental Science & Technology* 6.9 (1972), pp. 812–816.

[33] Andreas Dörnbrack, Peter Bechtold, and Ulrich Schumann. “High-resolution aircraft observations of turbulence and waves in the free atmosphere and comparison with global model predictions”. In: *Journal of Geophysical Research: Atmospheres* 127.16 (2022), e2022JD036654.

[34] Jason P Dunion and Christopher S Velden. “The impact of the Saharan air layer on Atlantic tropical cyclone activity”. In: *Bulletin of the American Meteorological Society* 85.3 (2004), pp. 353–366.

[35] Amato T Evan, Gregory R Foltz, Dongxiao Zhang, and Daniel J Vimont. “Influence of African dust on ocean–atmosphere variability in the tropical Atlantic”. In: *Nature Geoscience* 4.11 (2011), pp. 762–765.

[36] Matthew Falder, NJ White, and CP Caulfield. “Seismic imaging of rapid onset of stratified turbulence in the South Atlantic Ocean”. In: *Journal of Physical Oceanography* 46.4 (2016), pp. 1023–1044.

[37] William M Frank and John Molinari. “Convective adjustment”. In: *The Representation of Cumulus Convection in Numerical Models*. Springer, 1993, pp. 101–105.

[38] LS Freire, M Chamecki, and JA Gillies. “Flux-profile relationship for dust concentration in the stratified atmospheric surface layer”. In: *Boundary-layer meteorology* 160.2 (2016), pp. 249–267.

[39] Boris Galperin, Semion Sukoriansky, and Philip S Anderson. “On the critical Richardson number in stably stratified turbulence”. In: *Atmospheric Science Letters* 8.3 (2007), pp. 65–69.

[40] Amrapalli Garanaik and Subhas K Venayagamoorthy. “On the inference of the state of turbulence and mixing efficiency in stably stratified flows”. In: *Journal of Fluid Mechanics* 867 (2019), pp. 323–333.

[41] Luis Garcia-Carreras, DJ Parker, JH Marsham, PD Rosenberg, IM Brooks, AP Lock, F Marenco, JB McQuaid, and M Hobby. “The turbulent structure and diurnal growth of the Saharan atmospheric boundary layer”. In: *Journal of the Atmospheric Sciences* 72.2 (2015), pp. 693–713.

[42] Josef Gasteiger, Silke Groß, Daniel Sauer, Moritz Haarig, Albert Ansmann, and Bernadett Weinzierl. “Particle settling and vertical mixing in the Saharan Air Layer as seen from an integrated model, lidar, and in situ perspective”. In: *Atmospheric Chemistry and Physics* 17.1 (2017), pp. 297–311.

[43] MC Gregg. “Estimation and geography of diapycnal mixing in the stratified ocean”. In: *Physical processes in lakes and oceans* 54 (1998), pp. 305–338.

[44] Manuel Gutleben and S Groß. “Turbulence Analysis in Long-Range-Transported Saharan Dust Layers With Airborne Lidar”. In: *Geophysical Research Letters* 48.18 (2021), e2021GL094418.

[45] Manuel Gutleben, Silke Groß, Martin Wirth, Claudia Emde, and Bernhard Mayer. “Impacts of water vapor on Saharan air layer radiative heating”. In: *Geophysical Research Letters* 46.24 (2019), pp. 14854–14862.

[46] JOST Heintzenberg. “The SAMUM-1 experiment over Southern Morocco: overview and introduction”. In: *Tellus B: Chemical and Physical Meteorology* 61.1 (2009), pp. 2–11.

[47] Jackson R Herring and Olivier Métais. “Numerical experiments in forced stably stratified turbulence”. In: *Journal of Fluid Mechanics* 202 (1989), pp. 97–115.

[48] William C Hinds. *Aerosol technology: properties, behavior, and measurement of airborne particles*. John Wiley & Sons, 1999.

[49] AAM Holtslag and BA Boville. “Local versus nonlocal boundary-layer diffusion in a global climate model”. In: *Journal of climate* 6.10 (1993), pp. 1825–1842.

[50] Louis N Howard. “Note on a paper of John W. Miles”. In: *Journal of Fluid Mechanics* 10.4 (1961), pp. 509–512.

[51] Yue Huang, Jasper F Kok, Konrad Kandler, Hannakaisa Lindqvist, Timo Nousiainen, Tetsu Sakai, Adeyemi Adebiyi, and Olli Jokinen. “Climate models and remote sensing retrievals neglect substantial desert dust asphericity”. In: *Geophysical Research Letters* 47.6 (2020), e2019GL086592.

[52] IPCC. “Climate Change 2021: The Physical Science Basis”. In: (2021).

[53] Vassili Issaev, N Williamson, SW Armfield, and SE Norris. “Parameterization of mixing in stratified open channel flow”. In: *Journal of Fluid Mechanics* 935 (2022), A17.

[54] Michael Jähn, Domingo Muñoz-Esparza, Fernando Chouza, Oliver Reitebuch, Oswald Knoth, Moritz Haarig, and Albert Ansmann. “Investigations of boundary layer structure, cloud characteristics and vertical mixing of aerosols at Barbados with large eddy simulations”. In: *Atmospheric Chemistry and Physics* 16.2 (2016), pp. 651–674.

[55] Eunsil Jung, Bruce Albrecht, Joseph M Prospero, Haflidi H Jonsson, and Sonia M Kreidenweis. “Vertical structure of aerosols, temperature, and moisture associated with an intense African dust event observed over the eastern Caribbean”. In: *Journal of Geophysical Research: Atmospheres* 118.10 (2013), pp. 4623–4643.

[56] VA Karydis, P Kumar, D Barahona, IN Sokolik, and Athanasios Nenes. “On the effect of dust particles on global cloud condensation nuclei and cloud droplet number”. In: *Journal of Geophysical Research-Atmospheres* 116.GSFC-E-DAA-TN8102 (2011).

[57] Sina Khani. “Mixing efficiency in large-eddy simulations of stratified turbulence”. In: *Journal of Fluid Mechanics* 849 (2018), pp. 373–394.

[58] Dongchul Kim, Mian Chin, Hongbin Yu, Thomas Diehl, Qian Tan, Ralph A Kahn, Kostas Tsigaridis, Susanne E Bauer, Toshihiko Takemura, Luca Pozzoli, et al. “Sources, sinks, and transatlantic transport of North African dust aerosol: A multimodel analysis and comparison with remote sensing data”. In: *Journal of Geophysical Research: Atmospheres* 119.10 (2014), pp. 6259–6277.

[59] RJ Kind. “One-dimensional aeolian suspension above beds of loose particles—A new concentration-profile equation”. In: *Atmospheric Environment. Part A. General Topics* 26.5 (1992), pp. 927–931.

[60] Jasper F Kok, Adeyemi A Adebiyi, Samuel Albani, Yves Balkanski, Ramiro Checa-Garcia, Mian Chin, Peter R Colarco, Douglas S Hamilton, Yue Huang, Akinori Ito, et al. “Contribution of the world’s main dust source regions to the global cycle of desert dust”. In: *Atmospheric Chemistry and Physics* 21.10 (2021), pp. 8169–8193.

[61] Jasper F Kok, David A Ridley, Qing Zhou, Ron L Miller, Chun Zhao, Colette L Heald, Daniel S Ward, Samuel Albani, and Karsten Haustein. “Smaller desert dust cooling effect estimated from analysis of dust size and abundance”. In: *Nature Geoscience* 10.4 (2017), pp. 274–278.

[62] Pijush K Kundu, Ira M Cohen, and David R Dowling. *Fluid mechanics*. Academic press, 2015.

[63] J-P Laval, James C McWilliams, and Berangere Dubrulle. “Forced stratified turbulence: successive transitions with Reynolds number”. In: *Physical Review E* 68.3 (2003), p. 036308.

[64] Dan Li. “Turbulent Prandtl number in the atmospheric boundary layer-where are we now?” In: *Atmospheric Research* 216 (2019), pp. 86–105.

[65] Jung-Tai Lin and Yih-Ho Pao. “Wakes in stratified fluids”. In: *Annual Review of Fluid Mechanics* 11.1 (1979), pp. 317–338.

[66] Andrea Maffioli, Geert Brethouwer, and Erik Lindborg. “Mixing efficiency in stratified turbulence”. In: *Journal of Fluid Mechanics* 794 (2016), R3.

[67] Sotirios A Mallios, Vasiliki Daskalopoulou, and Vassilis Amiridis. “Modeling of the electrical interaction between desert dust particles and the Earth’s atmosphere”. In: *Journal of Aerosol Science* 165 (2022), p. 106044.

[68] Sotirios A Mallios, Eleni Drakaki, and Vassilis Amiridis. “Effects of dust particle sphericity and orientation on their gravitational settling in the earth’s atmosphere”. In: *Journal of Aerosol Science* 150 (2020), p. 105634.

[69] H Maring, DL Savoie, MA Izaguirre, L Custals, and JS Reid. “Mineral dust aerosol size distribution change during atmospheric transport”. In: *Journal of Geophysical Research: Atmospheres* 108.D19 (2003).

[70] CL McConnell, EJ Highwood, H Coe, P Formenti, B Anderson, S Osborne, S Nava, K Desboeufs, G Chen, and MAJ Harrison. “Seasonal variations of the physical and optical characteristics of Saharan dust: Results from the Dust Outflow and Deposition to the Ocean (DODO) experiment”. In: *Journal of Geophysical Research: Atmospheres* 113.D14 (2008).

[71] Nick J Middleton. “Desert dust hazards: A global review”. In: *Aeolian research* 24 (2017), pp. 53–63.

[72] John W Miles. “On the stability of heterogeneous shear flows”. In: *Journal of Fluid Mechanics* 10.4 (1961), pp. 496–508.

[73] Mostafa Momen, Elie Bou-Zeid, Marc B Parlange, and Marco Giometto. “Modulation of mean wind and turbulence in the atmospheric boundary layer by baroclinicity”. In: *Journal of the Atmospheric Sciences* 75.11 (2018), pp. 3797–3821.

[74] O Muñoz, H Volten, JW Hovenier, Timo Nousiainen, K Muinonen, D Guirado, F Moreno, and LBFM Waters. “Scattering matrix of large Saharan dust particles: Experiments and computations”. In: *Journal of Geophysical Research: Atmospheres* 112.D13 (2007).

[75] Terrence R Nathan and Dustin FP Grogan. “Scale-Dependent Transport of Saharan Dust by African Easterly Waves”. In: *Geosciences* 12.9 (2022), p. 337.

[76] KA Nicoll, RG Harrison, and Z Ulanowski. “Observations of Saharan dust layer electrification”. In: *Environmental Research Letters* 6.1 (2010), p. 014001.

[77] FTM Nieuwstadt. “Some aspects of the turbulent stable boundary layer”. In: *Boundary-Layer Meteorology* 30 (1984), pp. 31–55.

[78] Thomas R Osborn. “Estimates of the local rate of vertical diffusion from dissipation measurements”. In: *Journal of physical oceanography* 10.1 (1980), pp. 83–89.

[79] Sebastian Otto, Marian de Reus, Thomas Trautmann, Andreas Thomas, Manfred Wendisch, and Stephan Borrmann. “Atmospheric radiative effects of an in situ measured Saharan dust plume and the role of large particles”. In: *Atmospheric Chemistry and Physics* 7.18 (2007), pp. 4887–4903.

[80] H Peters, MC Gregg, and JM Toole. “On the parameterization of equatorial turbulence”. In: *Journal of Geophysical Research: Oceans* 93.C2 (1988), pp. 1199–1218.

[81] Stephen B Pope. *Turbulent flows*. Cambridge university press, 2000.

[82] Gavin D Portwood, Stephen M de Bruyn Kops, John Ryan Taylor, H Salehipour, and CP Caulfield. “Robust identification of dynamically distinct regions in stratified turbulence”. In: *Journal of fluid mechanics* 807 (2016), R2.

[83] Ludwig Prandtl. “Essentials of fluid dynamics, Blackie and Son, Ltd”. In: *London and Glasgow* 452 (1952).

[84] Santosh Rana, William Anderson, and Mackenzie Day. “An entrainment paradox: how hysteretic saltation and secondary transport augment atmospheric uptake of aeolian source materials”. In: *Journal of Geophysical Research: Atmospheres* 126.10 (2021), e2020JD033493.

[85] Jeffrey S Reid, James E Kinney, Douglas L Westphal, Brent N Holben, Ellsworth J Welton, Si-Chee Tsay, Daniel P Eleuterio, James R Campbell, Sundar A Christopher, PR Colarco, et al. “Analysis of measurements of Saharan dust by airborne and ground-based remote sensing methods during the Puerto Rico Dust Experiment (PRIDE)”. In: *Journal of Geophysical Research: Atmospheres* 108.D19 (2003).

[86] David Richter and Marcelo Chamecki. “Inertial effects on the vertical transport of suspended particles in a turbulent boundary layer”. In: *Boundary-layer meteorology* 167.2 (2018), pp. 235–256.

[87] DA Ridley, CL Heald, and B Ford. “North African dust export and deposition: A satellite and model perspective”. In: *Journal of Geophysical Research: Atmospheres* 117.D2 (2012).

[88] Franziska Rittmeister, Albert Ansmann, Ronny Engelmann, Annett Skupin, Holger Baars, Thomas Kanitz, and Stefan Kinne. “Profiling of Saharan dust from the Caribbean to western Africa–Part 1: Layering structures and optical properties from shipborne polarization/Raman lidar observations”. In: *Atmospheric Chemistry and Physics* 17.21 (2017), pp. 12963–12983.

[89] Rodrigo Rodakoviski and Marcelo Chamecki. “Shear-induced vertical mixing in a stratified Saharan Air Layer”. In: (In prep).

[90] Rodrigo Rodakoviski and Nelson L Dias. “Direct simulation of two-dimensional Benard flow with free-slip boundary conditions”. In: *Computers & Fluids* 228 (2021), p. 105040.

[91] Rodrigo Rodakoviski, Jasper Kok, and Marcelo Chamecki. “Dust settling from turbulent layers in the free troposphere: Implications for the Saharan Air Layer”. In: *Journal of Geophysical Research: Atmospheres* 128.6 (2023), e2022JD037724.

[92] Javier Ruiz. “The role of turbulence in the sedimentation loss of pelagic aggregates from the mixed layer”. In: *Journal of Marine Research* 54.2 (1996), pp. 385–406.

[93] CL Ryder. “Radiative effects of increased water vapor in the upper Saharan Air Layer associated with enhanced dustiness”. In: *Journal of Geophysical Research: Atmospheres* 126.21 (2021), e2021JD034696.

[94] Claire L Ryder, Franco Marenco, Jennifer K Brooke, Victor Estelles, Richard Cotton, Paola Formenti, James B McQuaid, Hannah C Price, Dantong Liu, Patrick Ausset, et al. “Coarse-mode mineral dust size distributions, composition and optical properties from AER-D aircraft measurements over the tropical eastern Atlantic”. In: *Atmospheric Chemistry and Physics* 18.23 (2018), pp. 17225–17257.

[95] Hesam Salehipour and WR Peltier. “Diapycnal diffusivity, turbulent Prandtl number and mixing efficiency in Boussinesq stratified turbulence”. In: *Journal of Fluid Mechanics* 775 (2015), pp. 464–500.

[96] Ulrich Schumann, Paul Konopka, Robert Baumann, R Busen, T Gerz, H Schlager, P Schulte, and H Volkert. “Estimate of diffusion parameters of aircraft exhaust plumes near the tropopause from nitric oxide and turbulence measurements”. In: *Journal of Geophysical Research: Atmospheres* 100.D7 (1995), pp. 14147–14162.

[97] Yaping Shao. *Physics and Modeling of Wind Erosion*. 2^{2nd}. Springer, 2008.

[98] Lucinda H Shih, Jeffrey R Koseff, Joel H Ferziger, and Chris R Rehmann. "Scaling and parameterization of stratified homogeneous turbulent shear flow". In: *Journal of Fluid Mechanics* 412 (2000), pp. 1–20.

[99] Lucinda H Shih, Jeffrey R Koseff, Gregory N Ivey, and Joel H Ferziger. "Parameterization of turbulent fluxes and scales using homogeneous sheared stably stratified turbulence simulations". In: *Journal of Fluid Mechanics* 525 (2005), pp. 193–214.

[100] H Siebert, M Beals, J Bethke, E Bierwirth, T Conrath, K Dieckmann, F Ditas, A Ehrlich, D Farrell, S Hartmann, et al. "The fine-scale structure of the trade wind cumuli over Barbados–an introduction to the CARRIBA project". In: *Atmospheric Chemistry and Physics* 13.19 (2013), pp. 10061–10077.

[101] Roland B Stull. *An introduction to boundary layer meteorology*. Vol. 13. Springer Science & Business Media, 1988.

[102] Peter P Sullivan, Chin-Hoh Moeng, Bjorn Stevens, Donald H Lenschow, and Shane D Mayor. "Structure of the entrainment zone capping the convective atmospheric boundary layer". In: *Journal of the atmospheric sciences* 55.19 (1998), pp. 3042–3064.

[103] D Tanré, J Haywood, J Pelon, JF Léon, B Chatenet, P Formenti, P Francis, P Goloub, EJ Highwood, and G Myhre. "Measurement and modeling of the Saharan dust radiative impact: Overview of the Saharan Dust Experiment (SHADE)". In: *Journal of Geophysical Research: Atmospheres* 108.D18 (2003).

[104] Joseph R Toth III, Siddharth Rajupet, Henry Squire, Blaire Volbers, Jùn Zhou, Li Xie, R Mohan Sankaran, and Daniel J Lacks. "Electrostatic forces alter particle size distributions in atmospheric dust". In: *Atmospheric Chemistry and Physics* 20.5 (2020), pp. 3181–3190.

[105] Kwan-Leung Tse, Alex Mahalov, Basil Nicolaenko, and HJS Fernando. "Quasi-equilibrium dynamics of shear-stratified turbulence in a model tropospheric jet". In: *journal of fluid mechanics* 496 (2003), pp. 73–103.

[106] Konstantinos Tsigaridis, M Krol, FJ Dentener, Yves Balkanski, J Lathiere, S Metzger, DA Hauglustaine, and M Kanakidou. “Change in global aerosol composition since preindustrial times”. In: *Atmospheric Chemistry and Physics* 6.12 (2006), pp. 5143–5162.

[107] Cynthia H Twohy, Sonia M Kreidenweis, Trude Eidhammer, Edward V Browell, Andrew J Heymsfield, Aaron R Bansemer, Bruce E Anderson, Gao Chen, Syed Ismail, Paul J DeMott, et al. “Saharan dust particles nucleate droplets in eastern Atlantic clouds”. In: *Geophysical Research Letters* 36.1 (2009).

[108] Michèlle Van Der Does, Peter Knippertz, Philipp Zschenderlein, R Giles Harrison, and Jan-Berend W Stuut. “The mysterious long-range transport of giant mineral dust particles”. In: *Science advances* 4.12 (2018), eaau2768.

[109] Bernadett Weinzierl, Albert Ansmann, Joseph M Prospero, Dietrich Althausen, N Benker, F Chouza, Maximilian Dollner, D Farrell, WK Fomba, Volker Freudenthaler, et al. “The Saharan aerosol long-range transport and aerosol–cloud-interaction experiment: overview and selected highlights”. In: *Bulletin of the American Meteorological Society* 98.7 (2017), pp. 1427–1451.

[110] CD Westbrook. “The fall speeds of sub-100 μm ice crystals”. In: *Quarterly Journal of the Royal Meteorological Society: A journal of the atmospheric sciences, applied meteorology and physical oceanography* 134.634 (2008), pp. 1243–1251.

[111] Sabine Wurzler, Tamir G Reisin, and Zev Levin. “Modification of mineral dust particles by cloud processing and subsequent effects on drop size distributions”. In: *Journal of Geophysical Research: Atmospheres* 105.D4 (2000), pp. 4501–4512.

[112] I Wygnanski and Heinrich E Fiedler. “The two-dimensional mixing region”. In: *Journal of Fluid Mechanics* 41.2 (1970), pp. 327–361.

[113] R Yi Young and Jeffrey R Koseff. “Revised mixing coefficient scaling for sheared stably stratified turbulence”. In: *Journal of Fluid Mechanics* 952 (2022), A18.

[114] Hongbin Yu, Mian Chin, Tianle Yuan, Huisheng Bian, Lorraine A Remer, Joseph M Prospero, Ali Omar, David Winker, Yuekui Yang, Yan Zhang, et al. “The fertilizing role of African dust in the Amazon rainforest: A first multiyear assessment based on data

from Cloud-Aerosol Lidar and Infrared Pathfinder Satellite Observations". In: *Geophysical Research Letters* 42.6 (2015), pp. 1984–1991.